This document was prepared for the ETI by third parties under contract to the ETI. The ETI is making these documents and data available to the public to inform the debate on low carbon energy innovation and deployment.

Programme Area: Marine

Project: PerAWAT

Title: Report on Comparisons of Nonlinear Models with Experimental Data for both Single Devices and Arrays of Devices

Abstract:

This deliverable details the simulation results and experimental data for the wave calibration tests and device performance tests involving focused wave groups, a subset of the large array testing programme conducted as outlined in WG2 WP2 D1.

Context:

The Performance Assessment of Wave and Tidal Array Systems (PerAWaT) project, launched in October 2009 with £8m of ETI investment. The project delivered validated, commercial software tools capable of significantly reducing the levels of uncertainty associated with predicting the energy yield of major wave and tidal stream energy arrays. It also produced information that will help reduce commercial risk of future large scale wave and tidal array developments.

Energy Technologies Institute

PerAWaT

WG1 WP1 D13: Report on comparisons of nonlinear models with experimental data for both single devices and arrays of devices

Author: C. Fitzgerald

Checked by: P. H. Taylor and R. Eatock Taylor

Date: 3rd July 2013

Version 1.1

Executive summary

In this deliverable (WG1 WP1 D13), the simulation results and experimental data for the wave calibration tests and device performance tests involving focussed wave groups are presented. The focussed wave group tests area subset of the large array testing programme conducted by QUB as outlined in WG2 WP2 D1. The experimental data was provided as part of deliverable WG2 WP2 D5. The numerical reconstruction of the fully nonlinear incident focussed waves from measured wave probe data is demonstrated as part of the simulation of the wave calibration tests. The nonlinear PTO force implemented in the experimental tests is modelled using a similar approach to that described in previous deliverables such as WG1 WP1 D10 and WG1 WP1 D11/D12. These preceding deliverables were concerned with the operation of devices with linear and nonlinear PTO mechanisms in regular and irregular waves, respectively. Therefore, this deliverable draws together parts of the experimental programme and the fully nonlinear aspects of the numerical modelling work stream.

The objective of the deliverable was to simulate the experimental device performance tests using the fully nonlinear model and to compare the results. This report provides an account of how the different aspects of performance tests were modelled, including a description of the PTO force model and an analysis and numerical reconstruction of the experimental wave generation procedure. The device displacement, PTO force and the power absorbed time-histories of the fully nonlinear simulations of the performance tests are compared to the experimentally measured behaviour for both the operation of isolated devices and four devices within a square array. Analysis of repeatability tests indicated that in some cases a large degree of uncertainty existed in the results and so the mean time-histories over the set of repeatability tests were used for comparison. A measure of the agreement between the numerical and experimental results is also included.

Table of contents

1 Introduction

1.1 Scope of this document

The focussed-wave isolated device and square array performance tests conducted as part of the QUB test programme reported in WG2 WP2 D5 are simulated here using the fully nonlinear potential flow solver OXPOT described in WG1 WP1 D7. This report contains the comparisons of the numerical simulation results and experimental measurements for the device displacement, the PTO brake force and, by derivation from the two preceding quantities, the power absorption. An assessment of the success of the OXPOT simulations in predicting the measured behaviour is provided by a comparison of the r.m.s. displacement and mean power absorbed for the simulations to those in the experimental tests.

This report comprises four main sections. A summary of the approach taken in the experimental tests conducted at Portaferry is provided in section 2 with a particular emphasis on the focussed wave group tests. The OXPOT simulations of the wave calibration tests for the focussed waves and the numerical focussed wave generation are described in section 3. In section 4, the isolated device performance test simulation results are presented and compared to the experimental results. A discussion of the hemispherical mesh, the PTO force model and the influence of domain width is also provided in this section. Some array performance test simulation results are presented and compared to the experimental data in section 5.

The focussed wave group wave calibration and device performance tests which formed part of the complete QUB test programme take precedence in this report and are described in section 2. A list of the different focussed wave groups used in testing is provided consisting of four phases for each permutation of the three different energy periods and two different focus wave amplitudes proposed prior to the test programme. The four phase realisations of the focussed waves, each shifted by 90°, are used to separate the crest-focussed wave group into its constituent harmonics. Furthermore, the same harmonic separation approach is used to linearise the measured free-surface elevation and hence to reconstruct the wavemaker signal in section 3. A discussion of the repeatability of the performance tests is also included in this section 2. The experimental results upon which this discussion is based highlight the likely difficulties that occur in trying to simulate the experimental behaviour.

The simulations of the wave calibration tests and performance tests for the isolated device are discussed and compared to the corresponding experimental data in sections 3 and 4, respectively. In section 4, an investigation into two possible discretisation methods for the rounded-end cylinder geometry is described. The numerical model of the PTO brake force is also discussed in some detail with comparisons to an experimental brake-force time-history. Prior to the presentation of the simulation results, an investigation into the influence of the numerical wave tank width on the device response is described. The convergence of the simulation results is also considered before the computational mesh specifications for each of the three different focussed-wave energy periods are provided. An analysis of the harmonic separation method as applied to the device displacement (experimental or numerical) results indicates that only reasonable but not perfect harmonic separation can be achieved. Therefore, only one phase realisation of the focussed-wave group performance tests is simulated for a given energy period. No harmonic separation is applied and the fully nonlinear OXPOT time-histories are compared to the experimental data. This section concludes

with comparisons of the fully nonlinear device displacement, PTO brake force and power absorption time-histories obtained from the OXPOT simulations to the experimental measurements. A brief discussion of the influence of nonlinearity in the OXPOT simulations is also provided at the end of this section.

The array performance tests are described in section 5. Most of the computational mesh specifications are extrapolated from the single device simulation, the PTO force model is as outlined in the isolated device section and so the section primarily consists of the comparison of the experimental and numerical performance results. The difference in the amplitudes of the experimental device motions for the left and right devices at the front and rear of the array is highlighted. In order to assess the array interactions it is necessary to use the isolated and square array OXPOT device displacement results – the numerical simulation of the performance tests assumes the interactions are symmetric about the centre line (aligned in the direction of wave incidence) of the wave tank

1.2 Acceptance criteria

The acceptance criteria for WG1 WP1 D13 are:

"Report summarises the approach taken in both modelling and experimental testing. Full comparison of the results presented, including a measure of the accuracy of the fully nonlinear analysis in predicting the measured behaviour."

Section 2 summarises the approach taken in the experimental testing and sections 3 and 4 contain descriptions of the important aspects of the numerical model. The comparisons of the device displacement, PTO force and power absorption time-histories are presented in section 4 and 5 for the isolated device and square array of four devices. Both of these sections contain measures of the accuracy of the fully nonlinear simulations in predicting the experimentally measured behaviour. These are the r.m.s. device displacement and the mean power absorbed.

1.3 Context of the deliverable

This deliverable draws on the experimental data provided by QUB as part of WG2 WP2 D5 and utilises the lessons learned from the fully nonlinear simulations of single devices and arrays of devices described in deliverables WG1 WP1 D10 to produce comparisons of numerical and experimental device performance results.

The forthcoming deliverable WG1 WP1 D14 is likely to include linear simulations of some the performance tests considered here in order to compare the accuracy of the linear and nonlinear simulations in modelling the experimental behaviour. Simulations of focussed wave groups with larger focus amplitudes than featured in the experimental tests may also be considered in order to draw conclusions regarding the importance of nonlinearity in the interactions.

2 Summary of scale model WEC/focussed wave group tests at Portaferry wave basin

The test programme outlined in WG2 WP2 D1 for small and large arrays of scale model wave energy devices (including isolated device tests) was completed in July 2012 by QUB as reported in deliverable WG2 WP2 D5. The programme, comprising wave calibration, device characterisation and device performance tests, was conducted at the QUB wave basin at Portaferry. This wave basin, which measures approximately $18m \times 16m$, was sufficiently large to allow tests for device arrays of up to 24 devices within a working area of $2m \times 6m$. However, for this deliverable we consider the performance of isolated devices and small arrays of four devices only due to computationally intensive nature of the OXPOT simulations. Simulations of arrays of more than four devices would require prohibitively long computational times. During the test programme the performance of the scale model device in isolation and in small arrays of four devices was assessed in regular waves, irregular waves and focussed wave groups. A wave calibration test and device performance test was conducted for each sea state or focussed wave and for the focussed waves the performance tests were in some cases repeated in order to assess experimental variability.

This deliverable contains a report on the fully nonlinear simulations of focussed wave group tests for isolated devices and small arrays of four devices. Of particular interest is the importance of nonlinearity in the experimental tests, and the capability of the fully nonlinear potential flow solver (OXPOT) for modelling the nonlinearity is also analysed. The focussed wave group tests were included in the experimental programme because nonlinearity can be controlled and confined to a single localised interaction in such interactions and because the interactions are suitable for simulation by OXPOT. In contrast to regular waves, focussed wave group interactions involve a broad range of frequencies and yield only one large wave event thus reducing possible wave energy dissipation due to localised breaking. For irregular waves, the duration of the tests (typically about 200 wave periods) and the size of the free-surface and number of devices requiring discretisation meant that simulating irregular wave tests and/or large arrays was impossible due to potentially prohibitively large simulation times. To summarise, focussed wave groups are preferable over regular waves and realisations of irregular sea states for investigations into hydrodynamic nonlinearity because:

- regular waves tests lack any representation of the broadbanded nature of the spectrum of real ocean waves;
- irregular wave tests yield large wave events sporadically and are affected by wave reflections due to the finite size of wave tanks;
- focussed waves tests involve many wave components of different frequencies, can be carefully controlled to yield a large wave event at a specific location and time, and have a relatively short duration precluding interference from side wall reflections.

Therefore, focussed wave tests are suitable for both numerical and physical wave tank tests.

The Portaferry wave basin is 17 metres long, 15 metres wide and includes a 12 metre wide span of wave paddles bounded by curved walls. (A more complete set of specifications is given in section 3 of WG2 WP2 D4). The basin contains a four metre long section of constant depth $0.625m$ in front of

the paddles followed by a slope to a beach at the far end of the basin from the paddles. A sloped beach of stones is present at the two side walls of the wave basin. The focus location for the wave groups was specified to be positioned four metres from the wave paddles at the end of the constant depth section of the tank. The focussed waves are all unidirectional and so the wave profile was expected to be approximately homogenous perpendicular to the direction of wave propagation. In particular, it was expected that the focussed wave should be homogeneous in the region where the devices were to be located for the isolated device and small array tests.

The scale model device geometry is that of a rounded vertical cylinder, i.e. a vertical cylinder with a hemispherical end. This geometry was preferred to a truncated vertical cylinder because vortex shedding and viscosity is likely to be significantly larger for the truncated case (see (Yeung & Jiang, 2011) for a discussion of the effects of shaping on viscous damping) which will adversely affect comparisons between potential flow codes such as WAMIT and OXPOT with experimental results. Furthermore, such viscous effects also adversely affect WEC performance so that designs are more likely to have rounded ends rather than truncated sections. As described in WG2 WP2 D4, the wetted surface of the WEC model in still water is a $250mm$ diameter cylinder with a hemispherical end and a total draft of $250mm$. (The correct draft for each model was achieved by the addition of ballast.) Above the water line the model geometry is a cylinder of constant diameter $250mm$. The proposed Froude length scale factor is 1:80 so that the device represents a full scale device of $20m$ diameter in water of depth $50m$. In the square array configuration, the devices forming the sides of the square are positioned a (centre-to-centre) distance of $750mm$ apart. The unidirectional focussed wave groups are normally incident on one side of the square array.

The motion of the wave energy device model is constrained to heave by an air bearing and the maximum amplitude of motion is determined by the air-bearing shaft supports. The amplitude of motion is further restricted so that the waterline never retreats below nor rises above the vertical cylinder section of the model. A wire and pulley is used to convert the heave motion of the model to rotational motion. A solenoid-actuated rotary brake provides a controllable brake force which acts as the power take-off (PTO) mechanism. Although the characteristics of the brake are relatively stable the RMS brake torque is controlled using feedback from the measured brake force to ensure an approximately constant Coulomb-friction-type force is applied. A schematic of the scale model device is shown in Figure 1.

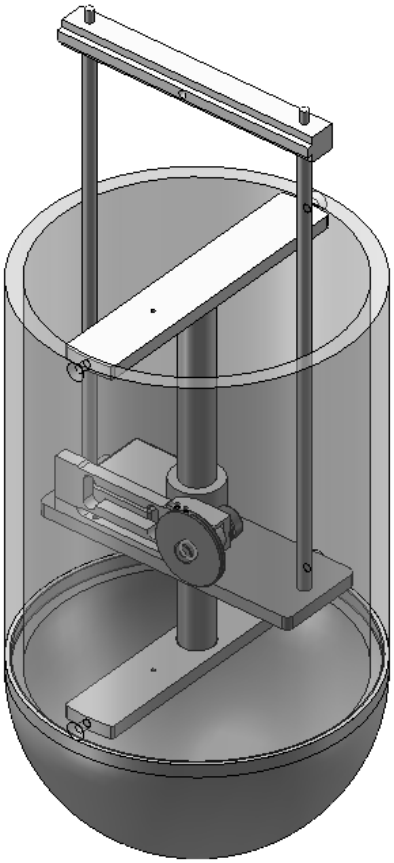

Figure 1: Schematic of the scale model wave energy device (obtained from the WG2 WP2 D2 'Tender for fabrication' appendix.)

2.1 Focussed wave group tests

The focussed wave group experimental programme comprised two separate sets of experiments – wave calibration tests and device performance tests. In the wave calibration tests, the device was not present in the wave tank and a basic set of four probes augmented by a probe where the device (or devices) would be were used to measure the free-surface elevation at various points in the wave tank. Given the level of control and accuracy available to the wavemaker it was considered sufficient to obtain one set of calibration results per focussed wave. For the device performance tests, where significant variability in the results was expected due to the uncertainty in the reliability of the parts involved the motion of the physical model such as the air bearing and the brake, it was considered necessary to repeat the tests a number of times.

2.1.1 Wave calibration tests

For the focussed wave calibration tests, a basic set of four wave probes were positioned four metres either side of the centre line of the tank, a distance of two metres and four metres from the wave paddles, respectively. In the case of the isolated device calibration tests, this basic set of four probes was augmented by a single wave probe at the proposed location of the device $(x, y) = (4.0m, 0.0m)$ where x measures perpendicular distance from the wave paddle and y is measured in the lateral direction from the centre of the tank. Similarly, the wave calibration tests for the small

array of four devices specified to form a square configuration with centre-to-centre distances along the sides of the square of $0.75m$ (three device diameters) feature four auxiliary wave probes located at $(x, y) = \{(4.0m,\ 0.0m),\ (4.0m, 0.75m),\ (3.25m, 0.0m),\ (3.25m, 0.75m)\}$. This wave probe data can be processed and used as input for the wavemaker motion in OXPOT in order to simulate the focussed wave generation. Thereafter, the OXPOT simulation results at the wave probe locations can be compared to the experimental measurements.

In the next section, the method for generating the focussed waves in OXPOT is described. First, we consider the full set of focussed waves generated and how phase control can be used to extract the hydrodynamic nonlinearity present in the wave propagation and device interactions. The focussed wave groups are denoted by the full-scale energy period T_e and linear wave amplitude at the focus location A as listed in Table 1. Therefore, given the scale factor of 1:80, a wave with energy period $T_e = 11.0s$ and focus amplitude $A = 3m$ corresponds to an experimental wave of approximate energy period $1.23s$ and amplitude $0.0375m$. Although the full scale characteristics of the wave groups will be referenced when discussing the experimental interactions it is implicit that the actual period and amplitudes observed are the scaled values. For each period, there are at least two associated amplitudes and for each amplitude a set of four phase shifted focussed waves. Each focussed wave is generated with four different phases corresponding to a phase shift of $\varphi = 0°, 90°, 180°, 270°$ relative to the basic focussed wave. Careful control of the focussed wave phases permits the use of the phase inversion method and a generalisation of this method to extract the higher order harmonics from the time-histories of kinematic (free-surface elevation) and dynamic (displacement) quantities. This approach, utilised here, is summarised next.

Test number range	Energy period $T_e\ [s]$	Amplitude $A\ [m]$
$1-4$	7.0	1.0
$5-8$	7.0	3.0
$9-12$	9.0	1.0
$13-16$	9.0	3.0
$17-20$	11.0	1.0
$21-24$	11.0	3.0
$25-28$	11.0	4.0

Table 1: Focussed wave group test cases.

A set of wave probe measurements at the focus probe for four focussed waves generated in the wave calibration tests for the isolated performance tests is shown in Figure 2. The wave with largest crest is sometimes referred to as a 'crest-focussed wave' and the wave possessing the largest trough is referred to as a trough-focussed wave. Crest and trough focussed waves are used in phase inversion methods to separate the odd and even harmonics. To demonstrate the phase inversion and the four-phase harmonic extraction method, it is useful to first consider a focussed wave in the context of the linearised water wave theory. In a unidirectional irregular sea state, if the ocean surface is considered to be a linear Gaussian process then the free-surface elevation ζ is modelled as a set of N independent small waves of random amplitude, i.e.

$$\zeta(x,t) = \sum_{m=1}^{N} a_m \cos(k_m x - \omega_m t + \varepsilon_m) \quad (1)$$

where $(a_m, \omega_m, k_m, \varepsilon_m)$ are the amplitude, frequency, wavenumber and phase of a the m^{th} wave component. By controlling the phases of the incident wave components so they satisfy $\varepsilon_m = -k_m x_0 - \omega_m t_0$ it is possible to generate a large wave crest (crest focussed wave) at the prescribed focus location (x_0, t_0). A more general focussed wave form is obtained from phases of the form $\varepsilon_m = -k_m x_0 - \omega_m t_0 + \varphi$. In this case, the crest focussed wave corresponds to $\varphi = 0$ and the trough-focussed wave corresponds to the phase shift $\varphi = 180°$ (a trough occurs at the focus because the sign of each wave component is inverted).

In a fully nonlinear environment, the linear description of a focussed wave group is insufficient to describe focussed waves with large amplitudes relative to the peak wavelength – in this case the second order contributions (and higher) must be included in the description. A narrow banded approximation is adopted to represent the focussed wave group around the focus event as a wave packet of monochromatic 'carrier wave' oscillations at the peak spectral frequency modulated by a slowly varying amplitude function $a(t)$. Using this narrow-banded approximation, which has been applied successfully to other focussed wave group analyses (Zang, et al., 2010), it is argued that regular wave Stokes' expansions can be extended to represent focussed wave groups and so the kinematic and dynamic (when a structure is present) quantities can be expressed as

$$\begin{aligned} q_\varphi = {} & a q_{11} \cos(\theta + \varphi) + a^2 (q_{20} + q_{22} \cos 2(\theta + \varphi)) \\ & + a^3 (q_{31} \cos(\theta + \varphi) + q_{33} \cos 3(\theta + \varphi)) \\ & + a^4 (q_{42} \cos 2(\theta + \varphi) + q_{44} \cos 4(\theta + \varphi)) + O(a^5) \end{aligned} \quad (2)$$

where $a = a(t)$ is the wave group envelope, φ is the phase of the peak wave component and q_{ij} is a transfer function representing sum ($i = j$) and difference ($j = i - 2$) harmonics. The crest and trough focussed wave groups generated by careful control of the phases of the wave components can be used to extract higher order nonlinear information from the fully nonlinear time-histories for kinematic/dynamic wave quantities in the manner described by (Baldock, et al., 1996) and (Borthwick, et al., 2006) for the free-surface elevation and (Zang, et al., 2010) for diffraction loads. In particular, the odd and even harmonics can be separated by combining the time-histories for the crest (q_0) and trough (q_{180}) focussed waves as follows

$$\frac{q_0 - q_{180}}{2} = a q_{11} \cos\theta + a^3 (q_{31} \cos\theta + q_{33} \cos 3\theta) + O(a^5), \quad (3)$$

$$\begin{aligned} \frac{q_0 + q_{180}}{2} = {} & a^2 (q_{20} + q_{22} \cos 2\theta) + a^4 (q_{42} \cos 2\theta + q_{44} \cos 4\theta) \\ & + O(a^6). \end{aligned} \quad (4)$$

This harmonic separation method is often referred to as the phase inversion method as it involves combining two focussed wave time-histories generated using linear wavemaker signals with inverted signs. The individual harmonics can be obtained from the odd and even time-histories by digitally filtering the spectral content of these signals so that only the peak associated with the harmonic of interest remains. It should be noted that the difference terms at a given harmonic $\cos n\theta$ are generally much smaller than the associated sum harmonic assuming the amplitude a is very small so that $O(a^{n+2}) \ll O(a^n)$. For example, the third order difference term $a^3 q_{31}$ has a

much smaller amplitude than the linear sum harmonic aq_{11} for the first order harmonic $cos\theta$ and so the contribution from the third order difference term can be neglected locally.

It is also possible to generalise the phase inversion method to extract the first, second, third without digital filtering and only a simple filter to obtain the fourth order sum harmonic and the second order difference harmonics. This method requires four time-histories from focussed wave interactions with wave components $90°$ out of phase such as that shown in Figure 2. This four-phase harmonic extraction method is described in (Fitzgerald, et al., 2012) and involves four linear combinations of the time-histories $(q_0,\ q_{90},\ q_{180}, q_{270})$ and the Hilbert transforms[1] of the $\varphi = 90°$ and $\varphi = 270°$ signals (q_{90}^H, q_{270}^H) to give the following:

$$(q_0 - q_{90}^H - q_{180} + q_{270}^H)/4 = aq_{11}\cos\theta + a^3 q_{31}\cos\theta + O(a^5), \quad (5)$$
$$(q_0 - q_{90} + q_{180} - q_{270})/4 = a^2 q_{22}\cos 2\theta + a^4 q_{42}\cos 2\theta + O(a^6), \quad (6)$$
$$(q_0 + q_{90}^H - q_{180} - q_{270}^H)/4 = a^3 q_{33}\cos 3\theta + O(a^5), \quad (7)$$
$$(q_0 + q_{90} + q_{180} + q_{270})/4 = a^2 q_{20} + a^4 q_{44}\cos 4\theta + O(a^6), \quad (8)$$

with the dominant harmonic highlighted in red. In both physical model wave test data and the numerical simulation results the higher order harmonics contributions to the fully nonlinear wave elevation and device response are extracted using the time-histories of the focussed wave groups with the prescribed $90°$ phase differences. The harmonic signals (5)-(8) extracted from both the numerical simulation results and from test measurements can be compared in order to assess the effectiveness of OXPOT in modelling the experimental wave generation method.

[1] http://mathworld.wolfram.com/HilbertTransform.html

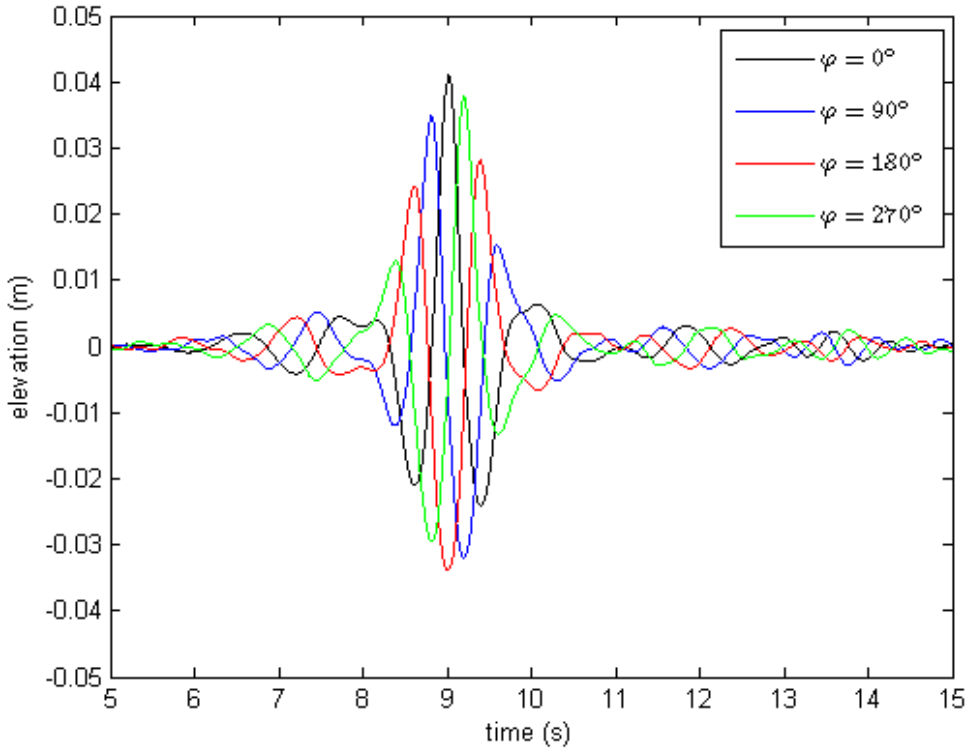

Figure 2: Free-surface elevation at the focus location for four different realisations of the focussed wave group corresponding to $(T_e, A) = (9.0s, 3m)$ each 90 degrees out of phase.

2.1.2 Device performance tests – repeatability

Each single device performance test involving a given phase realisation of a particular focussed wave was repeated ten times in order to assess the repeatability of the experiments and to measure the variability in the results obtained. A brief analysis of the results for the single device focussed wave interactions of most interest are provided here. In section 4, the results of OXPOT simulations of the performance tests involving crest-focussed interactions of full-scale period T_e equal to 7.0s, 9.0s and 11.0s of full-scale amplitude $A = 3m$ are compared. Therefore, the repeatability of each of these tests is considered next.

To illustrate the level of variation in the results, the maximum, minimum and mean device responses (from the set of ten repeated tests) are plotted for the performance tests 5, 13 and 21 corresponding to the crest-focussed incident waves of full-scale focus amplitude $A = 3.0$ and full-scale period $7.0s$, $9.0s$ and $11.0s$, respectively, in Figure 3. It is clear that there are significant variations in the amplitude of the device response for the $T_e = 5.0s$ performance test indicating that the reliability of the various moving mechanical parts in the model is compromised and that significant frictional losses (in addition to those occurring due to the WEC brake) are occurring during the interaction. In contrast, the variation in the device displacement for the wave of longest peak period (full-scale energy period $T_e = 11.0s$) is much smaller than for the wave of shortest peak period. The maximum and minimum responses differ from the mean value quite considerably for the incident waves of energy period $T_e = 9.0s$ although the difference is not as significant as the $T_e = 7.0s$ case. The mean device displacement will be used for the purposes of comparison when the OXPOT simulations of the performance tests (isolated devices and arrays) are presented.

Although the PTO force has not been considered here it displays similar statistical properties over the ensemble of ten tests and so the mean PTO value is also used in the comparisons between experimental measurements and numerical simulations.

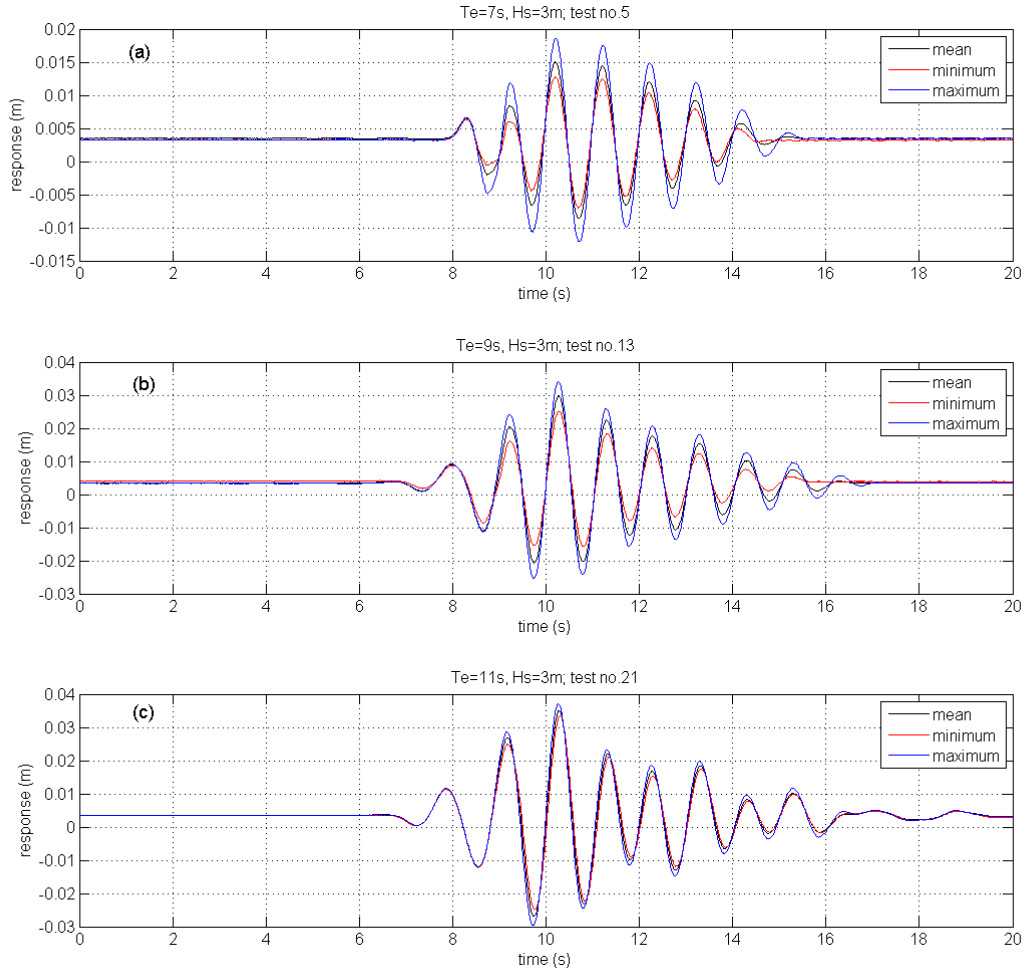

Figure 3: Mean (black), maximum (blue) and minimum (red) device displacement from the set of ten repeatability tests for device performance test (a) number 5 ($T_e = 7.0s,\ A = 3m, \varphi = 0°$), (b) test number 13 ($T_e = 9.0s, A = 3m, \varphi = 0°$) and (c) number 21 ($T_e = 11.0s, A = 3m, \varphi = 0°$).

3 OXPOT simulation of experimentally generated waves

3.1 Fully nonlinear potential flow simulations – a brief summary

The fully nonlinear potential flow solver (OXPOT), the methodology for which was described by (Bai & Eatock Taylor, 2006), (Bai & Eatock Taylor, 2007) and (Bai & Eatock Taylor, 2009) and summarised in WG1 WP1 D7, was used to simulate the experimental wave calibration and device performance tests. In this time-domain solver, a higher-order boundary element method is used to solve the mixed boundary value problem in the Eulerian frame of reference and the free-surface and body boundary conditions are time stepped in the Lagrangian frame using a fourth order Runge-Kutta (RK4) method. The hydrodynamic force is computed using the auxiliary function described by (Wu & Eatock Taylor, 1996) and the RK4 time-stepping scheme is used to solve the equation of motion of

the body and the velocity obtained is used in the body boundary conditions. In this manner, the coupling of the fluid-structure motions is solved.

The computational boundary is discretised by quadratic isoparametric elements: the walls and vertical body surfaces are meshed with quadrilateral elements and the free-surface is meshed using a set of unstructured triangular elements generated from the Delaunay triangulation method. The hemispherical cap of the device can be discretised using two alternative approaches. In the first, a Delaunay triangulation of the truncated surface of the vertical cylinder is generated after which the z-coordinates are projected onto the hemisphere. The second approach involves constructing a structured mesh consisting of strips of contiguous conical rings which taper to a single point at the bottom of the hemisphere. Simulations involving both meshes will be compared later in the report in order to ensure consistency in the OXPOT results irrespective of the exact mesh details. The domain decomposition technique described by (Bai & Eatock Taylor, 2007) is used to increase computational efficiency and is evident from the interface walls beneath the free-surface. Furthermore, the lateral symmetry of the interaction problem for unidirectional incident waves is exploited to allow us to simulate only one half of the domain. In the simulations the waves are generated by piston motions of one end wall and a damping layer is implemented at the opposite end of the tank to absorb the transmitted waves. The side walls have no-flow conditions and reflect outgoing waves; however, the reflected waves should not affect the response of the device during and immediately after the largest crest/trough of the focussed wave interacts with the structure. Once the focussed wave has passed, reflections may have an impact on the body motion. Their effect may be reduced by using a wider tank requiring correspondingly increased computational effort. Therefore, it may be necessary to simulate the device motion in numerical wave tanks of different width in order to assess the importance of the reflections.

3.2 Reconstruction of experimental paddle wavemaker signal

Prior to the device performance tests, wave calibration tests were conducted in the absence of any device models to ensure the desired focussed waves were being generated by the paddle motions. The wavemaker, consisting of Edinburgh Design paddles, was provided with a linear signal in order to generate the waves. The OXPOT wavemaker, modelled as piston motions of the end wall, provides a reasonable approximation of the paddle wavemaker in the tank despite the lack of force-feedback control. Furthermore, a straightforward Biesel transfer function can be used to convert the wave probe measurements to piston-type motions of the OXPOT wavemaker. However, in the absence of the experimental wavemaker signals it was necessary to adopt a different approach to accurately simulate the experimental focussed waves.

In this approach the linear paddle signal is reconstructed from the calibration test wave probe data as follows:

1. The wave probe measurements of free surface elevation from the two wave probes a distance 2 metres from the wavemaker are averaged for each of the four phase values for a given focussed wave.
2. The approximate linear component (5) of the free-surface elevation is extracted from the four sets of data using a linear combination of the four phase-shifted focussed wave time-histories (and two Hilbert transforms of $\varphi = 0^\circ$ and $\varphi = 270^\circ$).
3. A discrete Fourier transform of the linearised free-surface elevation is then obtained.

4. Finally, a linear transfer function (involving the Biesel transfer function $T(k_n)$) is applied to each frequency component ω_n of the Fourier transform of the linearised signal to yield the amplitude spectrum of the paddle signal; the wavemaker signal is simply the inverse Fourier transform of this complex amplitude spectrum.

The piston wavemaker signal in OXPOT takes the form

$$x_p(t) = \sum_{n=1}^{N} -a_n^{\mathrm{p}} \sin(-k_n L - \omega_n t) + b_n^p \cos(-k_n L - \omega_n t) \quad (9)$$

where $x = -L$ is the position of the wavemaker at zero displacement. To obtain the real and imaginary parts (a_n^p, b_n^p) of the Fourier transform of the paddle signal it is necessary to apply the following transfer functions

$$a_n^p = 2(a_n \cos k_n x_0 - b_n \sin k_n x_0)/T(k_n) \quad (10)$$
$$b_n^p = 2(a_n \sin k_n x_0 + b_n \cos k_n x_0)/T(k_n) \quad (11)$$

to the real and imaginary parts (a_n, b_n) of the Fourier transform of the wave probe data at the probe location $x = x_0$.

To demonstrate the signal reconstruction method, the $T_e = 9s$, $H_e = 3m$ focussed wave is considered. The averaged wave probe data sets from wave probes 2 and 3, both a distance of 2 metres from the wavemaker and positioned at $y = 4.0m$ and $y = -4.0m$ relative to the centre line of the tank, for the four phase realisations of the basic focussed wave are shown in Figure 4. The data sets on which this plot is based have sample rates of 128Hz and last 24 seconds – only the first 16 seconds are shown here for clarity. At this distance from the wavemaker the wave components have not exactly coincided so the amplitude of the waves are smaller than the specified focussed wave value $A = 3/80 = 0.0375m$. The linear component of the $\varphi = 0°$ focussed wave realisation is obtained by a linear combination of the four signals (and Hilbert transforms of the $\varphi = 0°$ and $\varphi = 270°$ signals) and is shown in Figure 5 with the second order sum harmonic provided for comparison. As summarised in steps 3 and 4 above, the paddle signal reconstruction first requires the application of an FFT to the linearised wave probe data. Thereafter, the transfer functions (10) and (11) are applied to the FFT data and by taking the inverse FFT of the resultant data the paddle signal can be obtained. The paddle signal reconstructed from the wave probe data shown in Figure 4 is illustrated in Figure 6.

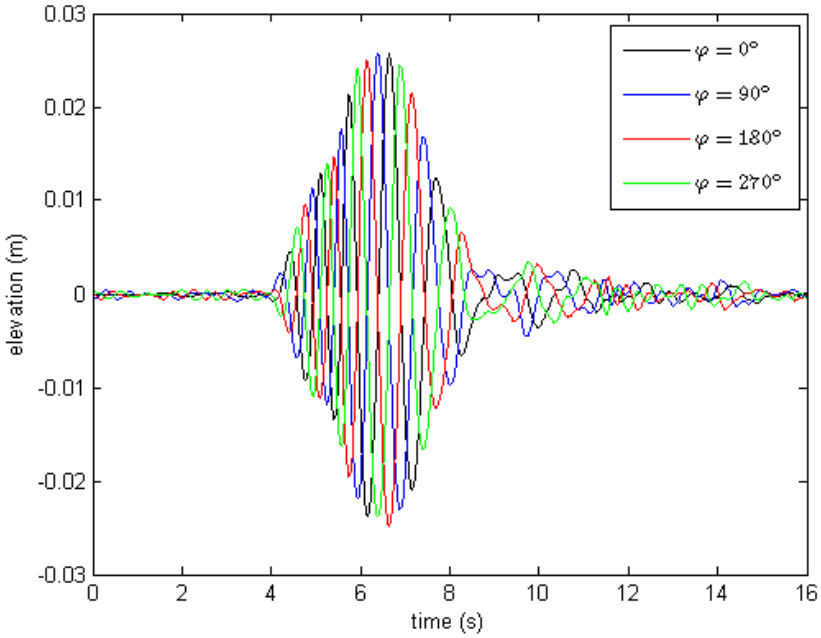

Figure 4: Time-history of averaged free-surface elevation at wave probes 2 and 3 for four focussed waves with phase differences of $90°$.

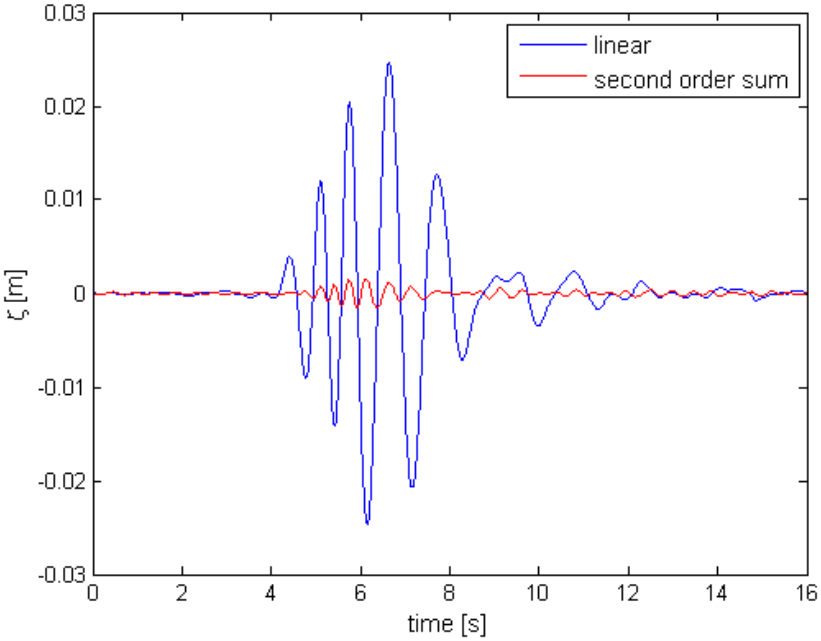

Figure 5: Linear component (blue) and second order sum harmonic (red) of crest focussed wave at wave probes a distance 2 metres from wavemaker.

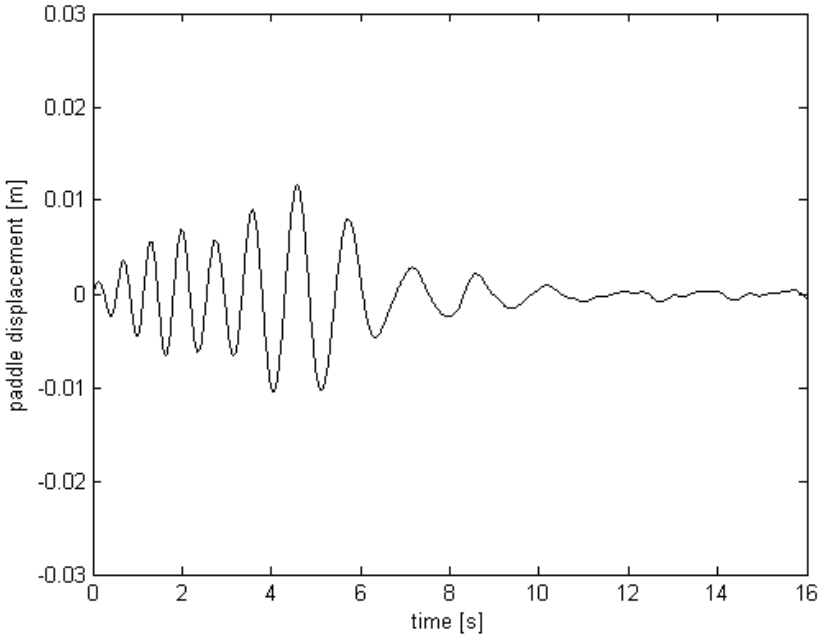

Figure 6: Paddle signal for OXPOT piston wavemaker to generate desired focussed wave.

3.3 Numerical simulations of wave calibration tests

The details of the OXPOT simulations of the focussed wave calibration test under consideration are specified next. Before describing the spatial and temporal discretisation of the simulation, it is useful to provide a context for the discretisation lengths by noting the parameters of the incident wave group at experimental scale. At full scale, the focussed wave group has an energy period $T\_e = 9.0s$ and amplitude $A = 3m$ corresponding to experimental values of $T_e \simeq 1.01s$ and $A = 0.0375m$. The wavelength corresponding to the energy period of the incident wave was determined to be $\lambda \simeq 1.56m$. The second order bound and free wave lengths will be approximately a half and a quarter of the linear wavelength. In order to model the second order contributions to the wave propagation it will be necessary for the free-surface elements to be smaller than the second order free wavelength – from observation, the elements should be at least five times smaller than the free wavelength of the harmonic that is to be included/modelled. The time-step should be at least one-fortieth of the peak period.

In the OXPOT simulations of the experimental tests, the density, gravitational acceleration and depth parameters were given values of 1000, 9.807 and 0.625, respectively, so that the domain and results required no scaling. With the focussed wave parameters in mind, the free surface in the wave propagation simulation was discretised so that the triangular elements had a side-length of $\Delta x = 0.032$, less than 1/12th of the second order free wavelength. The quadrilateral elements on the domain wall and contiguous to the free-surface were specified to have a height 0.04. The domain was specified to have a half-width of two elements, i.e. the numerical wave tank was a

narrow wave flume in order to minimise the computational time, and to have a length of 6.4. The damping zone was specified to be of length 1.5λ in order to absorb as much of the transmitted wave energy as possible. The fourth order Runge-Kutta time-stepping scheme was implemented with time steps of 0.01 (approximately $T_e/100$) and 16 seconds of the interaction were simulated. The wavemaker signal (9) was determined from the first 181 frequency components of the transformed wave probe spectrum – the maximum frequency was 7.5Hz.

Four wave propagation simulations, one for each realisation of the focussed wave, were run and the free-surface elevation at the focus location was recorded. Four sets of wave probe data for the free-surface elevation at the focus location in the wave tank were also available. Therefore, the four phase-combined time-histories (5)-(8) which separate the linear, second order sum, third order sum and fourth order sum and second order difference harmonic contributions were determined from both numerical simulations and wave tank tests and are compared in Figure 7. The agreement at first and second order sum is excellent indicating that the paddle signal obtained from the wave probe data is reasonably accurate and that the computational mesh is sufficiently fine for second order analyses. At third order, the agreement is not as good although around the focus the oscillations are in phase and of similar order of magnitude indicating that the mesh is capturing some, if not all, of the third order kinematics. The oscillation amplitude of the third order component is approximately forty times smaller than the linear component so the third-order free-surface elevation is likely to be sensitive to any discrepancies between the numerical and experimental wave generation processes. For the linear combination containing the fourth order contribution, it is clear that OXPOT is not capturing the fourth order sum harmonic at the focus time. However, the agreement of the long wave second-order difference component as computed by OXPOT with the wave tank test data is reasonably good.

A similar agreement between numerical and experimental results can be observed for the other simulations of the wave calibration tests, that is to say that the linear, second order sum and difference components of the free-surface elevation at the focus compare very well. The agreement at third order is not as good and the fourth order sum harmonic oscillations are not captured. However, given that the amplitude of the third order components is much smaller than the linear component it is considered unlikely that the third order component will have a significant effect on the device behaviour in the performance tests. Therefore, it is concluded that OXPOT simulates the wave calibration tests to second order for the free-surface meshes summarised in Table 2. Note that the so-called 'energy wavelength' is simply the wavelength corresponding to the energy period and that the energy period is provided at full scale (T_e) and experimental scale (T_e^E). The height of the wall element just below the free-surface is also provided for comparison. The number of elements per first-order wavelength is typically 40-50 corresponding to 11 per second order wavelength for free waves.

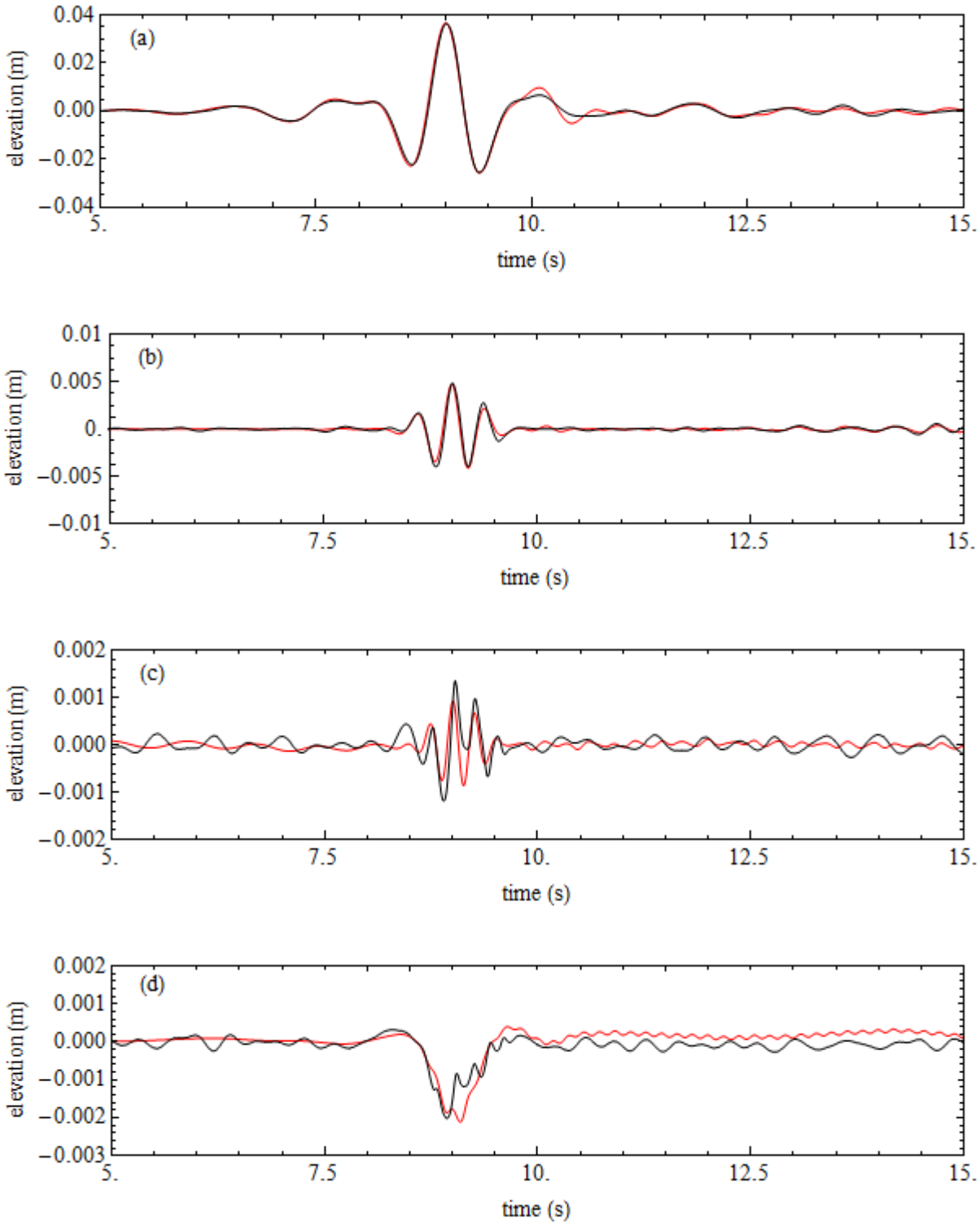

Figure 7: Comparison of (a) linear, (b) second order sum, (c) third order sum, (d) fourth order sum and second order difference harmonic contributions to the fully nonlinear free-surface elevation for the $(T = 9s, A = 3m)$ crest focussed wave at the focus as computed by OXPOT (red) and from focus wave probe data (black).

Energy Period (T_e, T_e^E)	Energy wavelength (λ_e)	Free surface element (Δx)	Wall element height (Δz)	Time-step (dt)	$\lambda/\Delta x$
$(7.0s, 0.78s)$	$0.955m$	0.0233	0.029	$0.01s$	69.6
$(9.0s, 1.01s)$	$1.56m$	0.032	0.04	$0.01s$	48.8
$(11.0s, 1.23s)$	$2.23m$	0.05	0.04	$0.02s$	44.5

Table 2: Summary of free-surface discretisation for wave calibration test simulations.

As an aside, it is useful to illustrate the harmonic separation achieved by the implementation of the four-phase linear combination formulae (5)-(8) for both the experimental wave probe measurements and numerical computational results. A semi-log plot of the amplitude spectrum of the linear combination is obtained in order to show the harmonic separation as shown in Figure 8; the spectra of the harmonics for wave probe measurements and for the OXPOT computations are shown in sub-figures (a) and (b) respectively. It can be seen that the OXPOT results recreate the experimental results effectively as far as third order where some significant discrepancies are evident. This is consistent with comparison of the OXPOT and experimental time-histories shown in Figure 7. At fourth order (around $f = 5Hz$) the spectral 'peak' for the OXPOT computations bears very little resemblance to the experimental spectral peak and, as seen in Figure 7 (d), the high frequency fourth harmonic oscillations are not reproduced. This is due to, among other things, insufficient mesh fineness for the free-surface discretisation. It is also worth remarking that the third and fourth order contributions to the total signal are much smaller than the first and second order contributions.

The time-step used in these wave propagation simulations was chosen to be small (approximately $T_e/100$) in order to ensure that the higher order harmonics resolved by the mesh would be advanced in time without losing any solution information. Using a small time-step for the wave propagation simulations involving narrow numerical wave tanks with a relatively small number of mesh nodes does not result in long computational times because the total domain does not contain a large number of nodes. In the next section, the computational domains contain a significantly larger number of element nodes and choosing a suitable time-step becomes important in this case. Therefore, the time step for the wave propagation simulations of the focussed wave group with full scale parameters ($T_e = 9.0s, H_s = 3.0m$) was increased by a factor of two and the difference in the second order sum harmonic signals was compared. (In the performance simulations, as will be discussed in this next section, the device motion to second order is sought.) The difference in the solutions is illustrated over the whole range of the simulation in Figure 9 and is less than 1% of the second order harmonic amplitude shown in Figure 7 (b). Therefore, a time-step of $0.02s$ or approximately 1/50th of the incident wave period should be sufficiently small to resolve any second order kinematics or dynamics. Extrapolating from this result, it is concluded that the incident wave of full/experimental scale energy period $T_e = 11.0s/1.23s$ can be simulated adequately to second order with the same time-step corresponding to 1/60th of a period and that a time-step of $0.01s$ will be more than sufficient for the simulations of the waves of period $T_e = 7.0s/0.78s$. These choices of time-step size are purposefully 'cautious' in order to ensure the convergence of the solution (assuming a suitable computational mesh). A much broader investigation into the convergence of the solutions with time-step size is necessary to determine the optimal time-step increment, i.e. a time-step increment that yields an accurate solution with a reasonably small computational time.

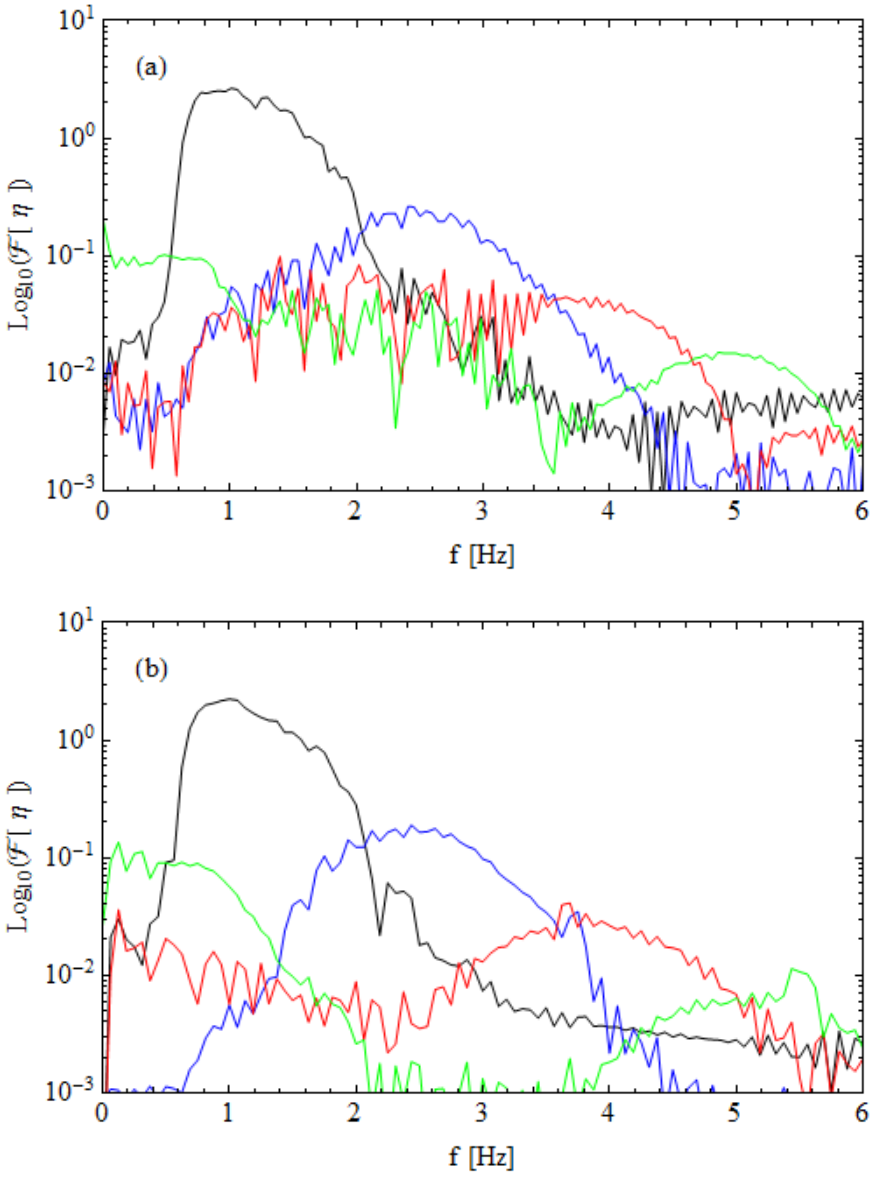

Figure 8: Semi-log plot of the Fourier transform of the linear combination (5) (black), (6) (blue), (7) (red) and (6) (green) for the experimental wave probe measurements at the focus (a) and for the OXPOT results at the focus (b).

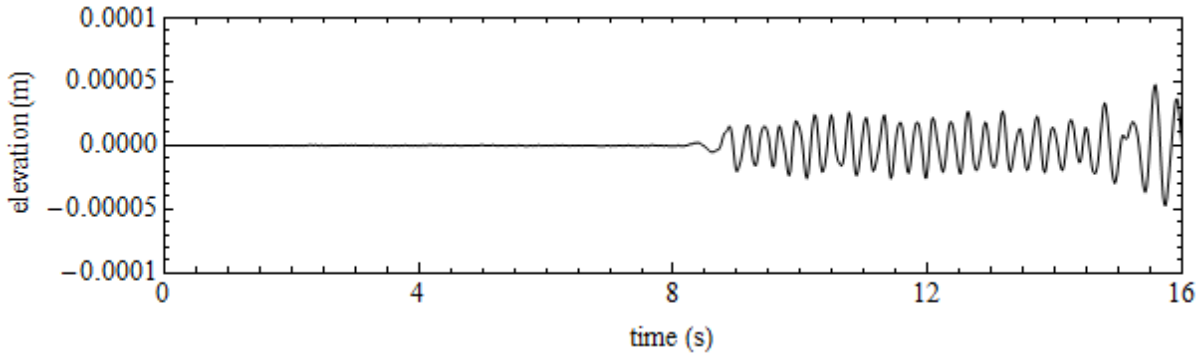

Figure 9: Difference in second-order harmonic of free-surface elevation for wave calibration simulation of test number 13 (focussed wave of full scale period $T = 9.0s$ and amplitude $A = 3m$) produced by changing the computational time-step from $dt = 0.01$ to $dt = 0.02$.

4 Isolated device simulations

4.1 OXPOT model of the experimental wave energy device

In order to simulate the performance of the 'physical model' or scaled model device in the experimental tests it is necessary to approximate the geometry within the computational domain and to approximate the device mechanisms with suitable numerical algorithms. The physical model of the wave energy device used in the test programme, as described in some detail in section 2, is a surface piercing vertical cylinder with a hemispherical cap which is restricted to move in heave only by a low-friction air bearing and whose energy is absorbed through a Coulomb friction brake.

Some of the properties of the device were specified with the numerical simulations in mind, e.g. the restriction of the device to motion in heave only via the implementation of a low-friction air bearing, and are straightforward to model. The geometry of the device, a rounded vertical cylinder, is chosen to minimise viscous drag and must be approximated with an appropriate mesh. In the next section a discussion of the different meshing options is presented. It has been noted in section 2 that a wire-and-pulley system is used to convert the heave motion of the device to a rotational motion. The PTO mechanism is a controllable rotary brake which acts on the pulley. Although there is not an exact relationship between the PTO force and the body motion (the brake torque is controlled using feedback from the measured brake force), the PTO force can be approximated and modelled as a constant Coulomb damping friction force. A brief discussion and analysis of the OXPOT model of the PTO force is presented in one of the following subsections.

It is useful to note that parasitic losses occurring at hinges or articulations in the model will affect the motion of the device but will be quite difficult to eliminate. Furthermore, although a rounded vertical cylinder was chosen as the device geometry viscous losses due to the heaving motion of the body will occur and will not be accounted for by the potential flow solver OXPOT. Therefore, although much of the physics of the device interaction can be described within the numerical model in a satisfactory manner, some aspects of the interaction will be quite difficult to simulate.

4.1.1 Different meshing approaches for the hemispherical end of the rounded cylinder

In OXPOT there are two possible methods for discretising the surface of the hemisphere on the bottom of the rounded vertical cylinder. In both cases, the adjoining vertical surface of the cylinder is discretised using a set of quadrilateral elements containing eight nodes which span the distance between the free-surface intersection and the beginning of the hemisphere. The number of quadrilateral elements around the circumference of the cylinder is an important parameter for determining the fineness of the mesh on the hemispherical surface because the basis set of nodes for the unstructured (Delaunay) or structured mesh of triangular elements is the set of nodes at the bottom of the vertical surface of the cylinder.

On the vertical surface, the number of elements which discretise the circumference and which discretise the vertical span of the cylinder are specified as simulation inputs. At each corner of a given quadrilateral element there will be a computational node upon which the boundary integral equation must be solved. However, the boundary element method is a higher order method and the position coordinates, the potential and its derivatives (the boundary data) vary quadratically within each element. Therefore, it is necessary to introduce a set of mid-point nodes on the sides of the quadrilateral element to complement the existing corner nodes which delineate each element. For quadrilateral elements this yields eight nodes per element and six for the triangular elements. As

described by (Bai & Eatock Taylor, 2006) and in section 2.3 of WG1 WP1 D7 the introduction of a set of shape functions in each element allow us to express the variation of the boundary data through the corresponding values of the nodes.

The corner nodes at the bottom edge of the set of the lowermost 'ring' of quadrilateral elements on the vertical cylinder surface form the basis set of nodes for the Delaunay triangulation of the adjoining hemispherical surface. The adapted Delaunay triangulation method involves generating an unstructured mesh on the planar truncated surface and projecting the nodes onto the desired hemispherical surface. The unstructured mesh of triangular elements is generated in the following manner (summarising the description given by (Bai & Eatock Taylor, 2006)). Firstly, a set of points on the circumference of the bounding circle which encloses the truncated cylinder surface are generated from the discretisation of the vertical cylinder surface. These points are the set of corner nodes (i.e. not mid-point nodes) of the quadrilateral elements which discretise the vertical cylinder surface. This set of bounding points forms an initial basis set of coarse triangles which are made finer by the insertion of more points within the planar domain. The number of extra points added is an OXPOT input and this controls the fineness of the triangulation. However, at the boundary of the truncated surface the triangle size depends on the fineness of the circumference discretisation. Mid-point nodes, necessary for the quadratic representation of the boundary data, are then generated based on the vertices of the Delaunay triangles. The z-coordinates are determined from the equation for the surface of the hemisphere $z = -d - \sqrt{a^2 - (x^2 + y^2)}$ where d is the draft of the cylinder in equilibrium and a is the radius of the cylinder and also the hemisphere. A schematic of the mesh for a (half) cylinder in a simulation (where symmetry is assumed) is shown in Figure 10. The OXPOT inputs for the mesh are the number of elements discretising the bounding circumference of the hemisphere and the number of points inserted to form the Delaunay triangulation.

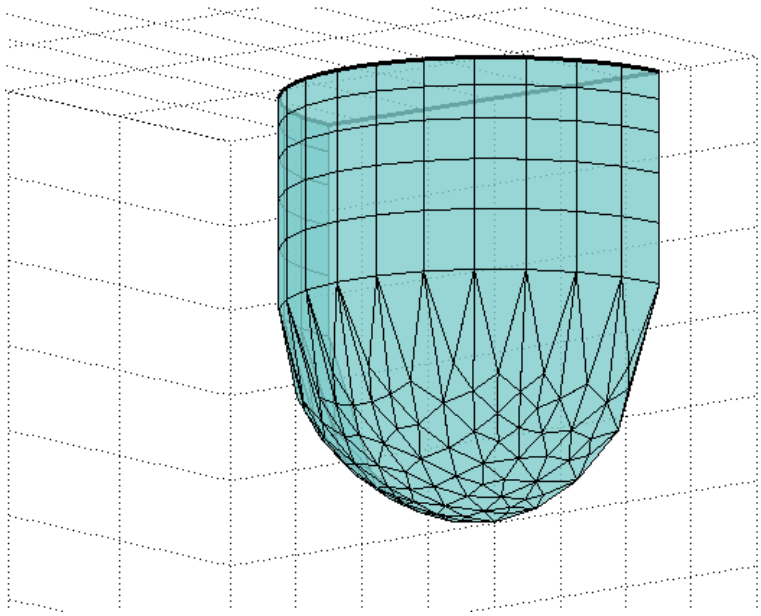

Figure 10: Graphic representation of the unstructured mesh on the hemispherical surface.

The alternative to the adapted Delaunay discretisation approach is to construct a set of basis nodes from rings on the hemisphere surface which decrease in radius away from the centre of the hemisphere finishing with a single node at the bottom of the hemisphere. The number of basis nodes on each ring is the same as the number of elements discretising the circumference of the cylinder and are then aligned along the same polar angles. In effect, the surface of the hemisphere is discretised by sets of longitudinal and latitudinal lines, the intersection of which give the corner nodes for the structured triangular elements. Mid-point nodes are inserted to complete the quadratic parameterisation of the boundary data, yielding a mesh like that illustrated in Figure 11. However, the mid-point nodes are prescribed to lie on the hemisphere surface and not half-way between the corner nodes, because the elements can have a curved geometry. The OXPOT inputs required to generate this mesh are the number of elements discretising the line formed by the intersection of the vertical cylindrical and hemispherical surface (which form the lines of 'longitude') and the number of 'rings' (which form the lines of 'latitude') which yield a set of basis nodes for the triangular elements.

In both cases, there will be a discretisation error associated with the surface mesh, i.e. the volume enclosed by the mesh will be slightly less than the actual volume of the physical model. However, the error is not as large as is represented in the diagrams because the elements can have a degree of curvature due to the higher order representation and are not in fact planar in geometry. Nevertheless, in the case of the mesh formed by the unstructured Delaunay triangulation the discretisation error is largest where the elements are elongated around the intersection with the vertical cylindrical surface. On the other hand, for the structured mesh of triangular elements the discretisation error is largest where the axis of cylindrical symmetry intersects the hemisphere – here a cusp is formed by the structured mesh. In order to ensure the meshes are reasonably accurate representations of the rounded end vertical cylinder, a simulation of the response of the device using both meshes is conducted and the results are compared.

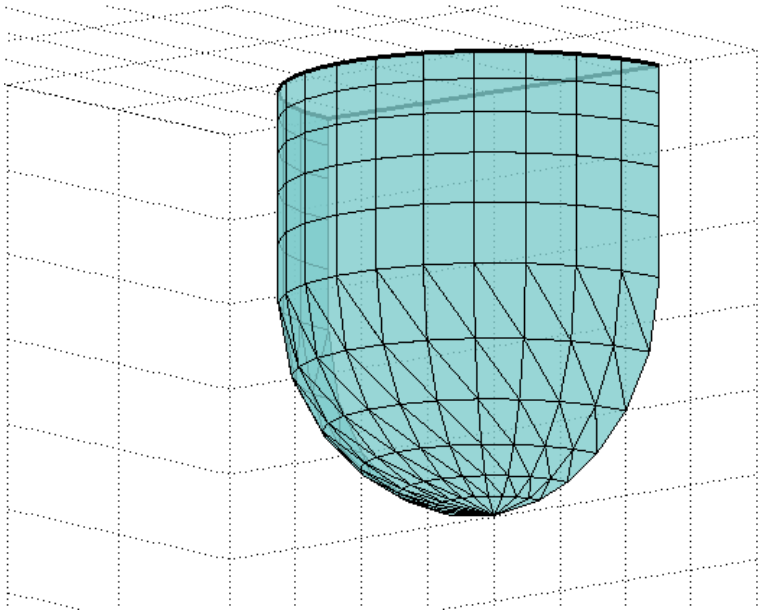

Figure 11: Graphical representation of the structured mesh used to discretise the hemispherical surface of the rounded cylinder.

The discretisation error associated with the meshing of the cylinder surface results in an underestimation of the volume of the cylinder which causes a mismatch between the water displacement and buoyancy force and the weight of the body. Therefore, in the numerical simulations the device equilibrium position is slightly lower than the actual physical value – the device 'sinks' when placed in the experimental equilibrium position in still water due to the net negative buoyancy force. This erroneous buoyancy force was observed to be non-negligible in some simulations. For example, in the focussed wave simulations involving the longest peak wavelength ($T_e = 11s$) the free-surface mesh was relatively coarse compared to the cylinder dimensions and, because the cylinder mesh and free-surface mesh must not have significantly different mesh element sizes, so the discretisation error for the cylinder was relatively large. To be specific, the volume discretisation error was sufficiently large that the resultant negative hydrostatic buoyancy force was of a similar order of magnitude to the Coulomb damping PTO force. For the focussed waves with shorter wavelengths, the mesh on the cylinder was correspondingly finer and the volume discretisation error was an order of magnitude less than the PTO force. As a consequence of this mis-match, the equation of motion of the body was adjusted so that a correcting upward force equal but opposite to the initial negative buoyancy force was applied on the body throughout the simulations. Therefore, at the start of each simulation there was a net force of zero on the cylinder(s) and no associated motion.

Without specifying the details of the computational mesh (all mesh 'patches' will be identical apart from on the hemispherical cap and it can be assumed that the mesh fineness there will be equivalent), a comparison of the results for the structured mesh and unstructured mesh is made in Figure 12. The fully nonlinear responses as compared in Figure 12(a) are virtually indistinguishable. The difference between the signals is shown in Figure 12(b) with the limits of the y-axis reduced by a factor of 10 compared to the displacement plot. From this difference plot it can be seen that the magnitude of the difference is significantly less than 1% and as desired the choice of mesh does not play a significant role in the device motion for the majority of the simulation. In the simulations that follow the structured mesh will be used because it allows more control over element size and minimises the occurrence of distorted elements.

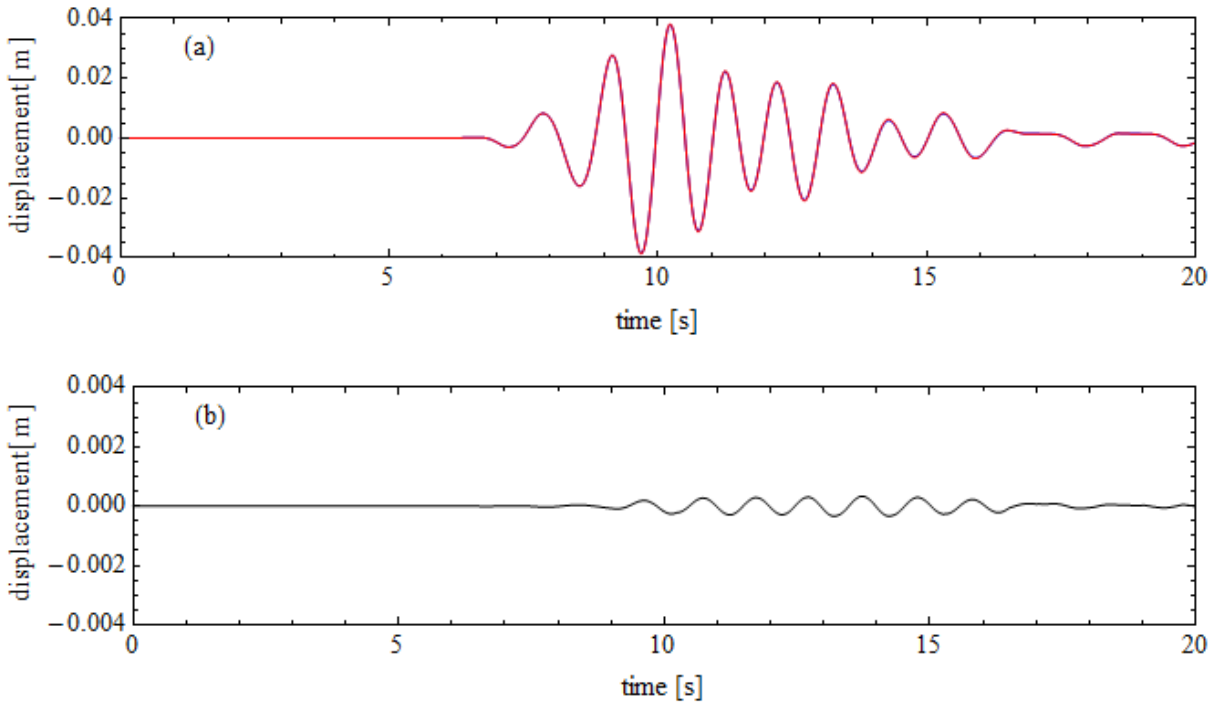

Figure 12: (a) Comparison and (b) difference between the fully nonlinear heave response of the device for the structured mesh of the hemispherical cap (blue) and the unstructured mesh (red).

4.1.2 PTO force model

From a modelling perspective, the most important facet of the WEC brake is that the brake force equals the input force until the input force exceeds the threshold target PTO force in which case the PTO force is approximately constant and opposes the motion. Such an arrangement is relatively straightforward to implement as an algorithm. However, the actual experimental brake force uses feedback mechanism in order to ensure the applied force is relatively stable and so it cannot be modelled exactly. Before describing the algorithm(s) used to model the PTO brake it is useful to analyse the PTO force time-history from an experimental test in relation to the body motion. In what follows, the PTO force will correspond to $F_{PTO}(t)$ in the equation of motion

$$M\ddot{\xi} = F_{HYDRO} + F_{PTO} - Mg, \tag{12}$$

where F_{HYDRO} is the hydrodynamic and hydrostatic pressure force exerted on the body by the surrounding water and ξ denotes the vertical displacement of the body. Therefore, the PTO force will have the opposite sign to the hydrodynamic and hydrostatic pressure force.

To model the experimental PTO force, the experimental test (referred to as test 21-A) involving the isolated device model responding to the crest focussed incident wave corresponding to a full scale energy period $T_e = 11.0s$ and focus amplitude $A = 3m$ is considered. The original PTO force time-history and a filtered time-history is shown in Figure 13 and the corresponding device velocity (obtained by numerical differentiation of the displacement time-history with noise filtering) is shown in Figure 14. From the PTO force time-history it is clear that the exciting force exerted on the structure during the interval $(0s, 6s)$ is not large enough to overcome the target PTO damping force. Therefore, the PTO force during this interval equals the exciting force due to the incident focussed wave and features an underlying long wave oscillation as expected. It is worth noting that the initial displacement of the body is non-zero – the initial position of the body is slightly above equilibrium –

and so the initial PTO force is also initially non-zero (positive) because it opposes the initial (negative) hydrostatic restoring force. The feedback controller causes some high frequency oscillations about the mean value; this aspect of the experimental PTO brake mechanism is not modelled because such oscillations in the force will not have a significant effect on the device motion. In the results that follow the low-pass filtered PTO time-history is used rather than the original time-history.

During the period of significant motion, from $t \simeq 7s$ to $t \simeq 20s$, the PTO force switches between approximately constant positive and negative force as desired. It is worth noting that the RMS force during this period is closer to $0.3N$ than the target force $0.4N$ and this will be taken into account in some of the device performance simulations. The effect of the feedback controller is also evident during the period of significant motion whereby the Coulomb-type 'kinetic friction' force is only approximately constant and contains small, rapid changes about the local constant value. After $t = 20s$ the device motion has decayed towards zero and the PTO brake force signal begins to resemble the initial static resistance force form.

In the OXPOT simulations, the aim of the PTO force implementation is to model the ideal form of the WEC brake and not the experimental form. That is, during the motion of the body the PTO force is a Coulomb-type damping force which opposes the motion of the body with a constant magnitude (the target value or otherwise). Prior to the onset of motion, when the exciting force is smaller than the threshold (target) brake force, the PTO force is specified to exactly oppose the hydrodynamic and hydrostatic pressure forces on the body. No feedback type oscillations will occur in the numerical implementation of the PTO brake. It can be seen from the velocity time-history that the most interesting interactions occur before $t = 20s$. Therefore, we seek to simulate only the first $20s$ of the experimental tests and it is not necessary to model the return of the friction brake force from kinetic to static mode.

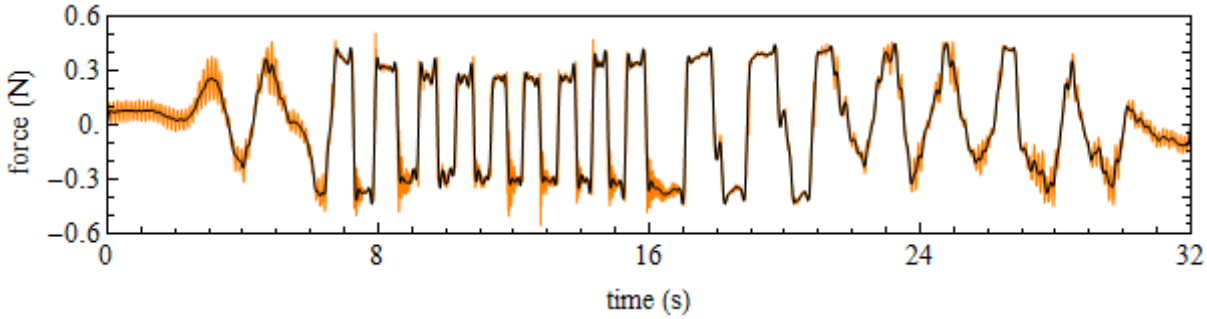

Figure 13: Original PTO force time-history (orange) and low-pass filtered PTO force signal (black) from the isolated device test 21 (A) corresponding to the $T_e = 11.0s$, $A = 3m$ crest focussed ($\varphi = 0°$) wave.

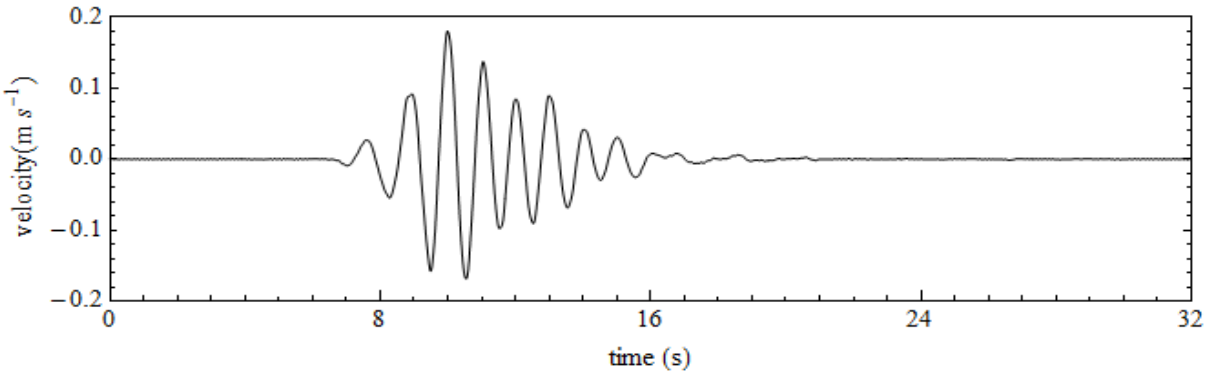

Figure 14: Device velocity time-history in the isolated device test 21 (A).

The algorithm for the PTO force can be expressed as follows:

1. if the exciting force is less than or equal to the target PTO force magnitude $(0.4N)$ and the device is not moving then the PTO force exactly cancels the exciting force;
2. at the instant when the magnitude of the exciting force exceeds the threshold force which typically equals the target PTO force then the PTO force equals a prescribed 'kinetic friction' force in magnitude and opposes the direction of motion of the device.
3. once the device is in motion the PTO force always opposes the motion of the device and has a constant magnitude equal to that of the prescribed kinetic force during motion.

As can be seen from Figure 13, the threshold force which the wave excitation force must exceed to induce motion is approximately equal to the target PTO force. However, during the largest motion of the device the approximately constant PTO force opposing motion is clearly less than the prescribed target force of $0.4N$. For longer simulations, where the device settles back to an equilibrium position, to model the PTO mechanism fully it would be necessary to include a condition for determining when the motion has ceased, e.g. if the magnitude of the velocity is less than a prescribed (small) value for a certain period of time. However, in the simulations featured here this is not considered important or relevant – the behaviour of most interest occurs during the interval of largest motion. Note that in most cases the 'kinetic friction' force is prescribed to equal the target PTO force; however, to improve the power absorption predictions of the OXPOT model it is necessary to match the simulated force during body motion to an averaged measured force from the experimental tests.

4.2 Domain width and mesh fineness on simulation results

The simulations of the wave calibrations tests involved narrow numerical wave tanks of only two elements width. Such numerical wave tanks can be discretised using fine meshes with small elements without leading to large computational times irrespective of time-step sizes. Therefore, it was straightforward to ensure convergence of the results at second order with reasonable third order representation as illustrated in Figure 7. However, for the device performance simulations it is necessary to use a wide numerical wave tank to minimise side wall reflections. (The wider the tank, the longer it will take for diffracted and radiated waves to propagate outwards and return after reflection at the side wall. Furthermore, the amplitudes of the diffracted/radiated waves will decrease according to $r^{-1/2}$ where r is the distance from the centre of the disturbance and so a

wider tank will also lead to smaller side-wall reflections). Therefore, the implementation of wide computational domains was prioritised for the device performance simulations.

To prevent the resultant simulation times from becoming prohibitively long it was necessary to reduce the mesh fineness compared to the wave propagation simulations and the effect on the first and second order results was investigated. Given that the third order component of the focussed wave free-surface elevation was significantly (approximately 50 times) smaller than the second order sum component it was expected that contributions to device response at orders above the second order would be minimal. Therefore, in the performance simulations the aim is to model the first and second order (sum and difference harmonic) components of the incident and diffracted/radiated waves and the first and second order components of the device motion. Analysis of the amplitude spectrum of the displacement time-history for different element and time-step sizes should indicate whether information is lost due to the coarseness of the mesh. The mesh fineness and domain width investigations involve the performance simulations involving the focussed wave of full scale energy period $T_e = 11.0s$ and amplitude $A = 3m$ (corresponding to test numbers 21-24). The conclusions regarding a suitable element size and domain width can be extrapolated to the other wave periods. First, the influence of domain width on the displacement is considered.

4.2.1 Influence of domain width on device displacements

Simulations of device performance in two domain widths were considered to assess the effect of side-wall reflections on the device response. For the focussed waves 21-24 the experimental-scale energy period of the focussed wave is approximately $1.23s$ and the associated wavelength is $2.226m$. The half-width of the narrower and wider computational domains (symmetry is exploited so that only one half of the total domain is simulated) was chosen to be $W = 1.5m$ and $W = 2.5m$, respectively. The free-surface and cylinder element sizes in both domains was specified to be approximately equal with values of $0.1m$ and $0.045m$, respectively, as were the time-step sizes at $\Delta t = 0.02s$, so that the width was the only parameter to change. The full free-surface plot (obtained by reflection of the half-domain about the y-axis) for the two simulations at $t = 11.0s$ is shown in Figure 15. It is clear that the outgoing waves from the cylinder will be reflected at the side walls earlier by the narrower domain. The device displacements for the same incident wave in the two domains are shown in Figure 16. It is evident from this comparison that the displacements become visibly different only after $t \simeq 14s$ when the device motions are relatively small.

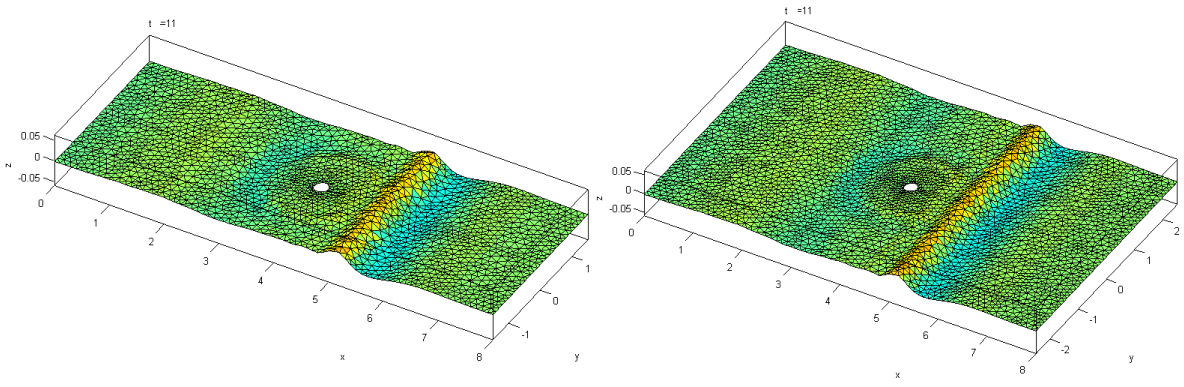

Figure 15: Free-surface plot for the performance simulation of the focussed wave test number 21 for domain half widths of $W = 1.5$ (left) and $W = 2.5m$ (right).

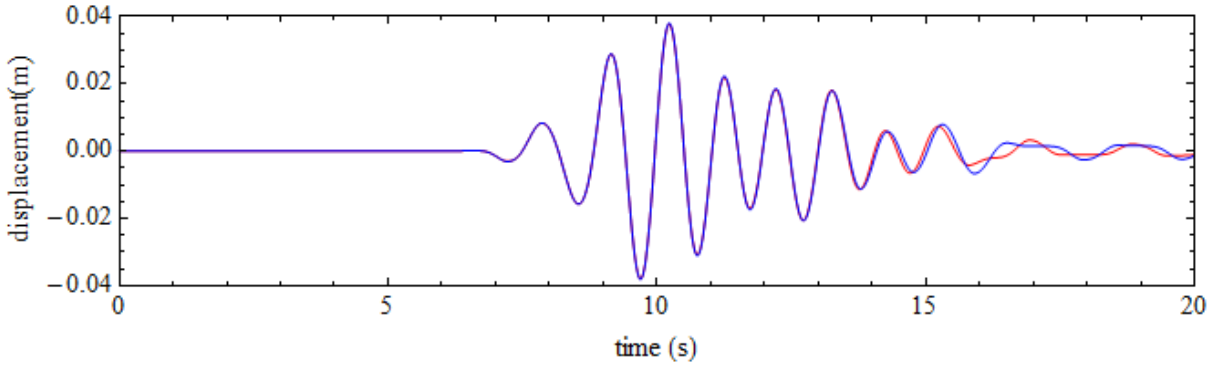

Figure 16: Fully nonlinear device displacement time-histories for simulations of test number 21 with domains of half-width $W = 2.5m$ (blue) and $W = 1.5m$ (red).

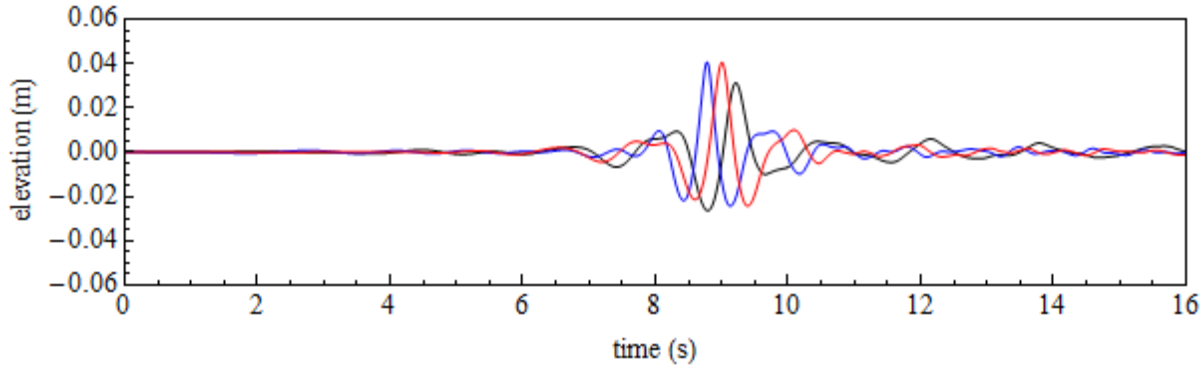

Figure 17: Free-surface elevation at the focus location in the simulations of wave calibration tests 5 (blue), 13 (red), 21 (black).

In the experimental focussed wave tests, due to the width of the tank and the brevity of the tests, the reflected outgoing waves do not interfere with the device motion. Therefore, in an ideal OXPOT simulation of the experimental tests any side-wall reflections would not interfere with the device motion for the duration of simulation. To estimate the time at which side-wall reflections of the radiated/diffracted waves will cause a significant difference in the time-history relative to ideal reflection-free case it is necessary to consider the group velocity of the main component of the focussed wave. The group velocity can be computed from

$$c_g = \frac{\omega}{2k}\left(1 + \frac{2kh}{\sinh 2kh}\right), \tag{13}$$

where k is the wavenumber of the peak frequency component, and for this focussed wave is determined to be $c_g \simeq 1.10ms^{-1}$. The travel time for the main component of the incident wave to radiate/diffract from the cylinder, reach the side-wall and be reflected back to the cylinder is $T_R = 2W/c_g$ which approximately equals $2.75s$ for the domain of half-width $W = 1.5m$ and $4.6.s$ for the domain of half-width $W = 2.5m$. The focussed wave arrives at the device/focus location at around $t = 9.0s$ (as is evident in Figure 17) so that the reflected waves are expected to significantly influence the device from $t \simeq 12s$ and $t \simeq 14s$ for the narrow and wide domain, respectively. However, from Figure 16 it is evident that the device responses differ significantly only after $t \simeq 14s$. This implies that the estimates based on the group velocity of the incident wave are overly-pessimistic and that the influence of reflected waves on the motion is small for reasonably wide

domains (of the order of one peak wavelength) because of the asymptotic decay of radiated circular waves according to $(kr)^{-1/2}$. Given that the device motion has decayed substantially for $t > 16s$, it is deduced that the domain of half-width $W = 2.5m$ is sufficiently wide for the purposes of simulating the device performance tests where the motions of most interest occur for $t \leq 16s$. Note that this domain half-width is greater than the 'energy wavelength', i.e. the wavelength associated with the energy period of the incident focussed wave group, which is $\lambda = 2.26m$ in this case. For the other focussed wave periods ($T_e = 7.0s$ and $T_e = 9.0s$), the domains were chosen to have half-widths of $W = 1.25m$ and $W = 2.0m$, respectively. The estimates for the travel times of the reflected waves are $4.0s$ and $4.8s$, respectively, and given that the focussed waves reach the devices around $9s$ the reflected will begin to influence the device motion around $13s$ and $14s$ respectively. The magnitude of this influence may well be small as in the case considered and the device response is likely to be dominated by the resonant motion excited by the incident wave. The repeatability issues highlighted in section 2.1.2 are more likely to influence the comparison of the numerical and experimental results. For the array simulations the side-wall should be at least the same distance from the cylinders as in the isolated device case.

4.2.2 Mesh fineness and solution convergence

A brief investigation into what constitutes a sufficient mesh fineness (or a sufficiently small average element size) for modelling the interaction accurate to second order was conducted for the interactions involving focussed-wave of energy period $T_e = 11s$ and focus amplitude $A = 3m$. As for the domain width investigation above, the findings will be extended to the array simulations involving the same period and also extrapolated to the isolated device simulations for the focussed waves of periods $T_e = 7s$ and $T_e = 9s$. It is assumed that the mesh determined suitable for a focussed wave of a given period can be utilised for interactions involving such an incident wave irrespective of the focus wave amplitudes.

The simulation results presented thus far utilise what is to be referred to as the 'standard mesh' for the experimental focussed waves corresponding to the full-scale energy period $T_e = 11.0s$. A summary of the most important properties of this mesh is provided in Table 3. The free-surface element length refers to the side-length of the triangular free-surface elements. It is worth noting that on each element there are six nodes; on each element side there are two corner nodes and one mid-point node. The cylinder element length refers to the circumferential length of the quadrilateral elements which discretise the vertical surface as shown in Figure 11. The vertical cylinder surface is discretised in the vertical direction by five quadrilateral elements and the hemisphere mesh involves five vertical elements also. At the intersection of the free-surface and the wall the wall elements have a height of $0.04m$ which is considered sufficiently fine for resolving second order free waves of approximate wavelength $0.6m$. As shown in Table 3, the free-surface element lengths correspond to more than 22 elements per first order wavelength and almost 6 elements per second order (free) wavelength. (At each order the wavelength of the free waves decrease by a factor of approximately 4.)

Mesh Type	Energy period (T_e/T_e^{exp})	'Energy' wavelength (λ_e)	Free-surf. (FS) element length (Δx)	Wall element height at FS (Δz)	Cylinder element arc-length (Δc)	$\lambda_e/\Delta x$
Standard	$11.0s/1.23s$	$2.23m$	$0.1m$	$0.040m$	$0.045m$	22.3
Finer	$11.0s/1.23s$	$2.23m$	$0.0625m$	$0.040m$	$0.030m$	35.6

Table 3: Summary of the element lengths for the standard and fine meshes used in assessing the convergence of the numerical solution.

To effectively assess the accuracy of the numerical solutions for each mesh it is preferable to decompose the fully nonlinear solution into its constituent harmonics. Given that the solution to second order is sought then it is sufficient to decompose the fully nonlinear time-history for the device displacement into the odd and even harmonic signals which will be dominated by the first and second order harmonics, respectively. Therefore, according to equations (3) and (4) it is necessary to combine the displacement time-history from the crest-focussed and trough-focussed wave simulations. The harmonic decomposition is very effective for the free-surface elevation time-signals as evidenced in Figure 7 and has been shown to be effective for wave loadings (Zang, et al., 2010). However, it is not clear if the harmonics of the device displacement can be cleanly separated with a nonlinear PTO affecting the dynamics of the device. In the harmonic decomposition, it is important that the crests and troughs occur at the same times throughout the simulation, i.e. that the displacements for $\varphi = 0^\circ$ and $\varphi = 180^\circ$ are given by

$$\xi_0 = a\xi_{11}\cos(\theta) + a^2(\xi_{20} + \xi_{22}\cos 2\theta) + O(a^3) \tag{14}$$

and

$$\xi_{180} = -a\xi_{11}\cos(\theta) + a^2(\xi_{20} + \xi_{22}\cos 2\theta) - O(a^3), \tag{15}$$

respectively. In this case, when the time-histories are summed, the first order component (and other odd harmonics) of the total signal cancel leaving only the even orders. However, if the presence of the PTO introduces a slight phase shift to the trough-focussed signal relative to the crest-focussed signal then the displacement time-history for the trough focussed wave will become

$$\begin{aligned}\xi_{180} &= -a\xi_{11}\cos(\theta + \delta\theta) + a^2(\xi_{20} + \xi_{22}\cos 2\theta) - O(a^3), \\ &= -a\xi_{11}\cos\theta - \delta\theta a\xi_{11}\sin\theta + a^2(\xi_{20} + \xi_{22}\cos 2\theta) - O(a^3)\end{aligned} \tag{16}$$

and hence

$$\frac{q_0 + q_{180}}{2} = -\delta\theta(a\xi_{11}\sin\theta) + a^2(q_{20} + q_{22}\cos 2\theta + O(a^3). \tag{17}$$

The presence of a small element of the first order components is sometimes referred to as 'leakage' and it also may occur for third order components. If the second order signal is sufficiently small then the time-signal for the displacement will be dominated by the leakage from the first order term.

In order to illustrate this, it is useful to apply the harmonic separation formulae (equations (3) and (4)) to a pair of displacement time-histories from the crest and trough focussed interaction simulations and to consider the amplitude spectra of these signals. Therefore, a trough-focussed simulation was generated as a counterpart to the wide-domain simulation from which the results illustrated in Figure 16 are taken. The time-histories for $(\xi_0 - \xi_{180})/2$ and $(\xi_0 + \xi_{180})/2$ are shown in Figure 18 and the corresponding spectra are illustrated in Figure 19. A cursory inspection of the displacement time-history for Figure 18 (b) shows a clear second order difference trough around

$t = 9.0s$. However, there are oscillations from $t = 10$s onwards which have the same period as the linear oscillations – a clear example of leakage from the linear component of the fully nonlinear signal. No second order sum component is evident in the displacement time-history. The small peak in the semi-log spectral plot of the amplitude of the $(\xi_0 + \xi_{180})/2$ signal at the first order peak frequency confirms the presence of a linear component in the intended even harmonic signal. However, the low-frequency peak in the spectra of the intended even harmonic signal shows that the harmonic separation is not completely unsuccessful. Furthermore, a broad maximum around the second order sum frequency is also evident in the spectrum and so it may still be useful to compare the spectra of the intended odd harmonic signal $(\xi_0 - \xi_{180})/2$ and the intended even harmonic signal $(\xi_0 + \xi_{180})/2$ for different element or time-step sizes in order to demonstrate convergence of the solutions to second order. If a leakage term from the first harmonic is present in the $(\xi_0 + \xi_{180})/2$ time history and it dominates the second harmonic contribution then the time-history will provide no insight into the importance of the second harmonic and nonlinearity in general. Instead, an analysis of the amplitude spectrum of the time-history will be the most useful method of assessing the importance of nonlinearity.

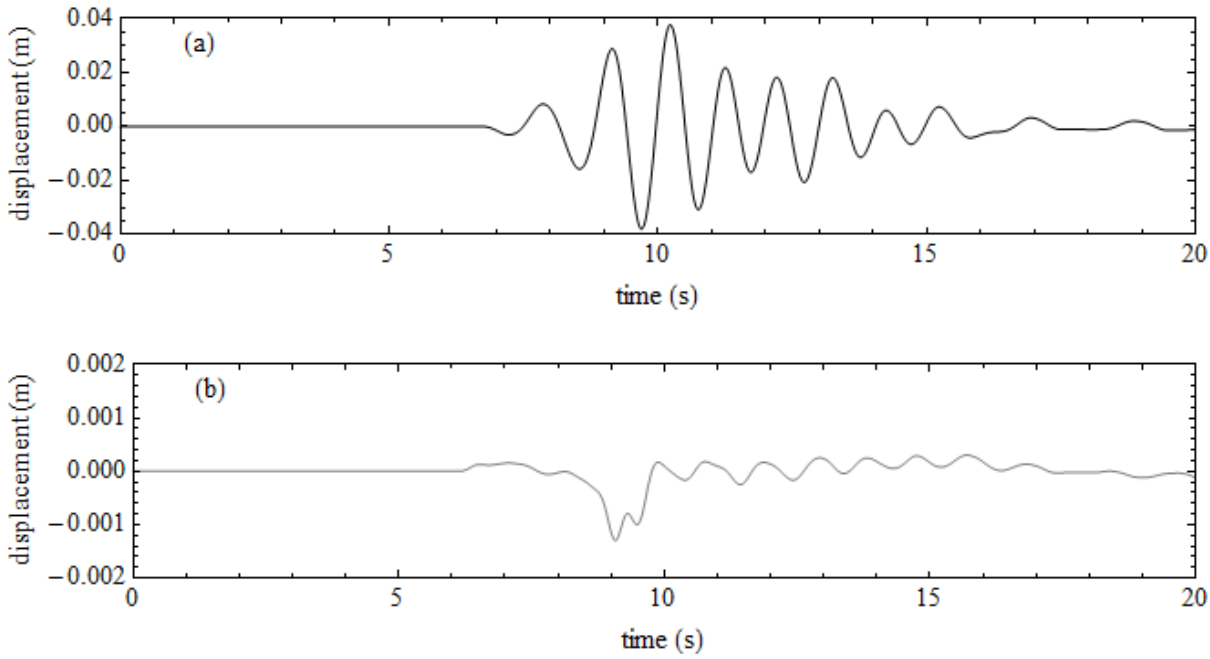

Figure 18: Combined devic e displacement time signal (a) $(\xi_0 - \xi_{180})/2$ and (b) $(\xi_0 + \xi_{180})/2$ for the crest and trough focussed simulations of the focussed wave of full scale period $T_e = 11.0s$ and amplitude $A = 3.0m$.

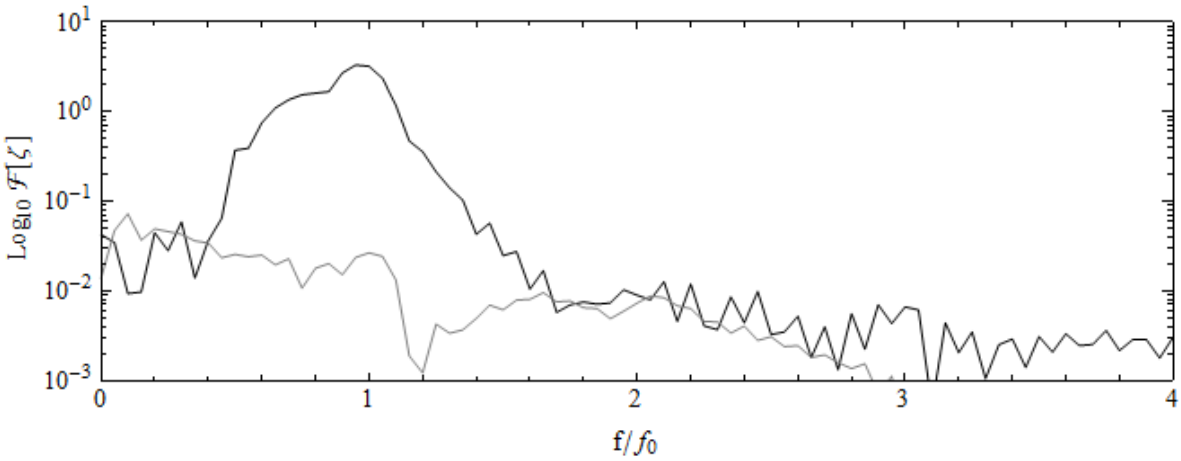

Figure 19: Semi-log plot of the amplitude spectra of the time-histories shown in Figure 18(a) (black) and Figure 18(b) (gray).

The device response in a narrow computational domain ($W = 1.5$) discretised using the standard mesh and fine mesh described in Table 3 is compared next. The harmonic decomposition formulae, $(\xi_0 - \xi_{180})/2$ and $(\xi_0 + \xi_{180})/2$, for the odd and even harmonics, respectively, were applied to the crest and trough focussed responses despite the previous caveat regarding 'leakage'. The amplitude spectra for the standard mesh and fine mesh results are shown in a semi-log plot for the odd harmonics in Figure 20. The spectral agreement for the intended odd harmonic response $(\xi_0 - \xi_{180})/2$ is excellent with only small discrepancies around $f = 2f_0$. It is clear that the solution has converged at first order. The agreement is not as good for the even harmonic response $(\xi_0 + \xi_{180})/2$ where there is an obvious discrepancy at the first harmonic frequency. That is, the discrepancy in the even harmonic amplitude spectra is due to differences in the leaked component denoted $-\delta\theta(a\xi_{11}\sin\theta)$ in equation (17). However, the agreement between the response spectra at the second order sum and difference frequencies is very good. This indicates that the standard mesh is sufficiently fine for the resolution of any second order nonlinearity. Nevertheless, the second order sum contributions are extremely small and will, in this case at least, contribute very little to the dynamics of the device. The mesh used in the subsequent performance simulations for the incident focussed waves of full-scale energy period 11.0s is the standard mesh(4) described in Table 3. For the other incident wave periods, the mesh elements will be scaled according to the wavelength of the incident waves so that the number of elements per wavelength is approximately the same as the $T_e = 11.0s$ case.

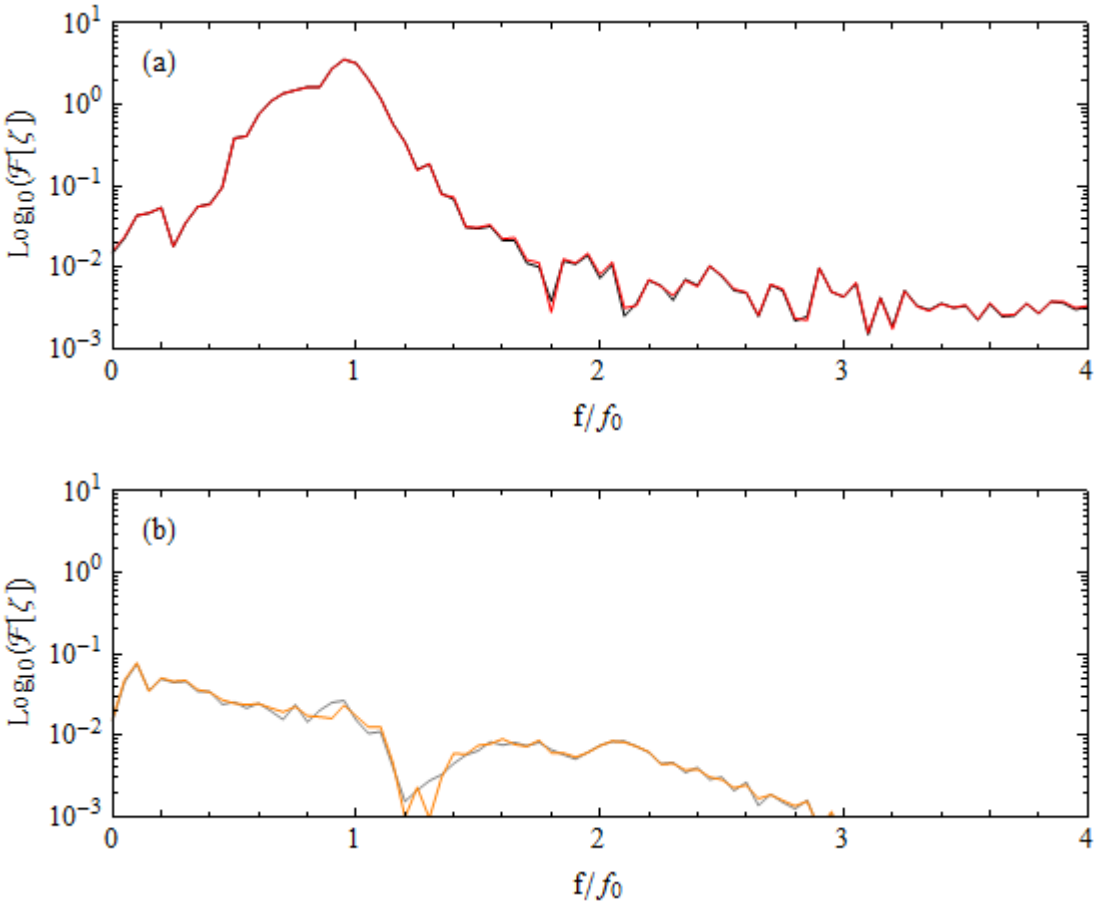

Figure 20: Semi-log plot of the amplitude spectra of the (a) odd harmonics and (b) even harmonics of the device response in the narrow computational domain discretised with a fine mesh (red and orange) and the standard mesh (black and gray).

4.3 Comparison of numerical and experimental performance results

In the following, the device displacement, power take-off force and instantaneous power absorbed obtained from the OXPOT simulations is compared to the corresponding test data for a subset of the focussed waves listed in Table 1. The cases of most interest are the large amplitude $A = 3m$ simulations for $T_e = 7.0s$ (test numbers 5-8), $T_e = 9.0s$ (test numbers 13-16), $T_e = 11.0s$ (test numbers 21-24) and the final set $A = 4.0m$ for the period $T_e = 11.0s$ (test numbers 25-28). Details of the computational domains for each focussed wave period are provided in Table 4. Notice that the number of elements per wavelength (the last column in the table) is approximately the same for each period, thus ensuring that the conclusions regarding the solution convergence in section 4.2.2. are satisfied. Rather than using a single experimental test case for comparison with the OXPOT predictions, the mean values of the device displacement, PTO force and power absorption values over the set of ten repeated tests is considered. It should be noted that in the case of test number 25 there are only 3 repetitions of the performance test.

The instantaneous power absorbed is obtained by multiplying the PTO force and the device velocity at every time-step. In the OXPOT simulations, the velocity of the device is output so calculating the instantaneous power absorbed is straightforward. For the physical model tests, only the displacement and PTO force are output so it is necessary to derive the velocity from the displacement time-history. This is achieved using the combination of numerical differentiation and a

low pass filter. Given the erratic nature of the PTO force time-history it is also necessary to obtain a low-pass filtered form of the PTO time-history.

Energy period (T_e/T_e^{exp})	'Energy' wavelength (λ_e)	Free-surf. (FS) element length (Δx)	Wall element height at FS (Δz)	Cylinder element (Δc)	Domain width (W)	$\lambda_e/\Delta x$
$7.0s/0.783s$	$0.955m$	$0.0391m$	$0.0291m$	$0.025m$	$1.25m$	24.8
$9.0s/1.01s$	$1.56m$	$0.067m$	$0.040m$	$0.030m$	$2.00m$	23.4
$11.0s/1.23s$	$2.23m$	$0.100m$	$0.040m$	$0.045m$	$2.50m$	22.3

Table 4: Specifications for the single device performance test simulations for each of three incident focussed wave energy periods.

4.3.1 $T_e = 11.0s, A = 3m$

The first set of performance test simulations to be analysed involve the focussed wave with the longest energy period $T_e = 11.0s$. The computational domain of half width $W = 2.5$ is discretised using the standard mesh described in the last section (see Table 3) and the time-step was specified to be $0.02s$. The PTO force magnitude for the first simulation was specified to equal the target PTO force for the test programme $(0.4N)$ both when the device was static and when it was moving. A comparison of this simulation, referred to as 'T11A3_0' with the experimental results is shown in Figure 21. The OXPOT displacement results over-predict the amplitude of the device motion and during the period of significant device motion the applied PTO force in the experiment is significantly smaller than the target force. Given that both the velocity and PTO force are over-predicted by OXPOT, it is not surprising that the power absorbed is predicted to be significantly larger than the derived test value throughout most of the simulation. Nevertheless, the phases of the OXPOT time-histories of the displacement, PTO force and power absorbed agree very well with the measured values. To measure the accuracy of the simulation results in modelling the experimental behaviour, both the r.m.s. displacement and the mean power capture are computed over the first 20 seconds of the experimental test and numerical simulations and are compared in Table 5. The relative difference between the numerical and experimental r.m.s. displacement and mean power capture results is also provided in alignment with the acceptance criteria. The first OXPOT simulation is denoted 'T11A3_0' and the associated over-estimates for the r.m.s. displacement and the mean power capture are 18% and 79%, respectively.

To improve the agreement between the simulated and experimental brake force the root mean squared (r.m.s.) value of the experimental PTO force for the duration of significant motion of the device was used as simulation input rather than the target brake force of $0.4N$. This interval of significant motion was chosen to be $t = (6s, 16s)$ and the associated r.m.s. PTO force value was determined to be $0.304N$. To understand how much influence the PTO force discrepancy has on the power absorbed comparison, this new simulation (T11A3_1) with the adjusted PTO force was also compared to the experimental results in Figure 21. It is clear from this figure that there is a significant improvement in the mean power capture values when the PTO force is modelled more effectively using the r.m.s. experimental value. However, the behaviour of the PTO force around $t = 5s$ is much more erratic because the incident wave exciting force instantaneously exceeds the PTO brake force by a small amount causing the device to move. The PTO model switches to a kinetic mode where the PTO always opposes the motion of the body. Since the device moves only a small

amount and the wave exciting force is still small this results in erratic, small motions of the body and an erratic PTO force signal.

The mean power absorbed and r.m.s. displacement results for this simulation are presented in Table 5. Simulation 'T11A3_0' over-predicts the mean power absorbed by 79% whereas the adjusted model 'T11A3_1' over-predicts the mean power absorbed by 48%. In contrast, the r.m.s. displacement for the simulation T11A3_0 is 18% greater than the experimental value whereas for T11A3_1 the over-estimate is 25% – this slight increase in the displacement amplitude is due to the reduction in damping as a result of the decrease in the PTO brake force. It is clear from a comparison of the mean power absorbed that any differences in the simulated and test PTO force will significantly affect the power absorption comparison. Therefore, to measure the accuracy of the fully nonlinear prediction of the experimental behaviour it is more useful to compare the r.m.s. displacements than the mean power absorbed. Nevertheless, a summary of the results is provided in Table 5 which includes OXPOT and experimental values for both displacement and power absorption.

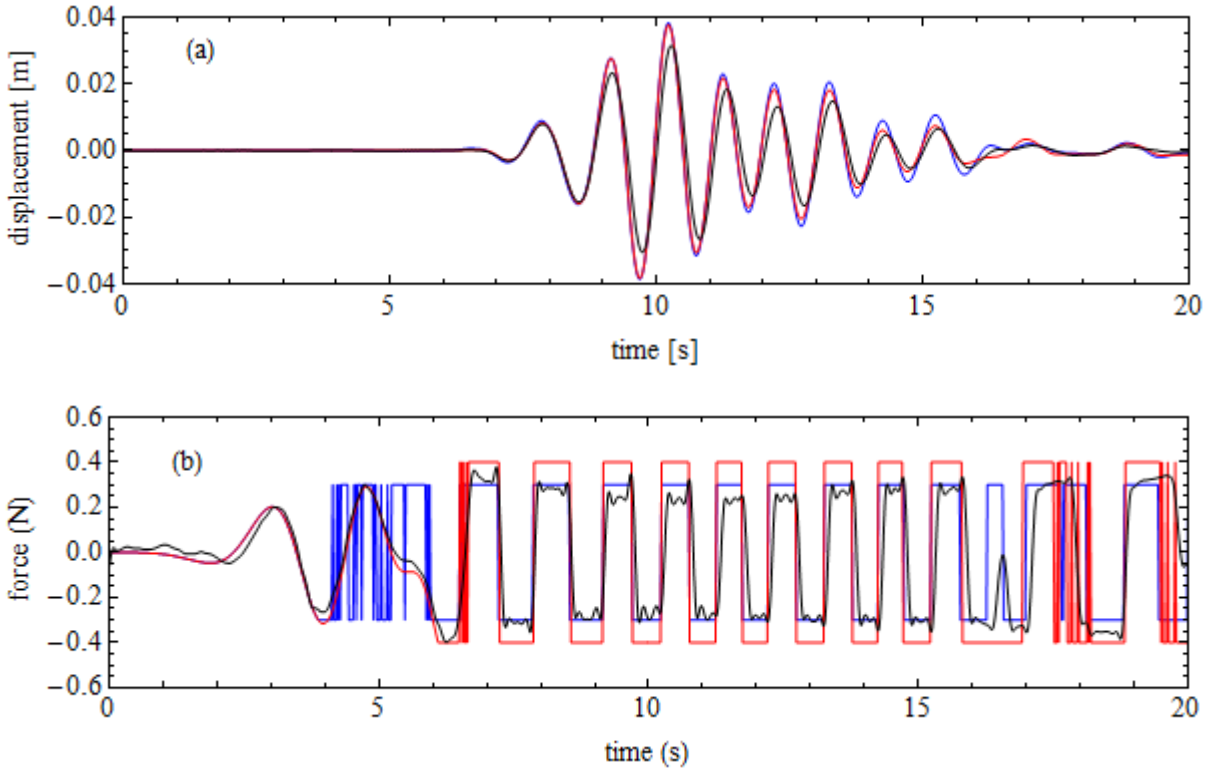

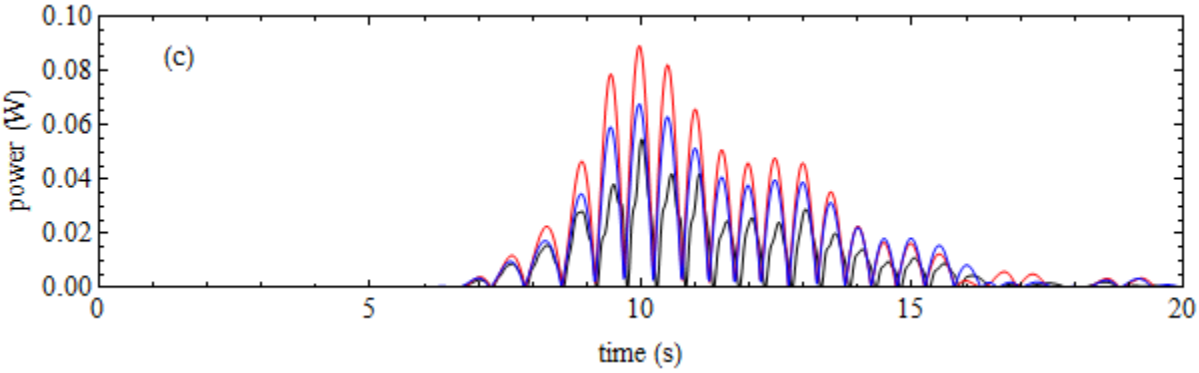

Figure 21: Comparison of OXPOT simulation results T11A3_0 (red) and T11A3_1 (blue) and test measurement data (black) for (a) the device displacement, (b) the PTO force, (c) the power absorbed for test number 21.

Interaction	**PTO force [N] (device motion)**	**Frictional losses/ External damping**	**RMS displacement [m]**	**Mean power capture [W]**
Experiment	0.304	Yes	0.00820	0.00666
T11A3_0	0.400/0.400	$c_F = 0.0Nm^{-1}s$	0.00973 (+18%)	0.01200 (+79%)
T11A3_1	0.304/0.304	$c_F = 0.0Nm^{-1}s$	0.01024 (+25%)	0.00987 (+48%)
T11A3_2	0.400/0.304	$c_F = 1.75Nm^{-1}s$	0.00904 (+10%)	0.00830 (+25%)

Table 5: Experimental and simulation results for performance test number 21 (focussed wave with full scale energy period $T_e = 11s$ and amplitude $A = 3m$).

In Table 5, the PTO force value provided for the experimental test is equal to the r.m.s. value during the interval of most significant motion, i.e. between 6s and 16s. Two OXPOT values are provided – the first is referred to as the static brake force and the second is the 'kinetic brake force' and these correspond to the force applied to the body prior to the onset of significant motion and after the onset of significant motion. Two parameters are necessary given that the experimental PTO brake force varies quite considerably over the course of the performance test. The frictional losses/external damping column refers to the presence of other sources of frictional losses in the system apart from the PTO brake force. In the case of the experiments, such frictional losses exist but are difficult to quantify and this is discussed in more detail next.

The discrepancy in the device displacement amplitudes predicted by OXPOT and the experimental results, as seen in Figure 21 (a), are presumably due to energy losses from the model motion arising from such sources as friction in the air bearing and viscous losses in the water. As OXPOT is a potential flow code, the effects of viscosity are not included in the model of the interaction and, apart from the PTO brake force, no other friction in the physical model has been accounted for in the equation of motion of the device. To model these auxiliary frictional losses it is necessary to include a damping term in the equation of motion. Therefore, an external (linear) damping term can be included in the equation of motion, involving a linear damping coefficient denoted c_F. (The linear damping term is very simple representation of energy loss from the system. It is not an accurate representation of the frictional and viscous losses which will have a quadratic component.) Values for the linear damping coefficient are presented for each simulation in Table 5.

To improve the model of the experimental behaviour a simulation (T11A3_2) including a term to account for the frictional losses and the variation in the PTO brake force term over the test was conducted. The PTO threshold force during the static phase and for the initial motion (until $t = 8.0s$) was prescribed to equal $0.4N$ and thereafter to equal $0.304N$. A linear damping coefficient of $c_F = 1.75\ m^{-1}s$ was also specified. The results of this simulation 'T11A3_2' are shown in Figure 22 and it can be seen that both the displacement and PTO force agreement is better than for the previous simulations. The improvement in the OXPOT estimate of device behaviour is also borne out in the results in Table 5. A larger damping coefficient may improve the agreement further but to determine the optimal damping coefficient would require a large number of simulation runs. OXPOT is not an ideal tool for such an investigation as the computational times are relatively long.

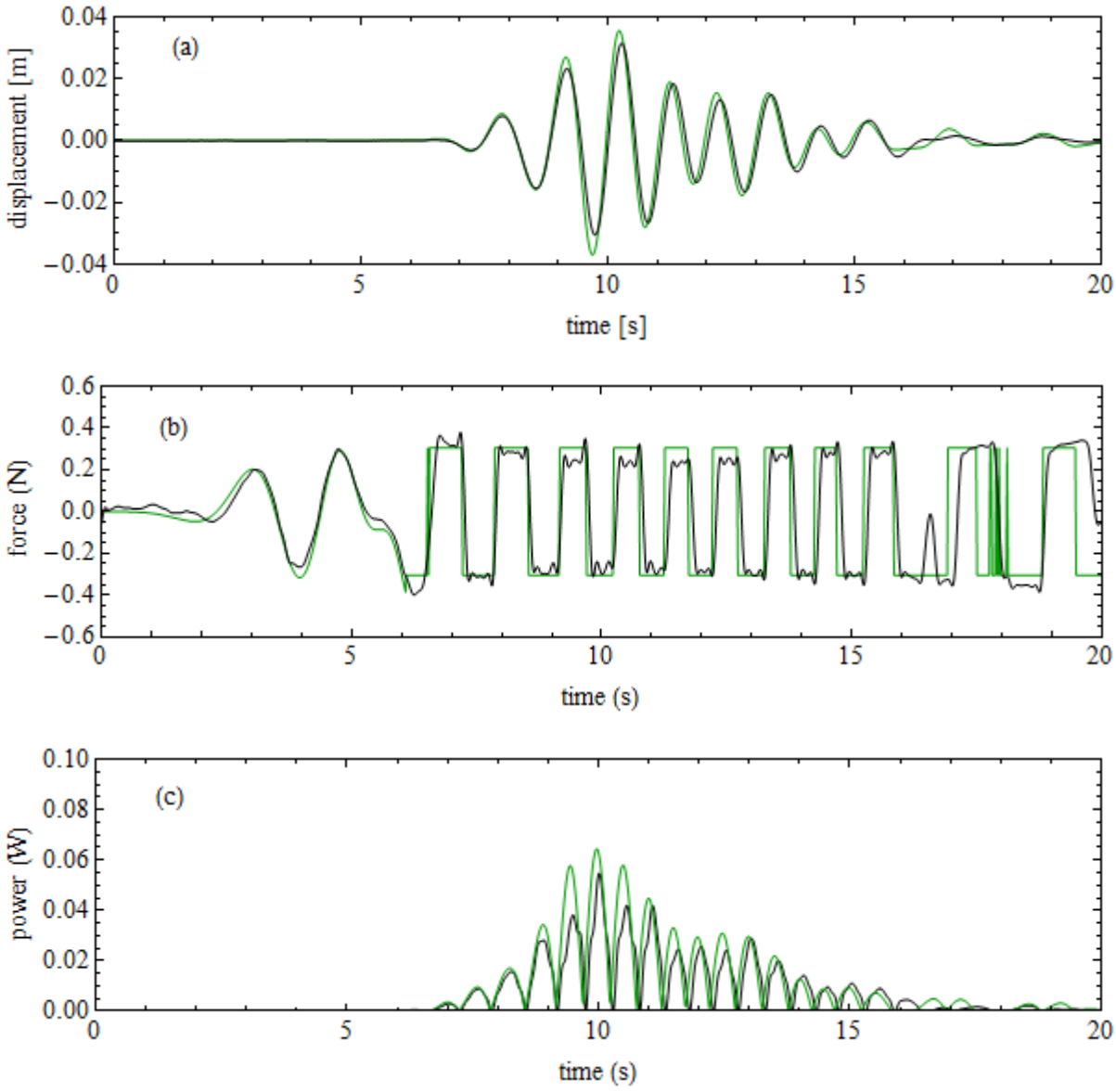

Figure 22: Comparison of OXPOT simulation T11H3_2 (green) and test measurement data (black) for (a) the device displacement, (b) the PTO force, (c) the power absorbed for test number 21.

4.3.2 $T_e = 11.0s, A = 4m$

The mesh and time-stepping specifications for the simulations of the performance test number 21 involving the focussed wave of full scale energy period $T_e = 11.0s$ and focus amplitude $A = 3m$ (outlined in the last subsection) were also utilised for the simulations of test number 25 involving the focussed wave of the same period and focus amplitude $A = 4m$. Therefore, it was necessary to change only the wavemaker input signal to obtain a new set of results for comparison with the experimental data for test number 25.

The results of two simulations are presented with the corresponding experimental data in Figure 23. In the first simulation (referred to as T11A4_0), the PTO brake force was specified to have the target threshold value of $0.4N$ throughout the simulation and no term was present to account for frictional losses. In the second simulation (referred to as T11A4_1), the PTO brake was specified to have a static threshold value of $0.44N$ and a magnitude of $0.308N$ during significant motion after $t = 8.0s$. A linear damping term with a coefficient of $c_F = 2.5Nm^{-1}s$ was also included in the equation of motion of the device to model frictional losses in the physical model. The magnitude of the PTO brake force was obtained by taking the r.m.s. value of the PTO force data during the interval $t = (8s, 16s)$. As was the case previously, the OXPOT simulation without a term to model frictional losses yields a device displacement with a larger amplitude than the experimental displacement time-history. However, the prescribed linear damping coefficient is not large enough to accurately account for the frictional losses and so the discrepancy between simulation and experimental r.m.s. displacement values is quite large in both cases as can be seen in Figure 23. Furthermore, the standard PTO model involving the target threshold and friction force of $0.4N$ is larger than the measured PTO brake force during the most significant motions of the device. The addition of a damping term and the specification of PTO brake force model based on the experimental data yields a better agreement between the amplitudes of the displacement and PTO force time-histories. Therefore, the instantaneous power absorption obtained from simulation 2 gives a much better agreement with the experimental data as can be seen in Figure 23(c). The results of the simulations and the experimental test are summarised in Table 6.

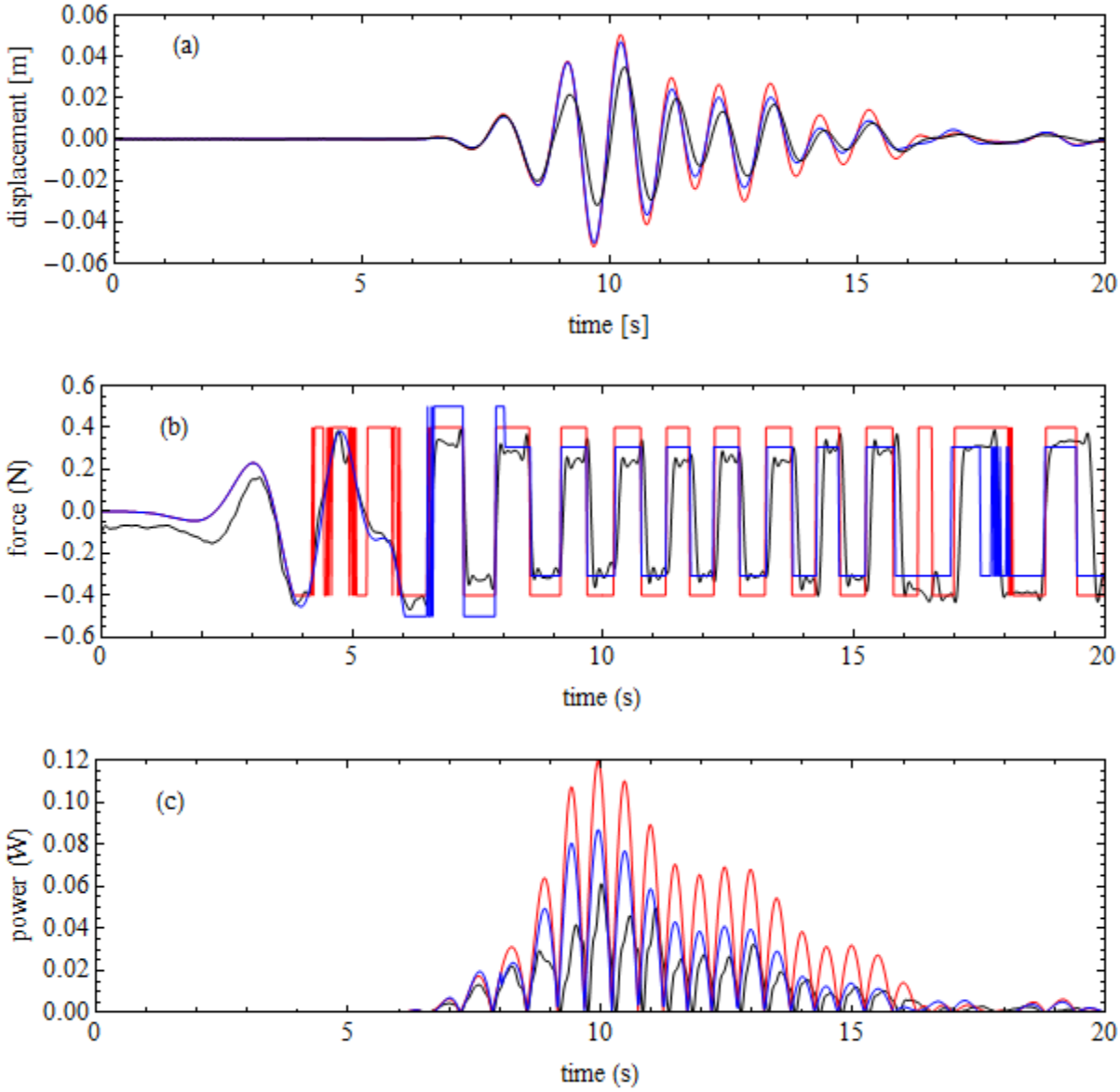

Figure 23: Comparison of OXPOT simulation results (red for T11A4_0 and blue for T11A4_1) and test measurement data (black) for (a) the device displacement, (b) the PTO force, (c) the power absorbed for test number 25.

Interaction	PTO force [N] (device motion)	Frictional losses/ External damping	RMS displacement [m]	Mean power capture [W]
Experiment	0.308	Yes	0.888	0.00805
T11A4_0	0.400	No	0.01360 (+52%)	0.0174 (+127%)
T11A4_1	$0.5/0.308$	$c_F = 2.5Nm^{-1}s$	0.0120 (+36%)	0.0115 (+49%)

Table 6: Experimental and simulation results for performance test number 25 (focussed wave with full scale energy period $T_e = 11s$ and amplitude $A = 4m$).

4.3.3 $T_e = 9.0s, A = 3m$

The focussed waves in the tests numbered 9 – 16 have an energy period $T_e = 9.0s$ close to the resonant period of the device (approximately equal to $10s$). Simulations of the set of tests involving the larger amplitude focussed waves ($A = 3m$) only were conducted because the small amplitude ($A = 1m$) experimental tests did not result in significant device motions. The computational domain of half width $W = 2.0$ is discretised using the mesh the properties of which are summarised in Table 4. A time-step of $0.01s$, corresponding to $1/100th$ of an energy period, was prescribed. As discussed in section 3.3, a coarser time-step could have been used; however, it was considered useful to model the directional switches of the PTO brake force as accurately as possible and so the smaller time-step was chosen. (In the more computationally intensive array simulations the coarser time step was used.)

Two OXPOT simulations of the crest-focussed interaction are here compared to the experimental results. These simulations, consistent with the comparison in the last two subsections, comprise a target PTO force and zero-added-friction case (T9A3_0) and a model with an r.m.s. experimental PTO brake force value during the device motion in conjunction with an added-friction/damping term in the equation of motion of the model (T9A3_1). The modified PTO model specifies the initial PTO force to equal the target force and after $t = 8.0s$ to equal the r.m.s. brake force between $t = 7.0s$ and $t = 15.0s$ in the experiment results. This value was determined to be $0.306N$. A small frictional force was also included in this model. An illustration of the experimental results, the first OXPOT simulation with the basic PTO force algorithm (T9A3_0) and with the modified PTO force algorithm (T9A3_1) are shown in Figure 24. A summary of the mean properties of the experimental and numerical results is shown in Table 7. The mean values are obtained from the first 16s of the experimental and numerical data. The frictional losses in the system clearly have a large effect on the motion of the device in this case – larger than in the longer period focussed wave interactions considered previously. To obtain a more accurate representation of the behaviour it will be necessary to introduce an improved model of the frictional losses (possibly involving a combination of quadratic and linear damping terms). However, such an investigation was not possible given the scope of the deliverable which requires the array results to be analysed also.

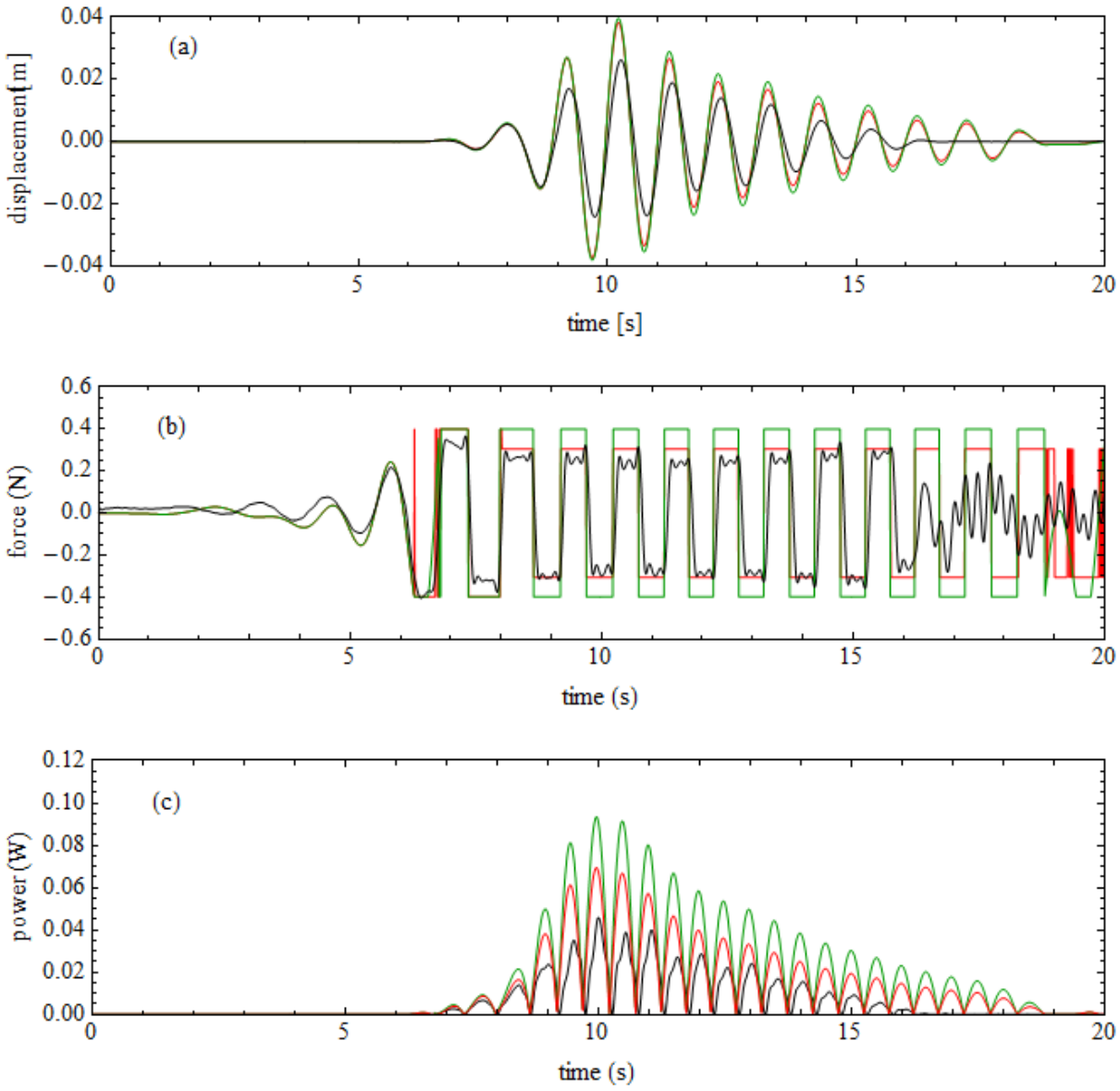

Figure 24: Comparison of OXPOT simulation results (green for T9A3_0 and red for T9A3_1) and test measurement data (black) for (a) the device displacement, (b) the PTO force, (c) the power absorbed for test number 13.

Interaction	PTO force [N] (device motion)	Frictional losses/ External damping	RMS displacement [m]	Mean power capture [W]
Experiment	0.306	Yes	0.0056596	0.00464574
T9A3_0	0.400/0.400	No	0.0119 (+71%)	0.0137 (+139%)
T9A3_1	0.400/0.306	$c_F = 1.5Nm^{-1}s$	0.0111 (+60%)	0.097 (+69%)

Table 7: Experimental and simulation results for performance test number 13 (focussed wave with full scale energy period $T_e = 9s$ and amplitude $A = 3m$).

4.3.4 $T_e = 7.0s, A = 3m$

A simulation of performance test number 7, involving the incident (trough) focussed wave with full scale energy period $T_e = 7.0s$ and amplitude $A = 3m$, with domain specifications provided in Table 4 was also conducted as part of the single device investigation. The time-step was specified to be

$0.01s$ corresponding to approximately 80 time-steps per experimental energy period. In this simulation the PTO force was prescribed to have a threshold value equal to the experimental target value while the device is static and the same constant target value as soon as the threshold is exceeded and the device begins to move. No linear external damping was included in the equation of motion to model the effects of the auxiliary friction/viscous losses in the interaction. The results for this simulation (T7A3_0) are compared to the corresponding experimental data in Figure 25. In this particular test, the basic PTO model provides an excellent representation of the experimental force as can be seen in Figure 25 (b). However, the experimental device motion is much smaller than that predicted by OXPOT and so there is a large discrepancy in the power absorption prediction also. The discrepancy is larger than for both the $T_e = 9.0s$ and $T_e = 11.0s$ comparisons. The mean properties of the experimental and numerical tests over the first 16s of the simulation are presented in Table 8.

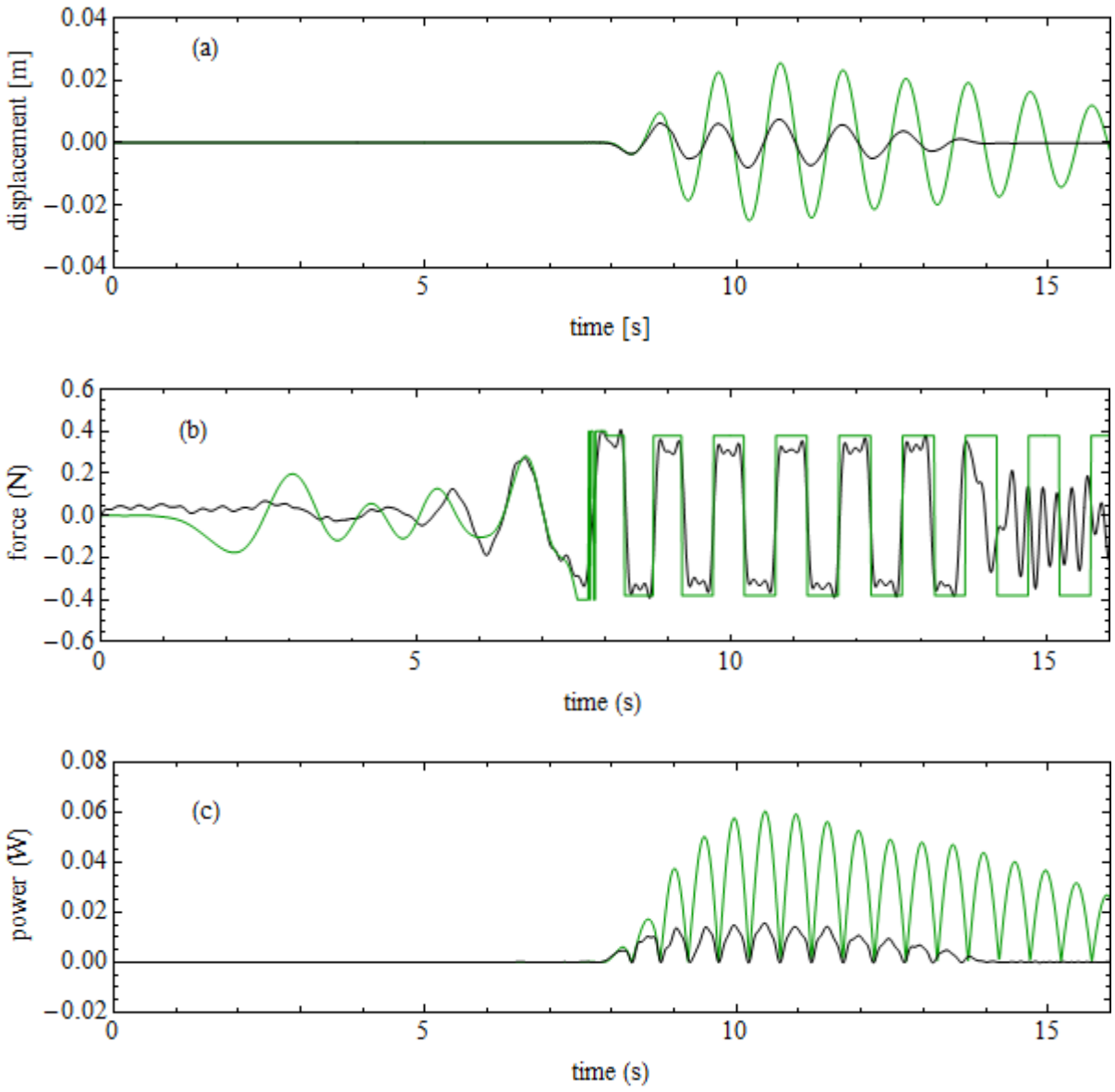

Figure 25: Comparison of OXPOT simulation results (green for T7A3_0) and test measurement data (black) for (a) the device displacement, (b) the PTO force, (c) the power absorbed for test number 7.

Interaction	PTO force [N] (device motion)	Frictional losses/ External damping	RMS displacement [m]	Mean power capture [W]
Experiment	0.4	Yes	0.00302289	0.00227196
T7A3_0	0.400/0.400	No	0.0960 (+234%)	0.0111 (+469%)

Table 8: Experimental and simulation results for performance test number 7 (trough focussed wave with full scale energy period $T_e = 7s$ and amplitude $A = 3m$).

4.4 Variation in the amplitudes of experimental device displacement results

The discrepancy between the OXPOT predictions and the experimental results is quite significant for the performance test involving the focussed wave of full-scale energy period $T_e = 7.0s$. However, as mentioned in section 2.1.2 and shown in Figure 3, the variability in the device displacement amplitude is also significant for the ensemble of repeatability tests. Given that the PTO force time-histories do not possess the same level of variability within the ensemble of repeatability tests, this suggests that undesirable friction losses of varying magnitudes are affecting the device response. In the cases where the motion is largest, it can be supposed that the friction losses are smallest given that the energy imparted to the system is the same in each test and that the device responds in a manner closer to that modelled in OXPOT (where the only damping occurs through the PTO brake). An illustration of the device displacement and PTO brake force between $t = 6s$ and $t = 16s$ for the performance tests yielding minimum and maximum device response is shown in Figure 26. The PTO brake force magnitude is much smaller than the total wave force and so a small change in the PTO force as shown in Figure 26 (b) should not cause such a large difference in the device displacement amplitudes as shown in Figure 26 (a). Therefore, it can be concluded that parasitic frictional losses are strongly influencing the device motion. It is also worth mentioning that for the interactions involving waves of smallest periods, the velocity of the device will be larger relative to the displacement than for the longer periods and so viscous effects might also be larger for these interactions.

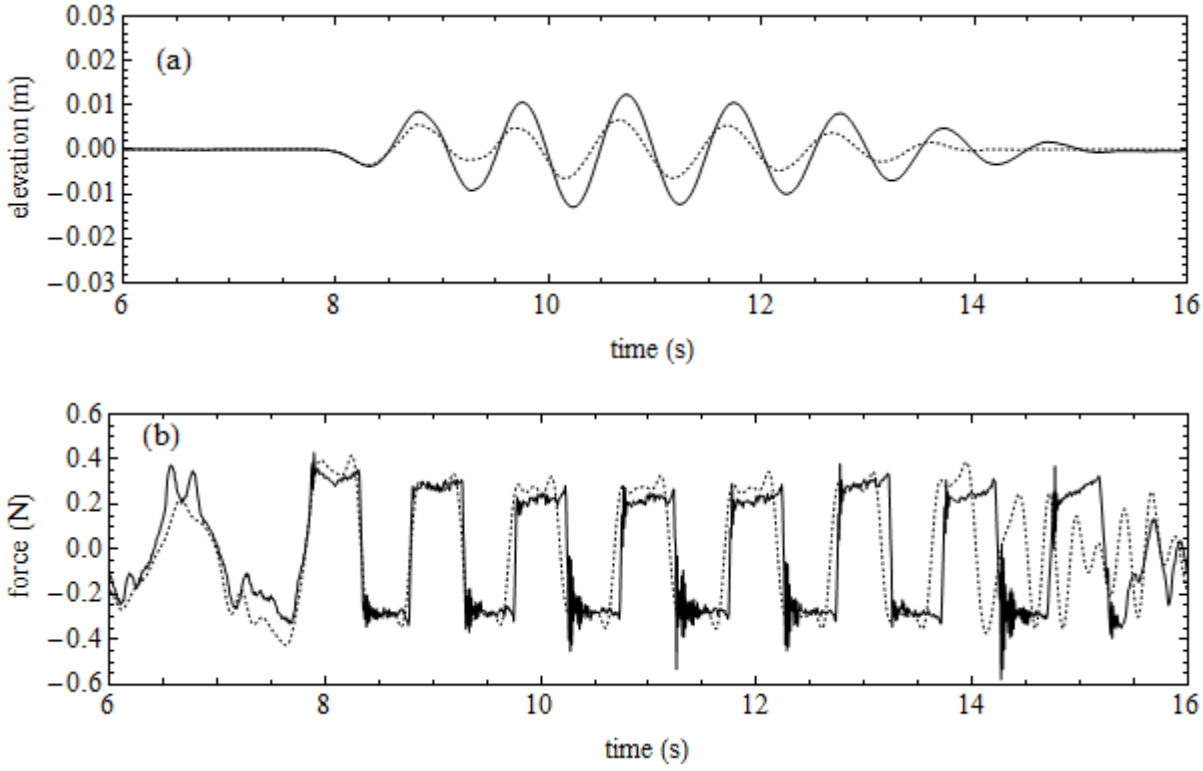

Figure 26: (a) Device displacement and (b) PTO brake force results from the OXPOT simulation (green), from the performance test with maximum response (black, solid) and from that with minimum response (black, dashed) for focussed wave of full-scale energy period $T_e = 7.0s$ and full scale amplitude $A = 3m$.

4.5 Influence of hydrodynamic nonlinearity on the device response

The influence and magnitude of hydrodynamic nonlinearity in the wave calibration tests was easily obtained from the experimental and fully nonlinear simulation time-histories for the free-surface elevation provided data for the four phase realisations was available. The magnitude of the nonlinear components of the free-surface elevation can be observed in Figure 7 with the linear component provided for reference. A semi-log plot of the amplitude spectrum as provided in Figure 8 also provides an insight into the structure of the nonlinearity in the wave propagation tests.

However, as discussed in section 4.2.2, the nonlinear PTO force acting on the body means the harmonic separation approach used for the free-surface elevation is not entirely effective for the fully nonlinear device displacement time-history. Therefore, it is very difficult to separate the linear and second order responses. Components of the response occurring at the second harmonic frequency may also arise from the nonlinearity in the equation of motion due to the PTO brake force. However, the brake force magnitude is quite small relative to the total hydrodynamic force on the body and so it is likely that any observable nonlinearity in the response arises from the nonlinearity in the incident focussed wave.

Therefore, the device response for the performance test simulation involving the incident focussed wave of full-scale energy period $T_e = 9.0s$ and full-scale focus amplitude $A = 3m$ is analysed. The

nonlinearity coefficient $\varepsilon = H/\lambda$ for this incident wave is 0.048 indicating a moderately nonlinear wave. The Fourier transform of the fully nonlinear device displacement as obtained from OXPOT is shown in Figure 27. A clear, although relatively broad, peak at the second order harmonic is evident and also a peak at third order. The latter occurs in the noisy tail of the signal and may not be due to hydrodynamic nonlinearity. Irrespective of the source of the small second order and third order peaks, it can be observed that these peaks are at least two orders of magnitude smaller than the first order peak. Therefore, it can be concluded that the influence of nonlinearity on the response of the device is minimal in this case. Similar amplitude spectra are observed for the device displacement results obtained from the performance test simulations of the focussed wave cases ($T_e = 11.0s, A = 4.0m$) and ($T_e = 7.0s, A = 3.0m$). The device motion in the experimental tests is subject to significant frictional damping and so the motion amplitudes are smaller and nonlinear effects are reduced.

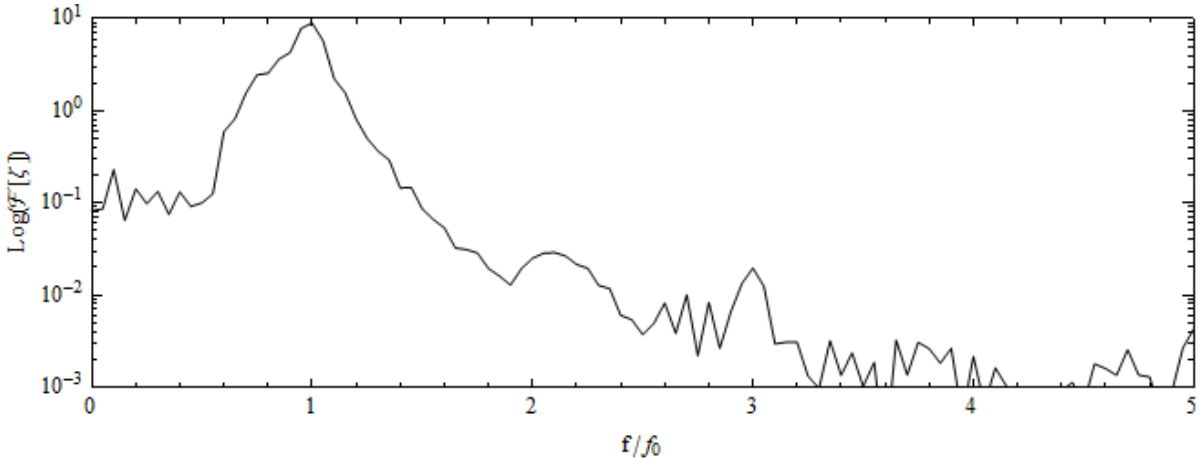

Figure 27: Semi-log plot of the amplitude spectrum of the device displacement time-history for simulations of performance test 13.

5 Array performance tests and simulations

5.1 Experimental array tests

The performance of a four device array subject to the same incident focussed waves as were used in the isolated device tests was also investigated as part of the experimental programme described in WG2 WP2 D5. The devices in the array are identical to the single device models described in section 2. The layout of the four device array is shown both in schematic form and as discretised in the OXPOT simulations in Figure 28 (a) and (b), respectively. In this report, the device indices are prescribed as shown in Figure 28 – in the experiment a slightly different numbering system was used. The centre-to-centre distance of adjacent devices (i.e. devices on the sides of the square) is $750mm$ corresponding to three device diameters and the direction of the incident focussed waves is perpendicular to the sides of the square array so that $\beta = 0$. To describe the position of the centre of the cylinder on the free-surface a Cartesian coordinate system was introduced with the origin at the centre of the tank on the wavemaker and with the x coordinate aligned perpendicular to the wavemaker in the direction of wave incidence. In this coordinate system, device 1 and device 4 are positioned at the front of the array with the axes of symmetry located at $(3.25m, 0.75m)$ and $(3.25m, 0.0m)$, respectively. For simplicity, device 1 will be referred to as the front-left device and

device 4 as the front-right device with the left/right identifier based on viewing the array from the direction of wave incidence. Device 2 and device 3 are positioned at the rear (left and right) of the array with the axes of symmetry located at $(4.0m, 0.75m)$ and $(4.0m, 0.0m)$, respectively. Therefore, the position of the device in the isolated device experimental performance tests corresponds to device 4 in the array tests.

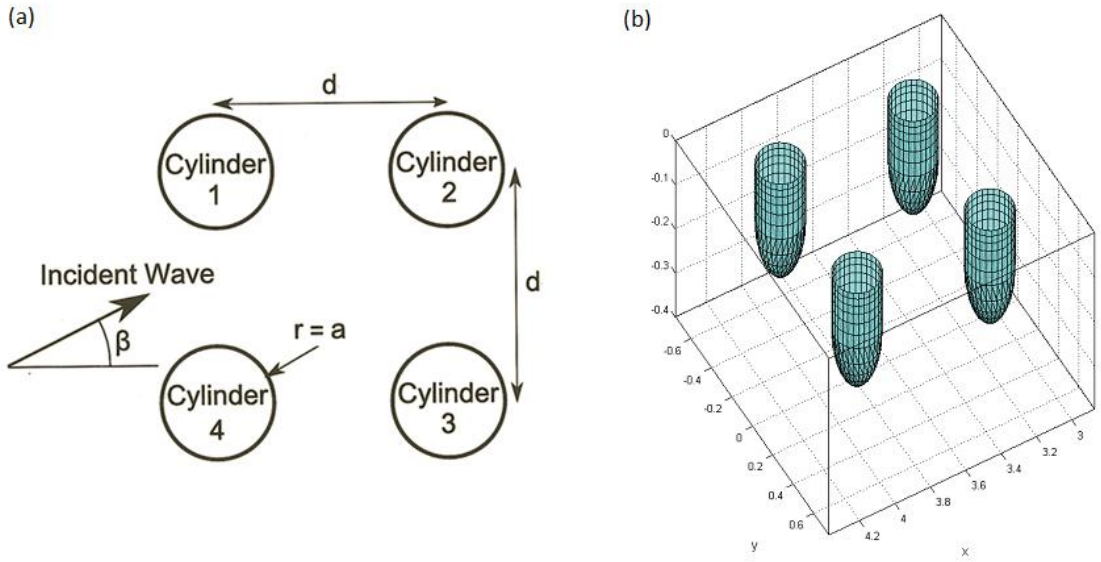

Figure 28: (a) Schematic of four device array configuration; (b) OXPOT discretisation of the four device array.

The incident focussed waves generated for the array tests utilised the same wavemaker signals as for the isolated device tests. A focussed wave calibration test involving wave probes at the intended device locations and an array performance test was conducted for each of the focussed waves listed in Table 1. In this section the results cover the tests numbered 13 and 21 corresponding to focussed waves with a full scale energy period of $T_e = 9.0s$ and $T_e = 11.0s$, respectively, and a focussed wave amplitude of $A = 3m$.

The focussed waves generated for both the isolated device and array tests were intended to be unidirectional so that each device at the front and rear of the array experiences the same wave-field. A plot of the free-surface elevation experimentally measured at four wave probes located the same (focus) distance from the wavemaker but at different lateral tank positions is shown in Figure 29. Only the data from the wave probe at $y = -4.0m$ differs considerably from the other time-histories. Therefore, it can be concluded that around the array the wave-field is unidirectional with some minor variations along the crest. In the case of the isolated device tests, the wave probe data from the probes located at $(x, y) = (2.0m, -4.0m)$ and $(x, y) = (2.0m, 4.0m)$ were averaged in order to obtain the wavemaker signal. The free-surface elevation simulation data at the position of the focus wave probe was compared to the corresponding experimental data and in each case a very good agreement was obtained. This comparison verified that the wave-field had been accurately recreated around the body given that the focus wave probe location in the wave calibration tests corresponds to the isolated device position in the performance test isolated device. Under the assumption that the wave-field has minimal variations in the lateral direction it was decided that the

wavemaker signal obtained for the single device simulations be used for the array simulations also. (This is advantageous for OXPOT comparisons between single device and array results.)

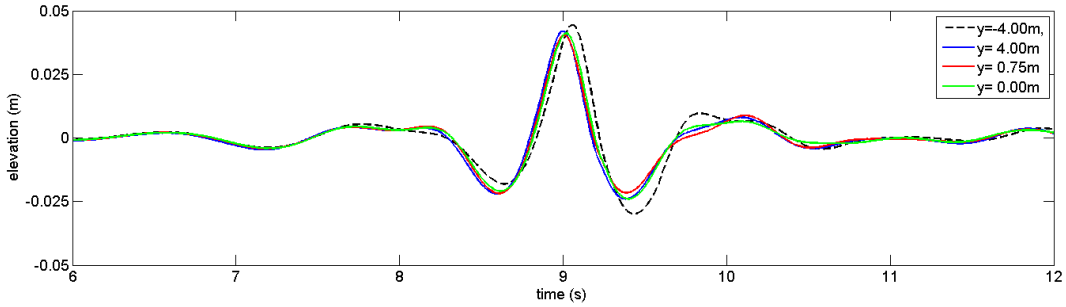

Figure 29: Free-surface elevations at wave probes a distance $x = 4.0m$ from the wavemaker from wave calibration test 21 for square arrays of four devices.

In a unidirectional wave-field in a wave tank, two identical devices located at the same perpendicular distance from the wavemaker but at different positions parallel to the wavemaker should have identical responses to the incident wave field. Therefore, the array performance tests provide an opportunity to assess the consistency of the device model mechanisms, such as the air bearing and the PTO brake. The motions of the devices at the rear of the array in performance test number 21 ($T_e = 11.0s$, $A = 3.0m$) are shown in Figure 30 (a) and compared to the response of the device in the isolated device performance test. There is clearly a significant difference in the amplitudes of the responses of device 2 and 3 thus indicating that the mechanical properties of the devices vary and can affect the motion of the devices considerably. However, the motion of the isolated device compares very well to the motion of the rear array device (2) at the tank location $(x, y) = (4.0m, 0.75m)$. This indicates that the mechanisms within these devices have very similar properties during motion and that array effects in this case do not strongly affect the rear devices. Nevertheless, the large discrepancy in the device motions in an interaction that should yield symmetric responses is worth noting, particularly in light of the discrepancies between the OXPOT predictions and the experimental measurements for the isolated device tests. The equivalent comparison for performance test 13 ($T_e = 9.0s$, $A = 3.0m$) involving the time-histories for both rear array devices and the isolated device is shown in Figure 30(b) and in this case there are even larger discrepancies between the device displacement time-histories. It is very unusual that the amplitude of the isolated device displacement is the smallest of the three time-histories because some of the wave energy propagating in the array test will be scattered/absorbed by the front array devices. This indicates that there are significant frictional losses occurring within the device motion mechanism which results in a restricted motion. This puts the discrepancy observed in section 4.3.3 into perspective. A similar observation can be made for the performance tests 5 corresponding to the incident wave of full scale energy period $T_e = 7.0s$ and focussed wave amplitude $A = 3m$, shown in Figure 30 (c).

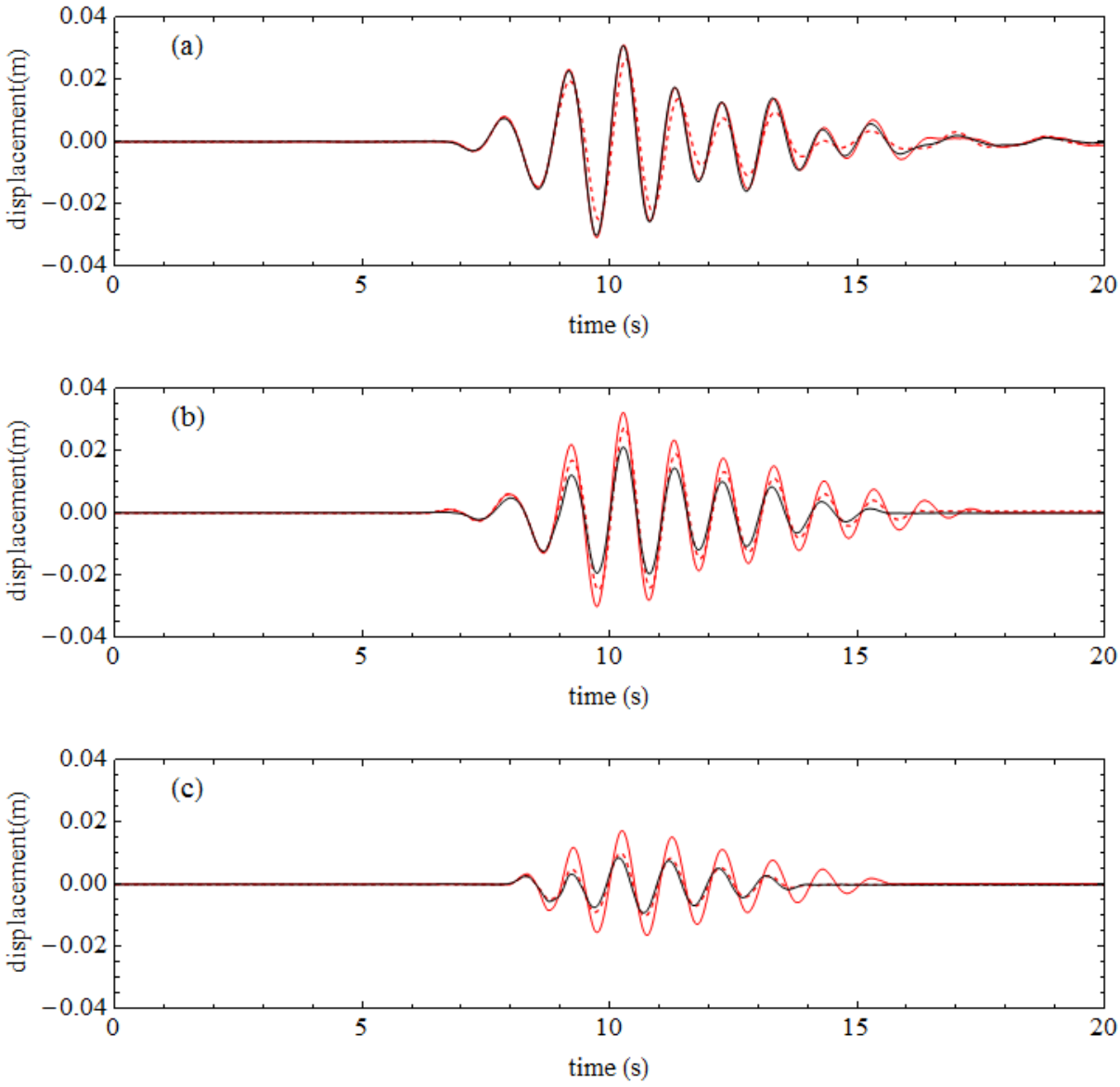

Figure 30: Experimentally measured displacement time-histories for device 2 (red, solid) of lateral position $y = 0.75m$ and device3 (red, dashed) of lateral position $y = 0.00m$ in the square array performance test and for the isolated device test (black, solid) for performance test (a) number 21, (b) number 13, (c) number 5.

5.2 Simulations of array performance tests

5.2.1 Summary of computational domains

The OXPOT simulations of the array performance tests exploit the symmetry in the interaction so that only one half of the experimental wave tank (and hence only two devices) is (are) simulated. The exploitation of this symmetry has been explained in previous deliverables (see section 3.2 and 4.1 of WG1 WP1 D11/D12) and will not be dwelt upon here. The assumption that the incident wave is unidirectional in the x-direction (perpendicular to the front 'face' of the array) and the assumption that the device properties are identical imply that the wave field will obey $\partial\phi/\partial y = 0$ and that the wave and device motion will be symmetric across the centre-line $y = 0$. Therefore, the total domain

can be represented by a half domain $y > 0$ with a no-flow wall condition at $y = 0$. Specifying the Green's function to satisfy $\partial G/\partial y = 0$ removes the integration over the wall of symmetry. Thus, the discretised computational domain looks like that shown in Figure 31. Therefore, only one time-history each will be obtained for the front and rear devices in the array.

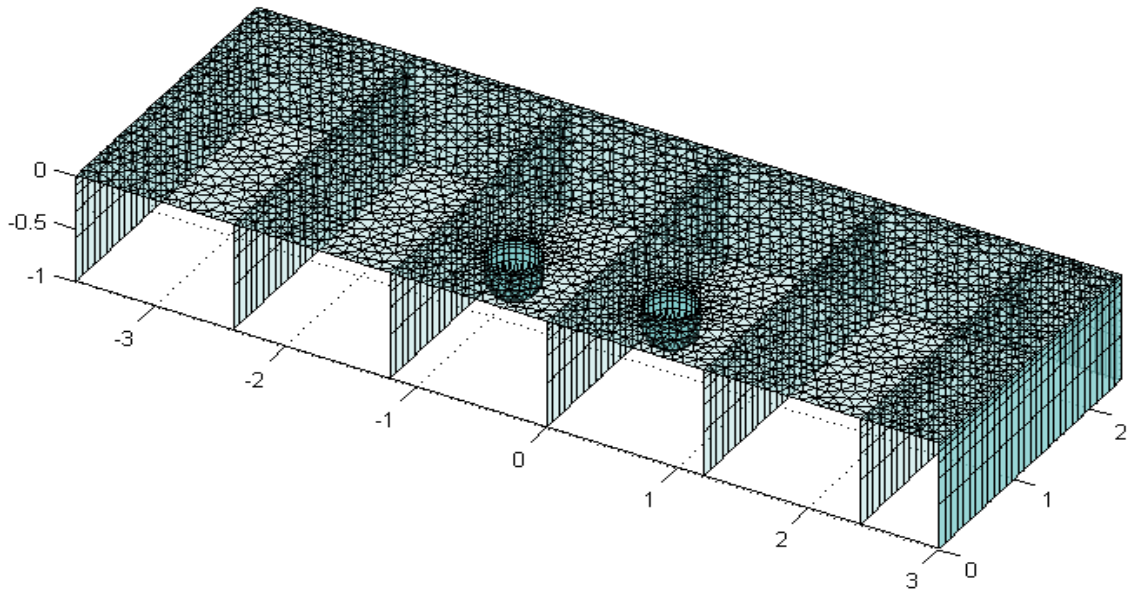

Figure 31: Representation of a typical computational domain for OXPOT simulations of array performance tests.

The computational domains used in the array simulations are based on the corresponding single device simulations. In particular, retaining the same free-surface mesh density as in the single device case is prioritised. The arc lengths of the cylinder elements are chosen to be greater than or equal to those of the isolated device simulations to ensure the mesh elements around the array are not distorted and to minimise computational overheads. Any reduction in cylinder element lengths should not have a large effect on the simulations given that the element lengths remain significantly smaller than those of the free-surface elements. Therefore, any higher order harmonics propagated through the free-surface mesh will be resolved at the cylinder also. To avoid lengthy descriptions of the domains in the device performance analysis section the details of the meshes used in the array simulations are summarised in two tables here. The first (Table 9) highlights the average mesh element size relative to the incident wave and the second (Table 10) presents the total number of elements, nodes and time-steps in the simulations.

Energy period (T_e/T_e^{exp})	**'Energy' wavelength** (λ_e^{exp})	**Free-surf. (FS) element length** (Δx)	**Wall element height at FS** (Δz)	**Cylinder element** (Δc)	**Domain width (W)**	$\lambda_e^{exp}/\Delta x$
$9.0s/1.01s$	$1.56m$	$0.067m$	$0.040m$	$0.040m$	$2.4m$	23.0
$11.0s/1.23s$	$2.23m$	$0.100m$	$0.040m$	$0.044m$	$3.0m$	22.3

Table 9: Specifications for the array performance test simulations for each of three incident focussed wave energy periods.

Energy period (T_e/T_e^{exp})	Elements			Nodes			Time steps
	Walls	Free surf.	Devices	Walls	Free surf.	Devices	
$9.0s/1.01s$	2358	5570	680	8055	11669	1722	2001
$11.0s/1.23s$	1900	4340	504	6625	8387	1298	1001

Table 10: Total numbers of elements and nodes on the different surfaces of the computational domains for the array performance simulations.

5.3 Array performance results and analysis

In the following, the results of the OXPOT simulations of the tests number 21 and 13 are analysed and compared to the corresponding experimental data. In the graphic illustrations of the comparisons, the measured time-histories of both front and rear devices are plotted alongside the front and rear device simulation time-histories. When assessing the accuracy of the OXPOT prediction of the measured device response, the experimental time-history with the larger displacement amplitude is used as the benchmark. This approach can be justified by considering the large variations in the device motions observed in Figure 30 – the largest motion of the device is likely to correspond to the device experiencing the least auxiliary frictional losses. In the case of the $T_e = 11.0s$ array interaction only one set of test data is available for comparison with OXPOT and only the first set of data is used for the $T_e = 9.0s$ simulation. Unlike the isolated device performance tests, the mean values over the ensemble of tests are not used.

The PTO force algorithm used in these simulations returns to the simplest algorithm possible, namely that the PTO force resists the exciting force until the exciting force exceeds the target force $(0.4N)$ after which the PTO force opposes the motion of the body with a brake force of magnitude equal to the target force. Once the exciting force decreases below the target force for longer than $0.1s$ then the PTO force balances the exciting force (and not the device motion) again. The exact details of the PTO force algorithm in the period after the focussed wave has passed the body and the motion and exciting force decay does not have a significant influence on the device motion and/or the mean properties of the device motion over the course of the simulation. The minor changes in the parts of the PTO force algorithm concerning the decay of the body motion and the exciting force have little more than an aesthetic influence on the PTO force time-histories. No frictional or viscous losses are modelled in the array simulations – the results are for device performance in an inviscid fluid with the only motion damping provided by the PTO brake.

It is also worth noting that the PTO force data presented in the subsequent plots are filtered so that the highest frequency oscillations are removed in order to reduce the 'clutter' in the figures with three separate time-histories. However, the r.m.s. PTO force values are taken from the source data.

5.3.1 $T_e = 11.0s,\ A = 3.0m$

The displacement time-histories of the front and rear devices in the array as measured in the performance test 21 and as simulated in OXPOT are compared in Figure 32. A similar agreement in terms of the amplitudes of the device displacement predicted by OXPOT and measured in the tests occurs here compared to the isolated device case. The devices with centres at $y = 0.75m$ have larger displacements than those at $y = 0.0m$. A similar comparison of the time-histories is made for the PTO forces in Figure 33 and the agreement is quite good. However, the PTO forces on both the rear devices are significantly (approximately 25%) smaller than the target PTO force of $0.4N$. For the

front devices, the device at $y = 0.0m$ experiences a peak PTO force 25% greater than the target force during the largest motion of the device. On the other hand, the device at $y = 0.75m$ experiences a brake force approximately equal to the target force. As a result, the power absorbed by the devices varies significantly depending on which device is considered as is illustrated in Figure 34. For the front device, the power absorbed by the experimental device with the largest PTO force exceeds that predicted by OXPOT at some instants. The power absorption curves associated with the rear test devices have much smaller peaks than the OXPOT device prediction as expected (given the smaller PTO forces experienced by the test devices).

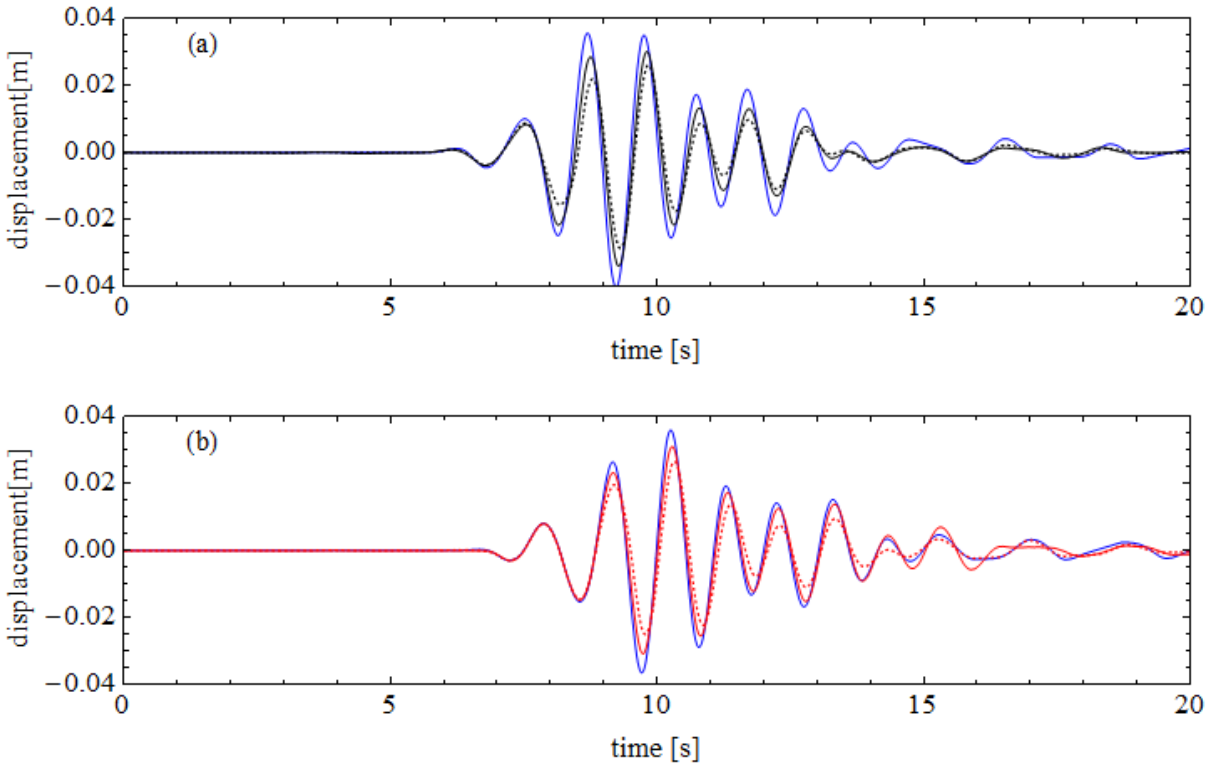

Figure 32: Experimental displacement time-histories (a) for front array device 1 (left, —) and device 4 (right,— —) and (b) for rear array device 2 (left, —) and device 3 (right, — —) compared to the corresponding front and rear device displacement OXPOT time-histories (—) for incident focussed wave 21.

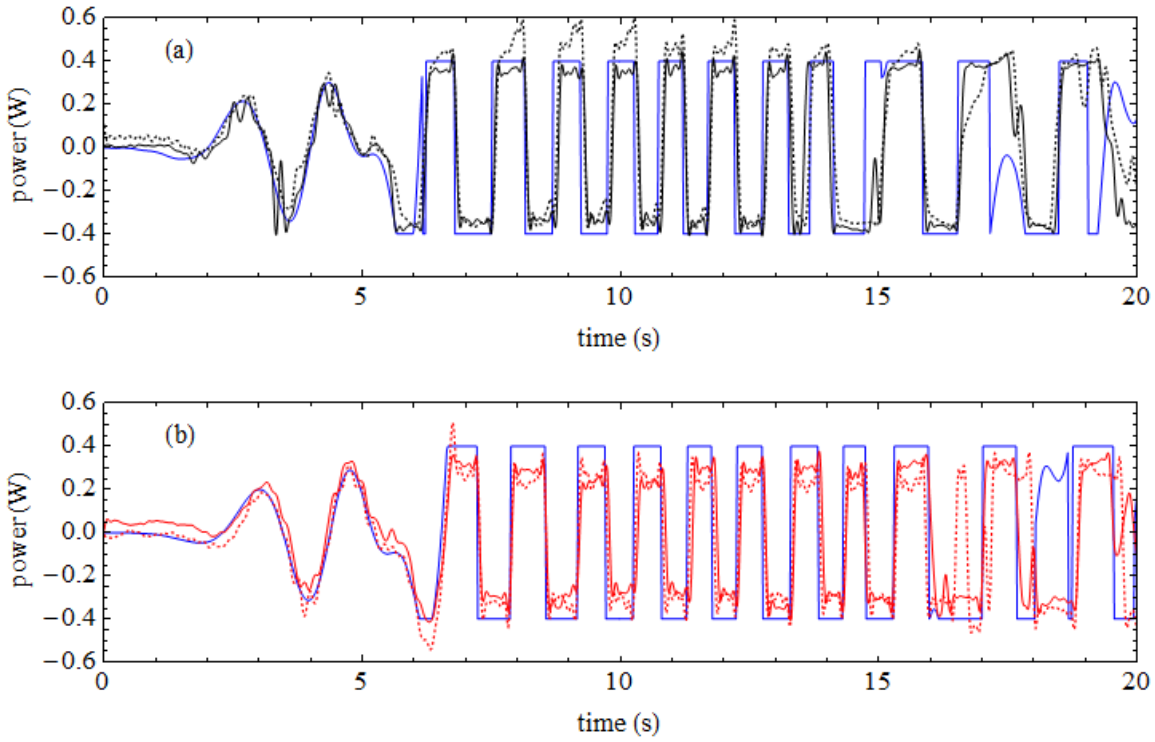

Figure 33: Experimental PTO force time-histories (a) for front array device 1 (left, —) and device 4 (right,— —) and (b) for rear array device 2 (left, —) and device 3 (right, — —) compared to the corresponding front and rear device PTO force OXPOT time-histories (—) for incident focussed wave 21.

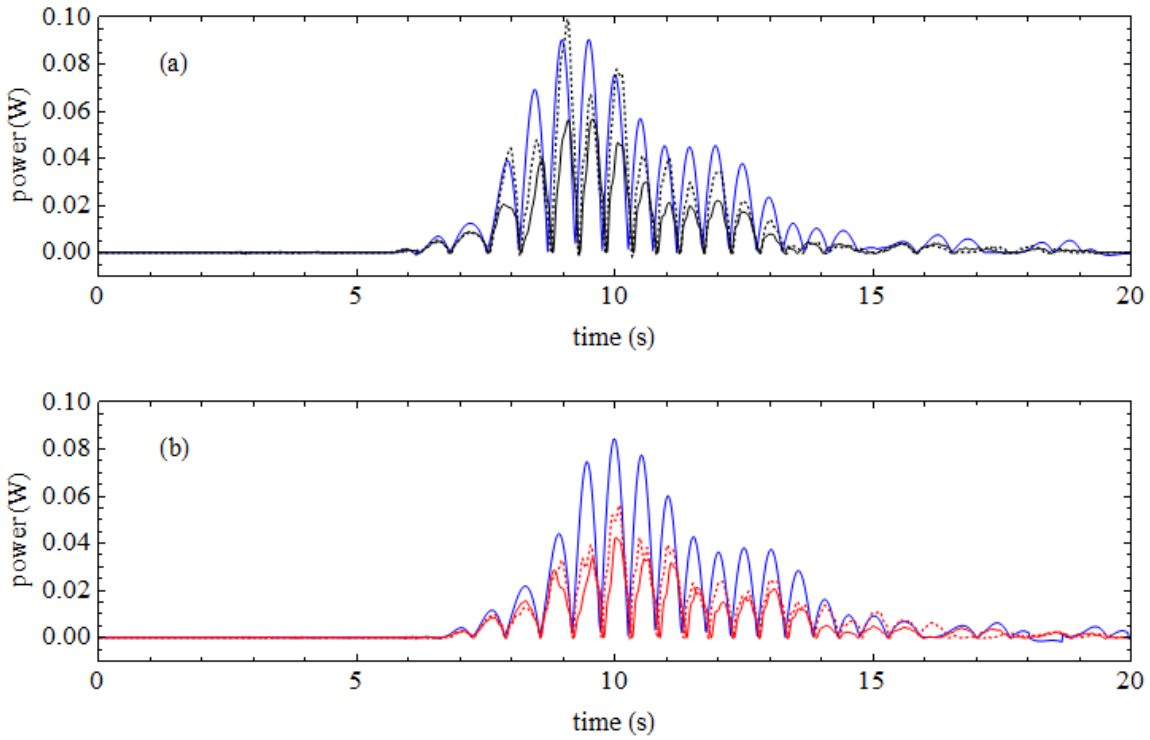

Figure 34: Experimental power absorption time-histories (a) for front array device 1 (left, —) and device 4 (right,— —) and (b) for rear array device 2 (left, —) and device 3 (right, — —) compared to the corresponding front and rear device power absorption time-histories (—) for incident focussed wave 21.

From a consideration of the large variations of the PTO force from the target value, it can be concluded that it is not useful to measure the accuracy of the OXPOT simulations by comparing the mean power absorbed. This is particularly true for the array simulations where the Coulomb PTO force amplitudes have not adjusted to match the forces measured in the experimental tests (unlike for the isolated device simulations). If the PTO forces for each device were to be adjusted then an averaged value of the PTO force experienced by the front and rear device would be necessary and this would still not guarantee a good agreement with regard to the power absorption curves. Therefore, to measure the accuracy of the OXPOT estimates the r.m.s. displacements of the devices in the experimental performance tests are compared to the corresponding OXPOT value as shown in Table 11. Although the OXPOT predictions are compared to both device motions, more emphasis is given to the comparison with the experimental device possessing the larger response amplitude. The OXPOT prediction of the rear devices motion agrees quite well with the data for the rear-left device (looking at the array from the direction of the incident wave). For the front devices, the discrepancy between the OXPOT estimate for the r.m.s. displacement and the r.m.s. value for the displacement data for experimental front-left device is similar to the isolated device comparison (see Table 5). The r.m.s. value of the PTO force between $t = 6s$ and $t = 16s$ is also presented in Table 11 for reference.

Case	Device location/#	PTO force (r.m.s.) [N]	Displacement (r.m.s.) [m]	% relative difference $(\xi_{ox}^{rms} - \xi_{exp}^{rms}) / \xi_{exp}^{rms}$
Experiment	Front – 1	0.380	0.0079	23.2%
Experiment	Front – 4	0.347	0.0064	51.3%
OXPOT	Front	0.400	0.0097	–
Experiment	Rear – 2	0.317	0.0080	12.5%
Experiment	Rear – 3	0.290	0.0066	36.6%
OXPOT	Rear	0.400	0.0090	–

Table 11: Root mean squared PTO force and displacement values for devices in experimental tests and numerical simulations of performance test 21.

5.3.2 $T_e = 9.0s,\ A = 3.0m$

The same comparisons were made between the OXPOT simulation results and the experimental data for performance test 13. The displacement time-histories are compared in Figure 35, the PTO force time-histories in Figure 36 and the instantaneous power absorbed in Figure 37. In Table 12 the r.m.s. displacements over the course of the first 20s of the test or simulation are provided with the percentage relative difference between the OXPOT and experimental results listed for purposes of comparison. An r.m.s. PTO force value is also provided for reference as computed over the interval of the most significant motion form $t = 6s$ to $t = 14s$. It is worth noting that here, for the array performance tests, the agreement between the OXPOT prediction of the device response and the measured response is better than for the isolated device tests as can be seen by comparing the percentage relative difference values in Table 12 to those in Table 7.

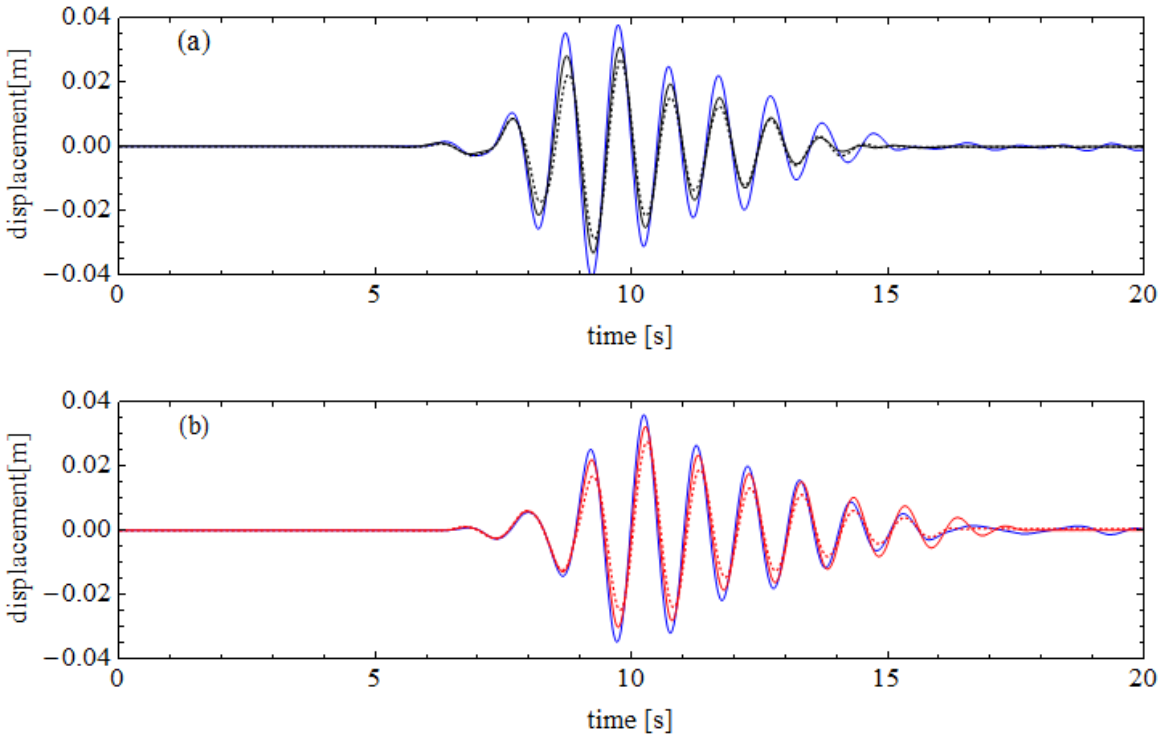

Figure 35: Experimental displacement time-histories (a) for front array device 1 (left, —) and device 4 (right,— —) and (b) for rear array device 2 (left, —) and device 3 (right, — —) compared to the corresponding front and rear device displacement OXPOT time-histories (—) for incident focussed wave 13.

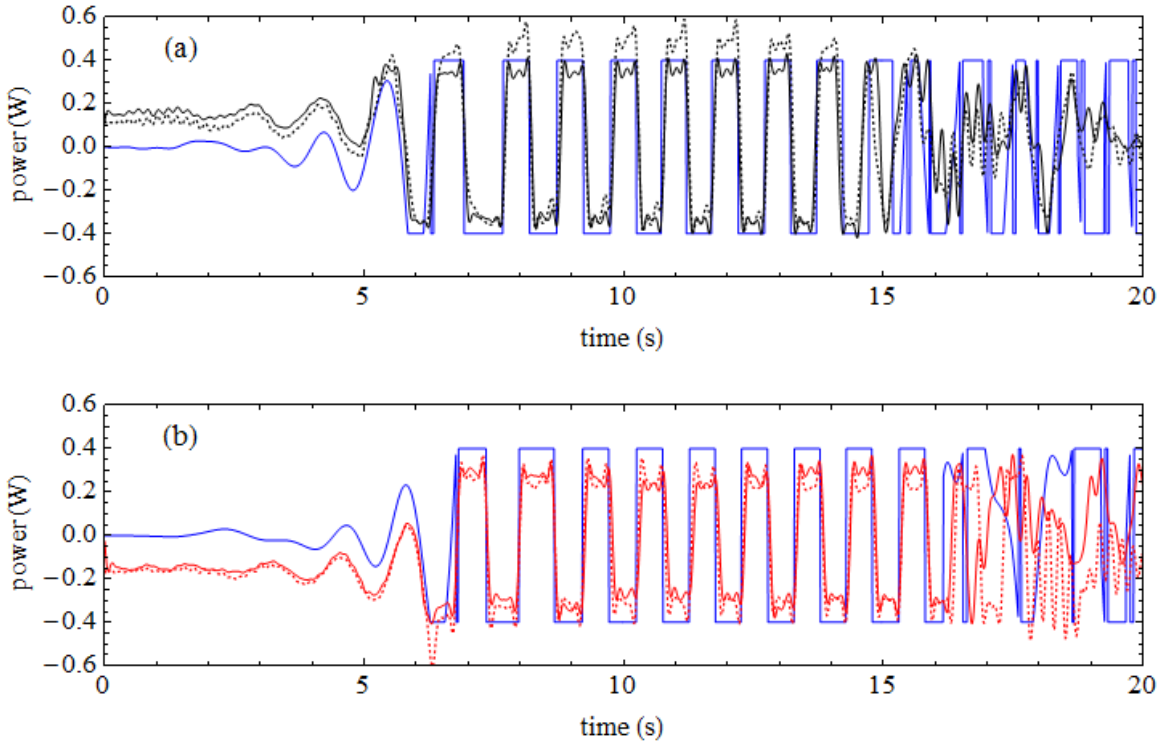

Figure 36: Experimental PTO force time-histories (a) for front array device 1 (left, —) and device 4 (right,— —) and (b) for rear array device 2 (left, —) and device 3 (right, — —) compared to the corresponding front and rear device PTO force OXPOT time-histories (—) for incident focussed wave 13.

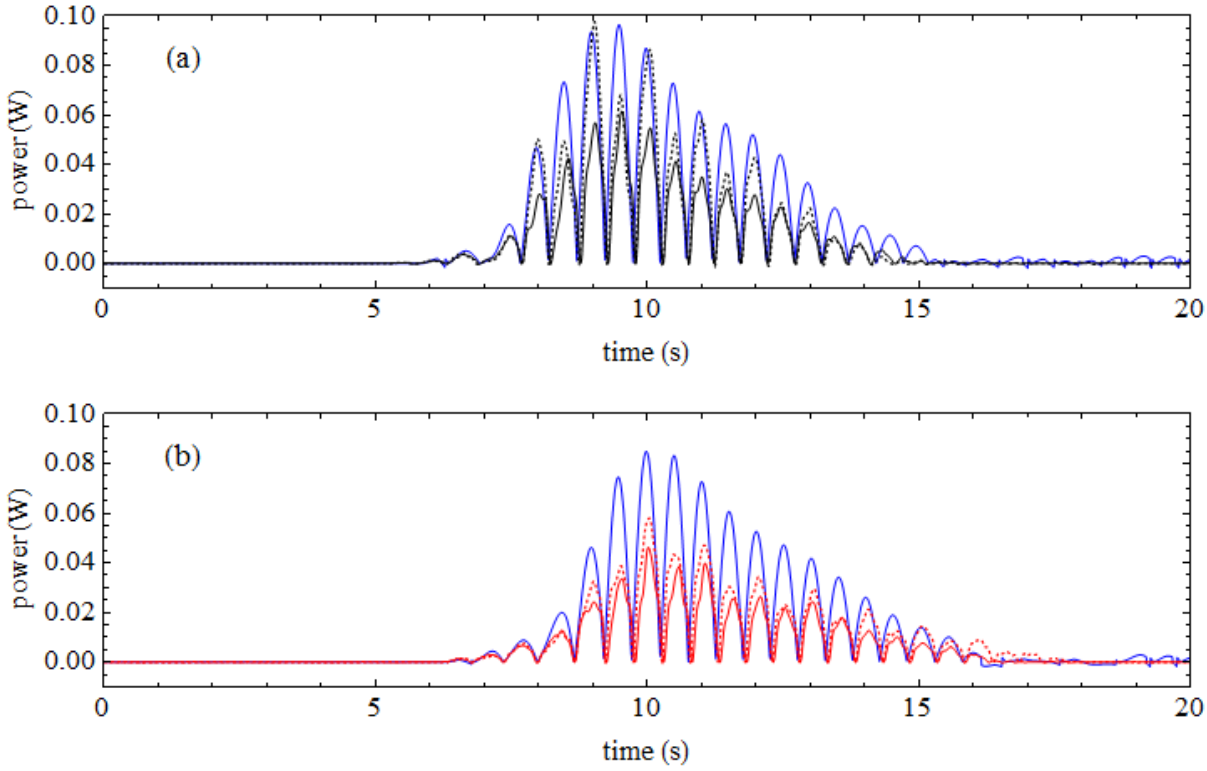

Figure 37: Experimental power absorption time-histories (a) for front array device 1 (left, —) and device 4 (right,— —) and (b) for rear array device 2 (left, —) and device 3 (right, — —) compared to the corresponding front and rear device power absorption OXPOT time-histories (—) for incident focussed wave 13.

Case	Device location/#	PTO force (r.m.s.) [N]	Displacement (r.m.s.) [m]	% relative difference $(\xi_{ox}^{rms} - \xi_{exp}^{rms})/\xi_{exp}^{rms}$
Experiment	Front – 1	0.385	0.0082	28.1%
Experiment	Front – 4	0.342	0.0069	51.2%
OXPOT	Front	0.400	0.00105	–
Experiment	Rear – 2	0.324	0.0085	10.8%
Experiment	Rear – 3	0.281	0.0069	37.0%
OXPOT	Rear	0.400	0.0094	–

Table 12: Root mean squared PTO force and displacement values for devices in experimental tests and numerical simulations of performance test 13.

5.4 Hydrodynamic interactions

The effect of hydrodynamic interactions between the devices on the response and performance of the devices within the array is briefly investigated in this section. In order to do this it is necessary to compare the response/performance time-histories of the device in isolation with a rear device in the array for a given performance test. Given the lack of consistency in the PTO properties and device motions in the experimental results the effect of the array interactions on the device response/performance are best investigated using the OXPOT results. For example, if the

response/performance of the isolated device is compared to the device in the array located in the same position in order to assess the effect of the surrounding devices on response/performance then it is crucial that the PTO force acting on the device and any frictional losses experienced by the devices are the same in both the isolated and array performance simulations. If the PTO force acting on the devices and the frictional losses experienced by the devices are not the same then it will be difficult to understand whether differences in the response/performance between the isolated and array device are due to array interaction effects or simply due to the experimental variability in the PTO properties and frictional losses experienced by the device. By using OXPOT to analyse the array interaction effects it is possible to eliminate the variability in the PTO properties and to specify frictional losses to be identical and so any differences between the isolated device and the corresponding array device will purely be due to array interaction effects. These array interaction effects will be consistent with the set of isolated device and array performance results obtained from OXPOT. It is also assumed that the width of the domain in the array interaction simulation is equivalent to that in the isolated device case. For example, in the isolated device simulation for test number 21 the half-width of the domain (and wall-to-cylinder distance) is $W = 2.5m$ while in the corresponding array simulation the half-width of the domain is $W = 3.0m$ and the distance from the wall to the cylinder is $2.625m$ because the device is located at $y = 0.375m$. The reflected waves should return to the cylinder around the same time and should not affect our analysis of the hydrodynamic interactions.

5.4.1 Incident focussed wave ($\boldsymbol{T_e = 11.0s, A = 3m}$)

The effect of the hydrodynamic interactions on the device response and performance for the rear device in the array in simulations of performance test 21 (involving the focussed wave with full scale parameters ($T_e = 11.0s, A = 3m$) is illustrated in Figure 38. There is a clear reduction in the displacement amplitude and power absorbed due to presence of the devices at the front of the array. Interactions due to the presence of the symmetrically located rear device may also affect the motion and performance of the device. In order to fully assess the extent of the hydrodynamic interactions it is useful to run another isolated device simulation with the same incident wave as before but with the device now located the same distance from the wavemaker as the devices at the front of the array. In this way, the effect of the devices positioned to the rear of the array (and the other device at the front of the array) can be assessed. A comparison of the relevant displacement and power absorption time-histories are shown in Figure 39. As expected, the effect of the devices at the rear of the array on the motion of the devices to the front of the array is much smaller than the effect of the front devices on those to the rear.

To measure the strength of the interactions it is useful to compute an interaction factor analogue for devices in focussed waves with non-optimal motions. The interaction factor as defined for regular waves is defined as the ratio of the maximum (mean) power absorbed by an array of N devices to the maximum (mean) power absorbed by a single such device in isolation. In a regular wave field the position of the isolated device will not affect the maximum power absorbed. However, in a focussed wave field the location of the device will be very important in determining the power absorbed: for example, placing the device at the focus location and far from the focus location will yield very different device motions. Therefore, to assess the effect of the interactions we compute the following quantity

$$q_{focus} = (P^A_{rear} + P^A_{front})/(P^I_{rear} + P^I_{front}), \quad (18)$$

where P^A represents the mean power absorption for devices in the array and P^I represents the mean power absorbed by a device in isolation. In this simulation, the mean power absorbed by the devices in the array at the front and rear over the course of the whole simulation is $0.01407W$ and $0.01275W$, respectively. In isolation, the device located at the front array position has a mean power capture of $0.01460W$ and for the device located at the rear array position the mean power capture is $0.01451W$. Therefore, the focussed wave interaction factor takes the value 0.92 indicating an average reduction in the power capture of a device in the array of 8% compared to the same device in isolation.

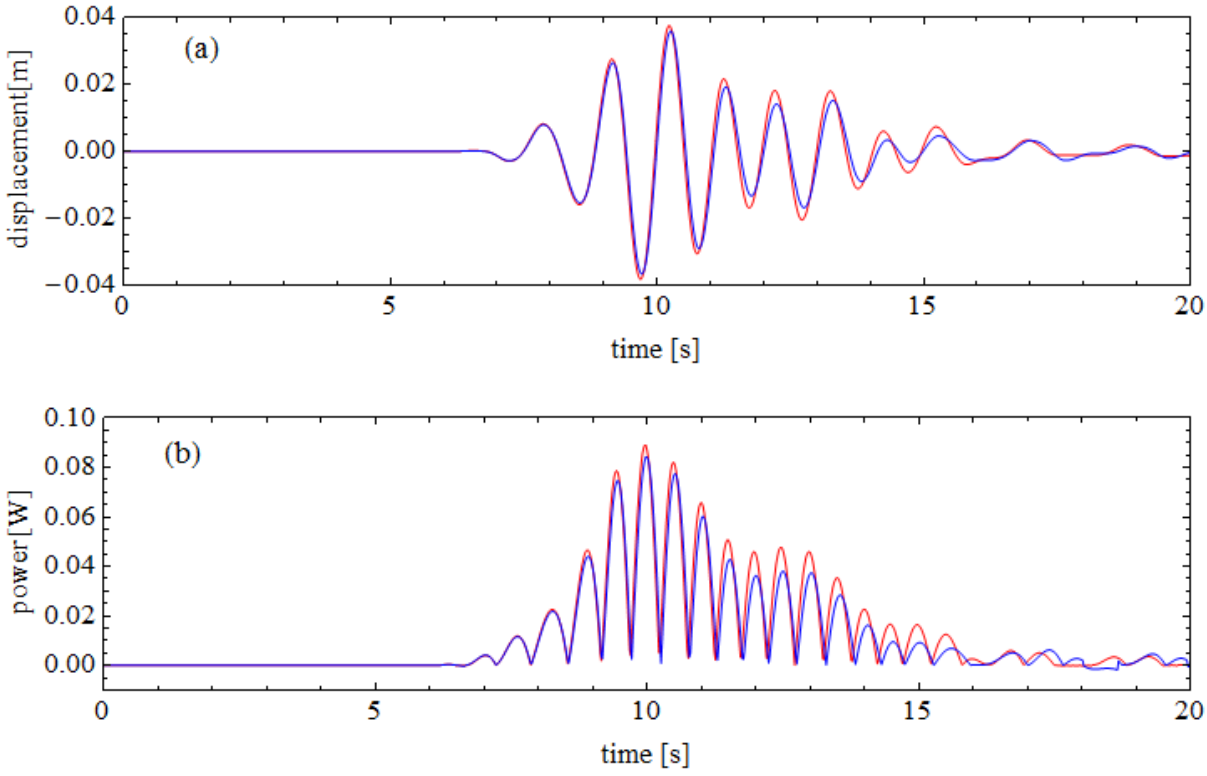

Figure 38: (a) Displacement time-histories and (b) power absorbed time-histories for the isolated device (red) and the rear device in the array (blue) for simulations of performance test 21.

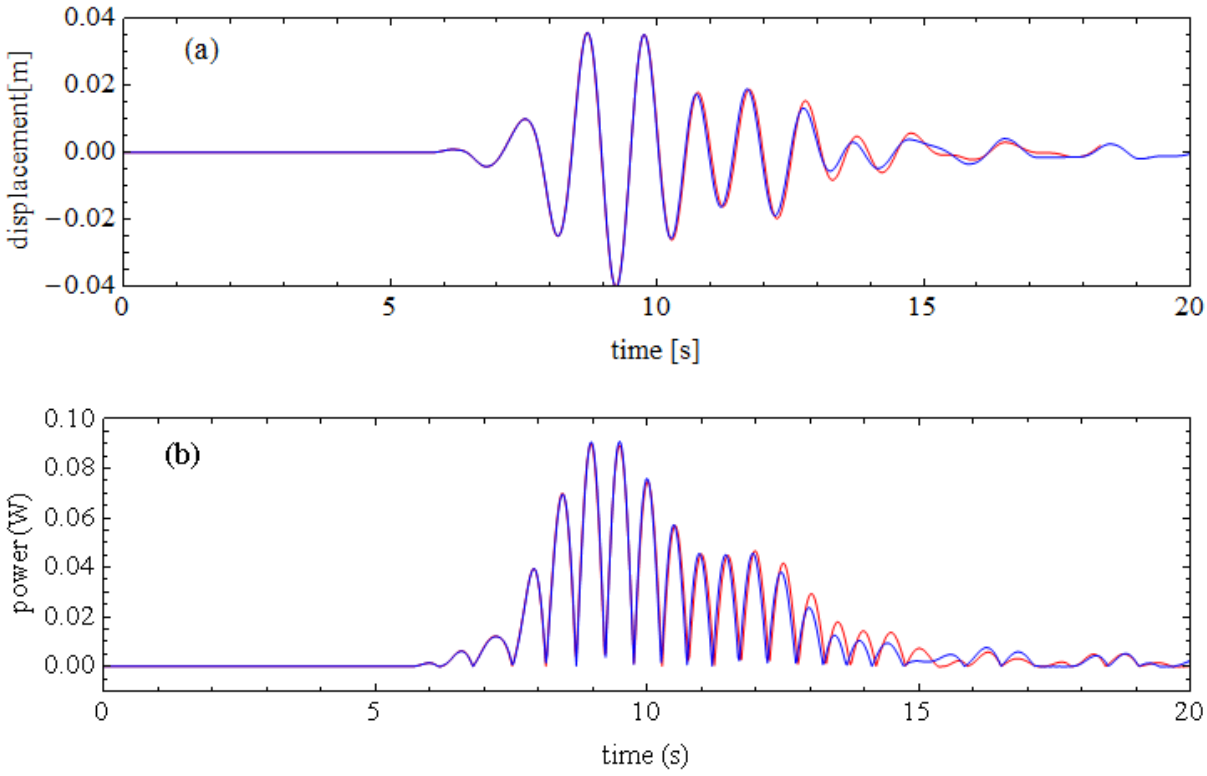

Figure 39: (a) Displacement time-histories and (b) power absorbed time-histories for the isolated device (red) located the same distance ($d = 3.25m$) from the wavemaker as front devices in the array (blue) for incident focussed wave 21.

5.4.2 Incident focussed wave ($T_e = 9.0s, A = 3m$)

A similar analysis can be conducted for the array and isolated device simulations of performance test 13. One issue to be addressed with this case is that the computational half-width is identical in both the isolated device and array OXPOT simulations. Therefore, the devices in the array simulation are closer to the side-wall because they are located at $y = 0.375m$ rather than $y = 0.0m$. Instead of comparing the response and time-history over the complete duration of the simulations (20s) we just consider the first $16s$ of the simulation. In this way, the effect of side-wall reflections should be negligible compared to the effect of the hydrodynamic interactions. A comparison of the displacement and power absorption time-histories for the isolated device located at the focus distance from the wavemaker and the similarly located rear array device is given in Figure 40. From a visual comparison of Figure 38 (a) and (b) to Figure 40 (a) and (b) it is evident that the effect of the devices at the front of the array is larger for the incident wave of period $T_e = 9.0s$. A similar observation can be made for the front device.

It is not surprising that the interaction effects are more marked for the incident wave of smaller energy period because the frontage per unit wavelength of the devices is larger in this case. Therefore, before wave radiation and energy absorption is taken into account, the devices at the front of the array will scatter more energy (relative to the total incident energy) than in the longer period case considered previously. For these simulations of the performance test 13, the mean

power absorbed by the devices in the array at the front and rear over the course of the whole simulation is $0.0161W$ and $0.0146W$, respectively. In isolation, the device located at the front array position has a mean power capture of $0.0177W$ and for the device located at the rear array position the mean power capture is $0.0172W$. A reduction of 15% in the mean power capture of the device over the first 16s of the simulation is experienced by the rear device operating in the array relative to operation in isolation. The focussed wave interaction factor takes the value 0.88 indicating an average reduction in the power capture of a device in the array of 12% compared to the device in isolation.

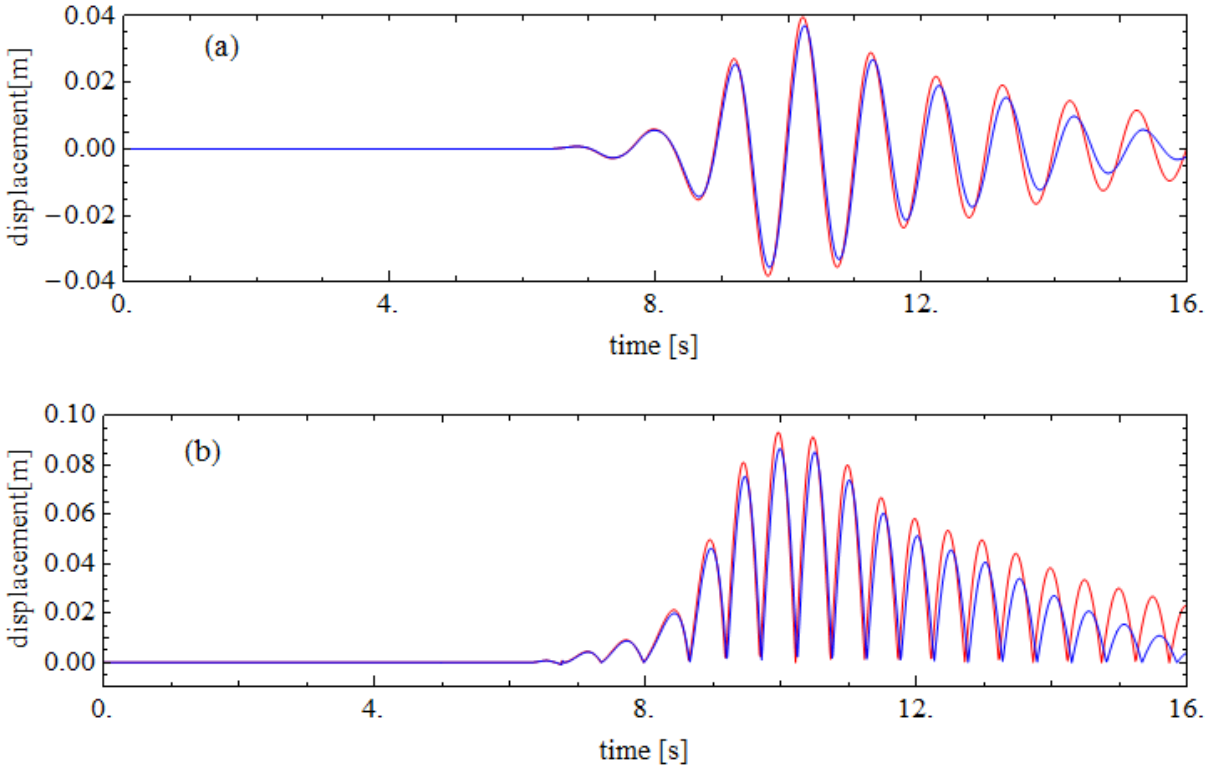

Figure 40: (a) Displacement time-histories and (b) power absorbed time-histories for the isolated device (red) and the rear device in the array (blue) for simulations of performance test 13.

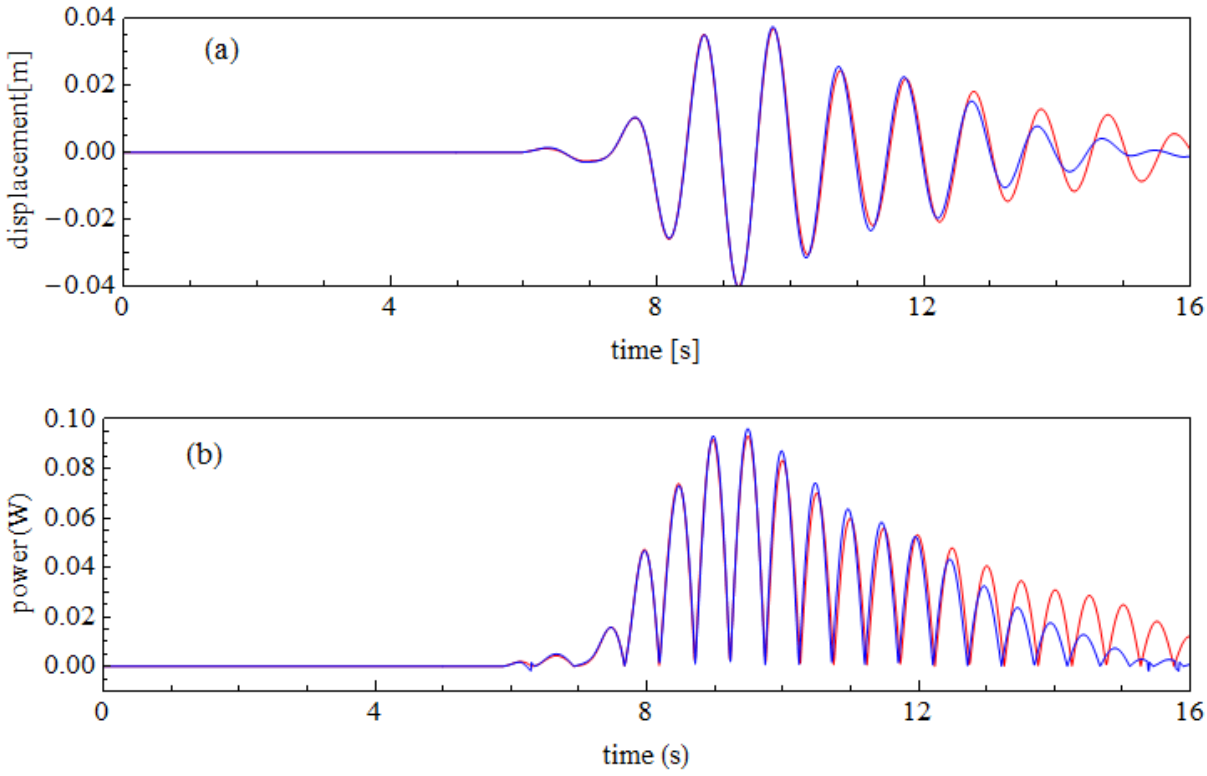

Figure 41: (a) Displacement time-histories and (b) power absorbed time-histories for the isolated device (red) located the same distance ($d = 3.25m$) from the wavemaker as front devices in the array (blue) for incident focussed wave 13.

6 Conclusions

In this report the results of the fully non-linear time-domain simulations of unidirectional focussed wave calibrations tests and device performance tests for isolated devices and small arrays of devices are compared to the corresponding experimental test results. The focussed wave experimental tests form only a small subset of the total QUB test programme – regular wave tests and irregular wave tests for small arrays and large arrays were also conducted. However, the tests involving focussed waves were more likely to yield clean response data (without interference due to tank reflections) and are more suitable for simulation by OXPOT because the duration of the tests are short. Furthermore, the use of focussed waves allows the generation of a single large event at a particular location during the test. This is preferable to irregular wave tests where large wave events can occur throughout the tank but not necessarily at the desired (device) location. Therefore, the scope of experimental simulations was restricted to the focussed wave tests. Nevertheless, a large number of OXPOT simulations and comparisons were conducted. Three different energy periods ($T_e = 7.0s, 9.0s, 11.0s$ at full scale) were generated and for each period two different amplitudes ($A = 1m$ and $A = 3m$ at full scale) and four different phases were considered. For the $T_e = 11.0s$ case a larger amplitude case ($A = 4m$) was also tested.

A summary of the approach to experimental testing taken for the case of the focussed waves is provided in this deliverable and this summary includes some of the details from the reports WG2 WP2 D2/D3/D4/D5 on the complete experimental testing programme. Of particular interest in the focussed wave tests is the use of four phase realisations of each focussed wave to obtain harmonic separation of fully nonlinear time-histories. A successful demonstration of the separation of an experimental time-history into individual harmonics for the free-surface elevation as measured at a wave probe at the focus location in the wave calibration tests is presented in Figure 8 (a). Furthermore, by separating the harmonics of the wave probe data elevation time-histories it is possible to isolate the linear component and reconstruct the experimental wavemaker signal. An OXPOT simulation of the particular wave calibration test under consideration was then obtained by using the wavemaker signal as input. Comparisons of the OXPOT free-surface elevation to the experimental elevation at linear, second order sum and third order sum harmonics showed a good agreement. Thus, the fully-nonlinear simulation of the wave calibration tests was demonstrated to be successful which was important from the perspective of accurately simulating the performance tests. The phase-separation method based on four phase shifted realisations of the focussed wave is fundamental to this simulation procedure.

The simulation of the wave calibration tests proved relatively straightforward given the necessary experimental data, i.e. the free-surface elevation of the four phase-shifted focussed waves. The presence of multiple probes in the wave tank at the same distances from the wavemaker and the precision and control of the wavemaker meant a single wave calibration only was necessary for each focussed wave. However, during the isolated device performance tests it was observed that the device response amplitude varied upon repeating the same test involving the same waves. In order to assess the statistical variability in the performance test results a further set of nine tests were conducted. The mean value of the device displacement and PTO force was used for the purposes of comparison with the corresponding simulation results. The mean value for the device displacement and PTO brake force was compared to the maximum and minimum response cases in order to assess the reliability of the mechanisms related to the device motion and the repeatability of the test.

Despite the large complexity of the tests due to the presence of the PTO rotary brake, the air bearing to restrict the motion to heave and the wire-and-pulley setup, the results for the statistical variation of $T_e = 11.0s$ results was quite small. However, it was found that the results of the shorter wave $T_e = 7.0s$ interactions varied significantly more from the mean than those for the $T_e = 11.0s$ wave interaction.

In order to simulate the motion of the device responding to the incident focussed waves it was important to accurately model the focussed waves incident on the device and the PTO brake force applied to the device while in motion. The focussed waves were accurately recreated in the process of simulating the wave calibration tests. To model the PTO brake force it was necessary to consider the PTO force measurements from a given performance test. The brake force is designed to balance the wave excitation force when this force does not exceed a given target value. Once the exciting force exceeds the target value then the device begins to move and the brake is designed to apply an approximately constant (target) force in opposition to the motion. Analysis of the PTO force measurements for one performance test revealed that the constant force opposing the body motion was not always equal to the target force. Nevertheless, implementation of a relatively simple PTO algorithm gave good agreement between the simulated brake force and the experimental measurements during the excitation of the device motion. (High frequency components of the experimental time-history were filtered out in order to provide a 'cleaner' signal with which to compare the OXPOT model results.) The PTO force signal was observed to be more erratic after the main wave packet had passed and the motion decreased in the particular test considered. Such erratic behaviour is difficult to model and given that the power capture during this phase of the simulation is negligible it was decided to leave the simple PTO algorithm unchanged.

The acceptance criteria for this deliverable require that a comparison of the fully nonlinear predictions of the experimental tests to the measured behaviour be provided. Furthermore, an assessment of the accuracy of the predictions is also stipulated in the criteria. Given the substantial number of focussed wave tests conducted it was necessary to restrict the number of tests simulated. Therefore, the performance tests involving larger amplitude focussed waves were considered for simulation given that these cases were more likely to involve nonlinear hydrodynamics. As discussed in 4.2.2, the harmonic separation method could not be applied to the experimental time-histories because of variations in the applied PTO force and the non-alignment of the crest and troughs of the device motion for incident waves 180° out of phase. Therefore, only one of the four phases of each the large amplitude focussed wave performance tests were simulated.

The OXPOT simulations of the interactions were generally quite successful. The OXPOT predictions for the device response, in particular the phase of the device displacement signal, agreed very well with the associated measured behaviour. A comparison of the PTO brake force revealed a similarly good agreement – the instant of transition of the brake force from positive to negative being very close for the numerical and experimental results. The main discrepancy between the OXPOT simulation results and the experimentally measured behaviour was the amplitude of the device response and the PTO force amplitude. Analysis of the experimental behaviour suggests that discrepancy between the simulated and experimental results is due to the following:

- Frictional losses arising in the device mechanisms such as bearings and hinges involved in the motion;

- Viscous losses (due to vortex shedding etc.) during the motion of the device through the water (small scale device interactions are particularly susceptible to such damping);
- The deviation of the PTO force magnitude from the target force of $0.4N$.

A simple model of frictional losses as a linear damping term in the device equation of motion and the adjustment of the PTO force magnitude to match the experimentally measured value (and not the target force) was seen to improve the device displacement agreement considerably as shown in Figure 22. The comparison of the power absorption values requires the PTO forces to agree quite well. A measure of the accuracy of the simulations was provided by comparison of the r.m.s. displacement value for the duration of the simulations and over the same interval for the experiment. Furthermore, the mean power capture was computed and compared for the simulation durations also. The relative difference between the numerical and experimental r.m.s. displacement and mean power capture values was found to be quite large is some cases. However, the reliability of the PTO force brake mechanism, the varying magnitude of frictional losses and the viscous losses occurring in the experimental tests mean that significant differences between the numerical simulations and experimental results were likely. Modification of the equation of motion with a damping term to describe the energy losses in the experimental system requires iteration of the simulations in order to identify the correct coefficients for the damping term. Such a procedure is not suitable for the computationally demanding OXPOT simulations. A brief discussion of nonlinearity in the performance tests (in particular in the simulation of these tests) was presented and it was concluded that the effects of hydrodynamic nonlinearity were negligible in the cases considered.

The same comparisons were made for the isolated device and array performance test simulations. The measured experimental behaviour in the array performance test highlighted the reliability issues observed in the isolated device reliability tests. In particular, the PTO brake force amplitude and device displacement varied according to the device considered. For a unidirectional focussed wave normally incident on a square array it is expected that the device motions of the front and rear devices will be symmetric provided all device properties are identical. However, significant differences exist. Nevertheless, the results of the OXPOT simulations (isolated device and array interactions) were used to investigate the hydrodynamic interactions between devices. In the case of the $T_e = 9.0s$ array interaction there were reasonably large device interactions leading to a 12% reduction in the performance of a device in the 2×2 array as opposed 4 devices in isolation.

To summarise:

- Separation of the higher order harmonic contributions free-surface elevation time-histories was made possible by the use of four phase realisations of the focussed waves. Isolating the linear component allowed for the reconstruction of the wavemaker signal for use in simulating the wave calibration tests.
- Fully nonlinear simulations of the wave calibration tests successfully recreated the incident focussed waves up to third order.
- A good approximation of the PTO brake force was implemented in OXPOT using a simple Coulomb friction algorithm.

- The reliability of the experimental tests was observed to vary depending on the incident focussed waves. Furthermore, the target constant PTO force applied by the brake was observed to vary over the course of some tests.
- The isolated device and square array performance tests were simulated with a good deal of success. An improvement in the agreement between the numerical and experimental results could be achieved given a more accurate characterisation of the frictional losses experienced by the devices in the experimental tests and more stable PTO force values.
- Array interactions were shown to be relatively small but clearly present by comparison of the isolated device and corresponding array device time-histories.
- The influence of hydrodynamic nonlinearity in the simulations of the performance tests was found to be negligible for the particular focussed wave interactions considered here.

It is evident from this report that OXPOT models the nonlinearity in the incident focussed waves and the consequent device response (once an adequate model of the friction losses and/or PTO force variability was accounted for) very well. For the particular focussed waves considered here this hydrodynamic nonlinearity did not have a significant influence on the response and performance of the device. However, it should be considered that only a relatively small subset of interaction parameters have been investigated here. To draw a well-informed conclusion regarding the role of OXPOT in simulating wave energy interactions, a more extensive follow-up investigation is required. Firstly, the experimental simulation results from a linear solver must be compared to these fully nonlinear results in order to understand how much more physics the fully nonlinear solver can represent compared to the linear model. Furthermore, the role of nonlinearity in the hydrodynamic forces on the devices has not been investigated here and will certainly be important in wave energy applications. (Hydrodynamic forces have not been considered here because there is no experimental data for the forces experienced by the device once the device is in motion). Accurate prediction of the hydrodynamic forces experienced by a body will be particularly important from a survivability perspective – for example, in survivability conditions it will be very useful to be able to accurately assess the maximum surge/heave force experienced by the structure. Therefore, a comparison of the hydrodynamic forces as predicted by the linear and fully nonlinear solver in both the operational mode (in motion) and survival mode (with motion significantly restricted or effectively held fixed) will be very useful. The acceptance criteria for the next deliverable WG1 WP1 D14 are as follows:

“Report on assessment of the accuracy of both the linear and fully nonlinear approaches to particular FDCs (fundamental device concepts) and events (moderate seas related to performance conditions; extreme seas related to survivability conditions) and draws conclusions on the ranges of validity of the linear wave analysis and an assessment of how much further nonlinear modelling can represent and therefore predict, real conditions.”

Therefore, the next deliverable provides an opportunity for a more complete assessment of the advantages and disadvantages of using OXPOT (relative to a linear potential flow solver) in the analysis of the performance of a wave energy device in performance conditions and for the assessment of hydrodynamic loads on the device in survivability conditions. Any conclusions drawn here would be premature.

Bibliography

Bai, W. & Eatock Taylor, R., 2006. Higher-order boundary element simulation of fully nonlinear wave radiation by oscillatiing vertical cylinders. *Applied Ocean Research,* Volume 28, pp. 247-265.

Bai, W. & Eatock Taylor, R., 2007. Numerical simulation of fully nonlinear regular and focused wave diffraction around a vertical cylinder using domain decomposition. *Applied Ocean Research,* Volume 29, pp. 55-71.

Bai, W. & Eatock Taylor, R., 2009. Fully nonlinear simulation of wave interaction with fixed and floating flared structures. *Ocean Engineering,* Volume 36, pp. 223-236.

Baldock, T. E., Swan, C. & Taylor, P. H., 1996. A laboratory study on nonlinear surface waves on water. *Philosophical Transactions of the Royal Society of London A,* Volume 354, pp. 649-676.

Borthwick, A. G. L. et al., 2006. Flow kinematics of focused wave groups on a plane beach in the UK coastal research facility. *Coastal Engineering,* Volume 53, pp. 1033-1044.

Fitzgerald, C. et al., 2012. *Phase manipulation and the harmonic components of ringing forces on a surface-piercing column.* Copenhagen, Denmark, 23rd International Workshop on Water Waves and Floating Bodies.

Hunt, A. C., Taylor, P. H., Borthwick, A. G. L. & Stansby, P. K., 2002. *Focused waves onto a plane beach.* Banff, Canada, 7th International Workshop on Wave Hindcasting and Forecasting .

Wu, G. X. & Eatock Taylor, R., 1996. *Transient motion of a floating bodyin steep water waves.* Hamburg, Proceedings of Eleventh International Workshop on Water Waves and Floating Bodies.

Yeung, R. W. & Jiang, Y., 2011. *Effects of shaping on viscous damping and motion of heaving cylinders.* Rotterdam, The Netherlands, Proceedings of the ASME 2011 30th International Conference on Ocean, Offshore and Arctic Engineering.

Zang, J. et al., 2006. Second order wave diffraction around a fixed ship-shaped body in unidirectional steep waves. *Journal of Offshore Mechanics and Arctic Engineering,* Volume 128, pp. 89-100.

Zang, J. et al., 2010. *Experimental study of non-linear wave impact on offshore wind turbine foundations.* s.l., Proceedings on the Third International Conference on the Application of Physical Modelling to Port and Coastal Protection.